

REPORT DOCUMENTATION PAGE			Form Approved OMB NO. 0704-0188		
<p>The public reporting burden for this collection of information is estimated to average 1 hour per response, including the time for reviewing instructions, searching existing data sources, gathering and maintaining the data needed, and completing and reviewing the collection of information. Send comments regarding this burden estimate or any other aspect of this collection of information, including suggestions for reducing this burden, to Washington Headquarters Services, Directorate for Information Operations and Reports, 1215 Jefferson Davis Highway, Suite 1204, Arlington VA, 22202-4302. Respondents should be aware that notwithstanding any other provision of law, no person shall be subject to any penalty for failing to comply with a collection of information if it does not display a currently valid OMB control number.</p> <p>PLEASE DO NOT RETURN YOUR FORM TO THE ABOVE ADDRESS.</p>					
1. REPORT DATE (DD-MM-YYYY) 01-10-2012		2. REPORT TYPE Final Report		3. DATES COVERED (From - To) 23-Jun-2003 - 22-Jun-2008	
4. TITLE AND SUBTITLE An Integrated Computational and Experimental Approach Toward the Design of Materials for Fuel Cell Systems			5a. CONTRACT NUMBER DAAD19-03-1-0169		
			5b. GRANT NUMBER		
			5c. PROGRAM ELEMENT NUMBER 106011		
6. AUTHORS Al Anderson (CWRU), and Gus Scuseria (Rice) Experimental Team Andrzej Wieckowski (UIUC), Sanjeev Mukerjee (Northeastern), Matt Neurock (UVA), Tom Zawodzinski (CWRU) Theory Team Gerbrand			5d. PROJECT NUMBER		
			5e. TASK NUMBER		
			5f. WORK UNIT NUMBER		
7. PERFORMING ORGANIZATION NAMES AND ADDRESSES Case Western Reserve University Case Western Reserve University 10900 Euclid Avenue Cleveland, OH 44106 -7015				8. PERFORMING ORGANIZATION REPORT NUMBER	
9. SPONSORING/MONITORING AGENCY NAME(S) AND ADDRESS(ES) U.S. Army Research Office P.O. Box 12211 Research Triangle Park, NC 27709-2211				10. SPONSOR/MONITOR'S ACRONYM(S) ARO	
				11. SPONSOR/MONITOR'S REPORT NUMBER(S) 45114-CH-MUR.1	
12. DISTRIBUTION AVAILABILITY STATEMENT Approved for Public Release; Distribution Unlimited					
13. SUPPLEMENTARY NOTES The views, opinions and/or findings contained in this report are those of the author(s) and should not be construed as an official Department of the Army position, policy or decision, unless so designated by other documentation.					
14. ABSTRACT The MURI set out with a series of objectives to construct a 'theory toolkit' coupled to advanced experimentation for validation and support. We have achieved all of our initial objectives in this regard and have expanded the scope of the MURI to use theory and experimentation to drive the prediction and preparation of new and highly active catalysts for key processes in fuel cells. Succinctly stated, our theory and experimental goals were as follows:					
15. SUBJECT TERMS					
16. SECURITY CLASSIFICATION OF:			17. LIMITATION OF ABSTRACT UU	15. NUMBER OF PAGES	19a. NAME OF RESPONSIBLE PERSON Thomas Zawodzinski
a. REPORT UU	b. ABSTRACT UU	c. THIS PAGE UU			19b. TELEPHONE NUMBER 865-974-2452

Report Title

An Integrated Computational and Experimental Approach Toward the Design of Materials for Fuel Cell Systems

ABSTRACT

The MURI set out with a series of objectives to construct a ‘theory toolkit’ coupled to advanced experimentation for validation and support. We have achieved all of our initial objectives in this regard and have expanded the scope of the MURI to use theory and experimentation to drive the prediction and preparation of new and highly active catalysts for key processes in fuel cells.

Succinctly stated, our theory and experimental goals were as follows:

Theory Objectives

- Accurate Quantum Mechanical Methods for Kinetics and thermodynamics
- ‘In silico’ Synthesis of Particle Structure
- Quantum Mechanical Electrocatalysis
- Ab initio Descriptions of Electron/Proton Transfer
- Predictive Catalysis: Multiscale Catalysis Model
- Data Mining Approaches to Predict New Materials

Experimental Objectives

- Theory Support
- Studies of Key Electrocatalytic Processes
- New Catalysts
- New Experimental Characterization of Structure

All of these objectives were achieved in the course of this project. We have reported a long series of innovations and, indeed, have extended this original list. Several of the investigators in the team have been cited as among the most productive ARO contractors.

Enter List of papers submitted or published that acknowledge ARO support from the start of the project to the date of this printing. List the papers, including journal references, in the following categories:

(a) Papers published in peer-reviewed journals (N/A for none)

Received

Paper

TOTAL:

Number of Papers published in peer-reviewed journals:

(b) Papers published in non-peer-reviewed journals (N/A for none)

Received

Paper

TOTAL:

Number of Papers published in non peer-reviewed journals:

(c) Presentations

Number of Presentations:

Non Peer-Reviewed Conference Proceeding publications (other than abstracts):

Received

Paper

TOTAL:

Number of Non Peer-Reviewed Conference Proceeding publications (other than abstracts):

Peer-Reviewed Conference Proceeding publications (other than abstracts):

Received Paper

TOTAL:

Number of Peer-Reviewed Conference Proceeding publications (other than abstracts):

(d) Manuscripts

Received Paper

TOTAL:

Number of Manuscripts:

Books

Received Paper

TOTAL:

Patents Submitted

Patents Awarded

Awards

Graduate Students

<u>NAME</u>	<u>PERCENT SUPPORTED</u>
FTE Equivalent:	
Total Number:	

Names of Post Doctorates

<u>NAME</u>	<u>PERCENT SUPPORTED</u>
FTE Equivalent:	
Total Number:	

Names of Faculty Supported

NAME

PERCENT SUPPORTED

FTE Equivalent:

Total Number:

Names of Under Graduate students supported

NAME

PERCENT SUPPORTED

FTE Equivalent:

Total Number:

Student Metrics

This section only applies to graduating undergraduates supported by this agreement in this reporting period

The number of undergraduates funded by this agreement who graduated during this period:

The number of undergraduates funded by this agreement who graduated during this period with a degree in science, mathematics, engineering, or technology fields:.....

The number of undergraduates funded by your agreement who graduated during this period and will continue to pursue a graduate or Ph.D. degree in science, mathematics, engineering, or technology fields:.....

Number of graduating undergraduates who achieved a 3.5 GPA to 4.0 (4.0 max scale):

Number of graduating undergraduates funded by a DoD funded Center of Excellence grant for Education, Research and Engineering:.....

The number of undergraduates funded by your agreement who graduated during this period and intend to work for the Department of Defense

The number of undergraduates funded by your agreement who graduated during this period and will receive scholarships or fellowships for further studies in science, mathematics, engineering or technology fields:

Names of Personnel receiving masters degrees

NAME

Total Number:

Names of personnel receiving PHDs

NAME

Total Number:

Names of other research staff

NAME

PERCENT SUPPORTED

FTE Equivalent:

Total Number:

Sub Contractors (DD882)

Inventions (DD882)

Scientific Progress

Technology Transfer

ARO-MURI Final Report

DAAD19-036-1-0169

An Integrated Computational and Experimental Approach Toward the Design of Materials for Fuel Cell Systems

PI

Tom Zawodzinski (CWRU)

Theory Team

Gerbrand Ceder (MIT), Nicola Marzari (MIT), Matt Neurock (UVA), Al Anderson (CWRU), and Gus Scuseria (Rice)

Experimental Team

Andrzej Wieckowski (UIUC), Sanjeev Mukerjee (Northeastern), Frank Ernst (CWRU) and Jay Mann (CWRU)

1. Executive Summary

The MURI set out with a series of objectives to construct a ‘theory toolkit’ coupled to advanced experimentation for validation and support. We have achieved all of our initial objectives in this regard and have expanded the scope of the MURI to use theory and experimentation to drive the prediction and preparation of new and highly active catalysts for key processes in fuel cells.

Succinctly stated, our theory and experimental goals were as follows:

Theory Objectives

- Accurate Quantum Mechanical Methods for Kinetics and thermodynamics
- ‘In silico’ Synthesis of Particle Structure
- Quantum Mechanical Electrocatalysis
- Ab initio Descriptions of Electron/Proton Transfer
- Predictive Catalysis: Multiscale Catalysis Model
- Data Mining Approaches to Predict New Materials

Experimental Objectives

- Theory Support
- Studies of Key Electrocatalytic Processes
- New Catalysts
- New Experimental Characterization of Structure

All of these objectives were achieved in the course of this project. We have reported a long series of innovations and, indeed, have extended this original list. Several of the investigators in the team have been cited as among the most productive ARO contractees.

2. Introduction and Overview of Approach

This MURI sought to identify and develop a set of validated theoretical and experimental tools and to use these tools in an integrated fashion to advance the science of electrocatalysis, with an emphasis on fuel cells.

Our program called for computational electrochemistry and catalysis tools that are applicable to real materials in actual fuel cell environments. As we began the program, an enormous gap existed between state-of-the-art theoretical tools and their applications to practical problems that would impact the design of catalysts and electrocatalysts for fuel cell systems. Relatively simple relationships, such as that between the 'd-band vacancy' and catalyst reactivity, were being promoted by Norskov et al. However, application of more sophisticated theory tools to provide meaningful predictive power, with validation, was lacking. This missing element required new theory tools or new applications of theory tools, informed by parallel experimental efforts, all applied to realistic materials and processes. We felt that this required the integration of knowledge from materials science, physics, chemistry, and engineering.

In response to this challenge we assembled an interdisciplinary team encompassing a diverse but complementary range of theoretical, experimental, and engineering skills. The team's strong and broad theoretical base (**Anderson**-CWRU, **Ceder**-MIT, **Marzari**-MIT, **Neurock**-UVA, **Scuseria**-Rice, **Zawodzinski**-CWRU) includes skills in all the necessary areas (materials structure, reaction chemistry and catalysis, improved quantum mechanical techniques, charge transfer and novel computational ensembles), and is coupled to unique world-class experimental capabilities in actual fuel cell measurements, characterization and engineering (**Mukerjee**-NE, **Wieckowski**-UIUC and **Zawodzinski**-CWRU). In the course of implementing this project at CWRU, we added the excellent microscopy capabilities of **Ernst** and the experience in colloid chemistry of **Mann**. The experimentalists had a track record of working closely with theorists to produce seminal information and many of the

theorists had demonstrated their ability to make suggestions for novel and improved engineering materials.

This program also required a unique blend of faculty and graduate students who, *first*, could generate the new adequate theory that can not only analyze materials performance but also provide guidance on for new catalytic materials, *second*, would conduct experiments as requested or expected by the theory, and *third*, embraced a interactive and cohesive spirit to overcome geographic differences. The latter was key to our assembling the first rank theorists and experimentalists of the team, who were not all found at a single or even small number of institutions.

In the following sub-sections, we describe the major program elements constituting our approach. These are derived from the initial proposal submitted for this program. The sub-sections are derived from reports and power point presentations of the Co-PIs received during the funding periods.

2.1 Theory Methodology

To meet the requirements of realistic calculation in the fuel cell environment, we identified a series of targets for theory development. These included:

- 1) **Accurate Quantum Mechanics** for **kinetic and thermodynamic** data: new exchange-correlation functionals, quantum Monte Carlo approaches, and quantum mechanical embedding schemes (to treat the reaction zone with high accuracy, while still providing a basic quantum mechanical description of the rest of the system) will be developed **(Scuseria and Marzari)**;
- 2) **Multi-scale modeling for the Structure of the Electrode/Catalyst**: interatomic potentials and charge transfer models derived from first-principles that can treat polarizable systems and metal/oxide interfaces **(Neurock)**. Effective Hamiltonian methods to equilibrate the shape and composition profile in multi-component nanoparticles **(Ceder)**, ab initio based analytical models to describe lateral interactions and alloying effects in atomistic simulations **(Neurock)**;
- 3) **Quantum mechanics for the electrochemical half cells under potentials**: Periodic-boundary approaches that explicitly treat non-periodic, finite external fields and applied potentials, overcoming one of the major limitations in the simulation of extended systems in the condensed phase **(Marzari, Neurock, Anderson and Scuseria)**;
- 4) First-principles derived novel descriptions for the mechanisms of **electron and cation charge transfer**. **(Anderson, Marzari, Ceder, and Neurock)**
- 5) **Data mining** approaches to correlate catalyst performance with calculated quantities, to rapidly screen new materials, compositions, and morphologies **(Neurock, Ceder)**;
- 6) **Predictive Catalysis Model**: A multiscale approach that uniquely integrates ab-initio methods to determine reaction kinetics, interatomic

potentials, molecular dynamics and simulated annealing methods to predict the most stable catalytic structures, and 3D kinetic Monte Carlo methods to simulate electrocatalytic performance at the anode and cathode. **(Neurock and Ceder);**

- 7) **Multiscale Model of Composite Electrode formation:** A multiscale approach that builds up the 3-D structure of catalyst layer using Hamaker/Landau-Lifshitz approach couple with MC description of lattice; MD simulations of particle-support interactions **(Mann, Zawodzinski).**

2.2 Experimental Methodology

An array of experimental measurements was brought to bear in this program. These had several goals, including augmenting the data available to benchmark and inform theoretical studies as well as driving fresh discovery. Materials preparation is also part of the MURI effort. Specific elements of the experimental effort include:

- 1) **Studies of Electrochemical Reactions at Anodes:** EXAFS analysis of metal coordination, EXAFS, XANES and NMR studies of electronic structure; vibrational spectroscopy (IR, far IR/synchrotron far IR, SFG and STM studies) of adsorbed intermediates; all coupled to probes of electrochemical reactivity. **(Wieckowski and Mukerjee)**
- 2) **Studies of Electrochemical Reactions at Cathodes:** EXAFS, XANES and NMR studies of electronic structure; Electrochemical reactivity of various alloys. **(Mukerjee, Zawodzinski);**
- 3) **Studies of Effects Arising from the Use of Nanomaterials:** HRTEM, high resolution electronic structure studies (EELS), experimental (spectroscopic) determination of electronic structure of colloid particles, interaction forces (Hamaker coefficients) to describe composite formation; studies of reactivity of catalysts in simulated FC environment; **(Zawodzinski, Mann, Ernst, Mukerjee);**

- 4) **New Electroanalytical Approaches:** Use of pulse voltammetry to obtain kinetic information in situ in the fuel cell; development of electroanalytical methods to probe specific mechanistic steps of anode reactions. (**Zawodzinski, Wieckowski;**

2.3 Novel Materials

The integration of these computational and theoretical developments with first class experimental efforts will lead to the rational design, synthesis and characterization of new materials for fuel cell systems including:

- 1) **Novel binary or ternary alloys** to replace Pt and other expensive noble metals with effective substitutes.
- 2) **New nanoparticle structures** obtained by experimental synthetic methods to enhance high reactivity facets in nanoparticles by shifting from cubo/octahedral structures to tetragonal ones.
- 3) **Tailored nanoparticles with sizes optimized for** the promising catalysts developed for specific fuels. Size and morphology will affect both cathode and anode catalysis. Nanoparticle modeling indicates that the abundance of low coordination surface sites is the most effective.
- 4) **Layered nanoparticle structures** with engineered superlattice sequences, as well as layer-by-layer self-assembling depositions (alloy nano-clusters in a polymer composite containing ionic and electronic conducting elements).
- 5) **New substrate** candidates including transition metal oxides or tailored carbon supports with specific acid/base and oxidation functionalities and/or substrates with strong metal-support interactions, including electronic/proton conducting polymers substrates.
- 6) **New synthetic procedures** and sequences of surface alloying-deposition-cementation to secure high activity and prevent catalyst corrosion.

- 7) **Novel supported molecular-based catalysts**, inspired by other nanoporous catalysts and enzymes.
- 8) **Advanced multifunctional catalysts** for internal fuel reforming.
- 9) **Optimal metal surface promoters** to enhance specific catalytic functionality.

2.4 Integrated Studies

A number of systems were chosen throughout the project to serve as the targets of our approaches. These served to benchmark and focus the project activities as well as to provide new insight into the chosen system. Though our annual 'focus projects' were not the sole focus of the effort of the entire team, we chose these as critical problems in the technology requiring investigation. In the first year of the project, the reaction pathway for methanol oxidation reaction was studied in depth by a combined effort of Neurock and Wieckowski. Other fuels studied at various stages included formic acid and ethanol. Year 2 of the project focused strongly on the oxygen reduction reaction. In all studies, initial work was carried out on Pt or Pt-alloy particles. For anode studies, Pt-Ru was a primary target, while Pt-Co, Pt-Cr and Pt-Ni alloys were among those studied for cathode reactions. As the project progressed, other emerging items of interest took the place of the originally planned 'Annual Problem' sequence. Thus, we studied (i) nano-scale aspects of the electrocatalysts, and the construction of composite electrodes; (ii) methods to simulate the real electrochemical interface including potential; and (iii) non-platinum group metal (NPGM) catalysts as important elements of the latter half of the project.

3. Results

3.1 Theory Development

A significant portion of the work of this MURI was the development and deployment of theoretical methods. In this section, we summarize the main results of the various investigations undertaken as per section 2.2 above. For each Target we provide a brief synopsis of the key achievement(s) and then a more detailed report (written by the main investigator(s)).

Target 1: Accurate Quantum Mechanics for kinetic and thermodynamic data:
New exchange-correlation functionals, quantum Monte Carlo approaches **Scuseria**

Synopsis:

A series of new functionals for use in density functional theory, rapid convergence algorithms and other methods were developed. The overall objective was to improve speed and accuracy of DFT calculations. A special focus was the relativistic correction for metals. These were then applied to a series of problems including oxide formation on metals and CO adsorption processes. The methods have been introduced into Gaussian.

Detailed Report:

CO adsorption on platinum surfaces is an important area of study in computational fuel cell research and is related to the development of novel materials. An interesting aspect of studying chemisorption of CO on Pt is that the density functional theory (DFT) tends to incorrectly predict the fcc-hollow sites to be the preferred adsorption sites whereas experiments clearly indicate adsorption of CO molecules on the atop sites of the Pt surfaces. Most of these studies have been carried out in the gas phase and are based on planewave methods using the LDA and GGA functionals. No hybrid functionals is known to be used in these studies as the use of hybrid functionals in planewave methods is prohibitively expensive. Hybrid functionals that include a portion of exact Hartree-Fock exchange contribution are found to improve energetics and level of accuracy for molecular and periodic systems. In this approach, Gaussian Type Orbitals (GTOs) and Periodic Boundary

Conditions (PBC) have been used. This investigation makes the first attempt to use hybrid functionals to study periodic systems that involve adsorption of fuel molecules on metal surfaces. Fast Multiple Method (FMM) helps to achieve linear scaling. Screened Exchange Hybrid functional (HSE) that have been developed earlier, can be conveniently applied to solid and metallic surfaces. A new basis set of Gaussian type have been developed for Platinum which overcomes the problems of numerical linear dependencies in periodic calculations. This basis set is highly accurate in producing the bulk properties of matter involving platinum and the quality of the results obtained using this in molecular calculations is similar to that of Stuttgart basis set. It can be assumed therefore that this basis set will perform very well in interfacial systems and as a benchmark it has been applied in calculating the ground state electronic property of platinum monoxide (PtO). PtO has attracted a lot of attention in recent years because of its potential use in important technological devices. It plays an important role in fuel-cell catalytic processes as well. Whether PtO is a metal or a semiconductor, however, is a matter of controversy until this day. In our research, several novel DFT exchange-correlation functionals as well as screened exchange hybrid functional (HSE) have been used for the first time to study this system. In agreement with the local spin density approximation (LSDA), the generalized gradient approximation (GGA) and the nonempirical meta-GGA functionals predict PtO to be metallic while the hybrid functional unequivocally predicts PtO to be a semiconductor with a band gap of 0.9 eV. This study reveals that improved functionals such as GGAs and meta-GGAs do not qualitatively improve the result obtained by LSDA for systems such as PtO. These results would help to predict the performance of density functionals in full-scale investigation on catalytic processes in the future. Some emerging issues such as the exclusive use of Scalar Relativistic and Spin-Orbit effects on chemisorption of CO on Pt(111) surface will also be discussed in this presentation.

Computational Methodologies: We have employed Density Functional Theory (DFT) methods using the *Gaussian* suite of programs.[1] *Gaussian* uses Gaussian type orbitals (GTOs) and employs periodic boundary conditions (PBC) methods.[2] Linear scaling is achieved by means of Fast Multipole Methods (FMM) algorithms.[3]

We have used several novel exchange-correlation functionals that have been developed in our group, in addition to the conventional Local Density Approximations (LDA)[4] and Generalized Gradient Approximations (GGA)[5]. The newly developed functionals are the Tao-Perdew-Staroverov-Scuseria (TPSS),[6] a meta-GGA functional, and the Heyd-Scuseria-Ernznerhof (HSE) functional,[7] a screened exchange hybrid. The meta-GGA performs better than GGAs to yield significant improvements in solids. Hybrid functionals that include a portion of exact-exchange are found to improve energetics and the band gaps in periodic systems.

Major Accomplishment and Highlights:

Over the past year, we have studied the performance of these novel density functionals for the following new materials: 1) Bulk platinum and palladium oxides 2) Bulk platinum nitride (PtN) 3) Molybdenum dichalcogenides 4) Polymeric nitrogen.

Moreover, we have studied the relativistic effects on Platinum dimer (Pt_2) using all-electron and valence basis set approaches.

Palladium and platinum monoxides (PdO and PtO): We have chosen the PtO system as a benchmark test for novel functionals because there exist contradictory observations in the experimental results. Four families of functionals that are mentioned above and a new GTO basis set that was developed by us for platinum have been used. Our calculations reveal that PtO has an antiferromagnetic ground state. The ferromagnetic phase is 2.1 eV/PtO higher in energy compared to the antiferromagnetic state. All non-hybrid functionals (LSDA, PBE and TPSS) agree well with each other and predict PtO to be metallic, while the hybrid HSE functional predicts PtO to be a semiconductor. The predicted band gap is 0.9 eV. This is in agreement with one of the reported experimental values. In order to investigate

whether oxygen vacancies are responsible for the metallic nature in the PtO as reported by one experimental study, calculations on oxygen deficient systems using the HSE functional have been performed and a reduced gap was obtained. This study reveals that the hybrid HSE functional separates valence and conduction bands from each other to create a band gap. Extended 6-311G(d) and 8-411G(d) basis sets along with 6-31G(d) basis set for oxygen have been used in this study. We found that 6-31G(d) basis set is sufficient for our calculations. We have extended our studies further to bulk PdO. In this study, a different approach was taken for the palladium basis set. We have truncated and modified most diffused exponents of palladium basis set from the one that was originally developed for molecular calculations. Bulk properties of Pd have been calculated using this basis set and the results have been compared with the ones obtained from an energy optimized basis set. These are in excellent agreement with experimental values as well. We confirm that for bulk properties, optimization of basis sets is not essential for periodic calculations. The band gap for PdO is found to be slightly smaller than that for PtO.

Platinum nitride (PtN): In this work we have studied bulk properties, phase transition pressure and electronic structures of zinc-blende and rock-salt phases of PtN. Our results predict that the zinc-blende type structure is energetically more stable than the rock-salt type structure. A remarkably high bulk modulus of 372(5) GPa, which is about 100 GPa higher than that for pure Pt has been confirmed by our calculations. The lattice constant calculated with PBE and TPSS agree well with the experimental result, while LSDA and HSE predict shorter values. Our PBE calculated value for lattice constant for the zinc-blende and rock-salt phases are very close to the value predicted independently by Sahu and Kleinman using the FLAPW and APW basis. The PBE and TPSS calculated values for bulk modulus the zinc-blende phase are 373 and 389 GPa, respectively. LSDA largely overestimate the bulk modulus. For rock-salt structures, the overall bulk modulus is much higher than zinc-blende phases. Again, we have found very good agreement between our calculated value for bulk modulus and those calculated with the FLAPW method and

APW basis set. PtN is predicted to be metallic by all functionals. Both phases have extended Pt *d* - N *p* hybridization.

Molybdenum dichalcogenides: Bulk properties of molybdenum dichalcogenides (MoS₂, MoSe₂ and MoTe₂) using novel functionals have been the main focus of this study. These complexes crystallize in the 2H-stacking sequence [XMoX · · · XMoX], where X is a chalcogen atom and the X-Mo-X sandwich layers are coupled by vdW forces. There exist strong covalent bonds within the layer in hexagonal arrays (quasi-2D structures). Metal atoms are coordinated in a trigonal prismatic fashion. It is known that density functional theory does not perform well for complexes that are separated by van der Waals gaps. From a theoretical point of view, it is very interesting to use novel density functional on such complexes. We have used all functionals described above for this work and optimized the energy of the lattice constants. Calculated and experimental lattice constants are in excellent agreement for the covalently bonded layers. However, lattice constants along the *c*-axis are largely overestimated. This overestimation comes from the interlayer distances that are separated by large van der Waals gaps. LSDA performs better compared to other functionals. In MoS₂ and MoSe₂ complexes, Mo atom acquires a minute net positive charge, while the opposite is found in MoTe₂ complexes. All complexes are found to be semiconductors with small band gaps, which vary with functionals.

Polymeric Phase of nitrogen: In this study we have calculated the energy storage capacity of the polymeric cubic gauche phase of nitrogen, which is a network of singly bonded nitrogen. Our results using PBE, TPSS and HSE functionals indicate that this form of nitrogen has a higher energy storage capacity than previously thought. PBE, TPSS and HSE functionals used in our study predict this value to be 3.14, 3.40, and 3.13 eV per N₂, respectively. LSDA predicts significantly lower energy storage capacity for this system, which is 1.91 eV/N₂. The calculated energy density for cg-N is found to be three times larger than that for TNT, RDX, and HMX. The high value of the bulk modulus confirms the stiffness of cg-N. The experimental bulk

modulus is best reproduced by TPSS and PBE functionals. Our results also suggest that much less energy can be stored at higher pressures. Zero point energy (ZPE) corrections are found to be important and in the case of Gaussian type orbitals, basis set super position errors (BSSE) must be taken into account.

Platinum dimer (Pt₂): The structure and thermochemistry of platinum dimer (Pt₂) have been calculated using a two-component self-consistent field method based on the third order nuclear-only Douglas-Kroll-Hess (DKH) approximation. The spin-orbit (SO) interaction is taken into account variationally employing a generalized Kohn-Sham scheme. Two all-electron basis sets with varying sizes (Malli Universal basis set: 29s27p20d16f and Gropen basis set: 21s17p12d7f) have been used. For comparison purposes, two effective-core potentials (ECPs) namely, LANL2DZ and Stuttgart, in conjunction with their valence basis sets have been used. For all-electron calculations, we have employed non-hybrid LSDA, PBE (GGA), TPSS (meta-GGA) functionals and hybrid B3LYP, PBE0, and TPSSh functionals. In case of ECP calculations, we have employed non-hybrid LSDA; PBE, BP86, and PW91 (GGA); VSXC and TPSS (meta-GGA) and hybrid B3LYP, HSE, PBE0, and TPSSh functionals.

Almost identical values for bond dissociation energy are predicted by the Malli universal basis set and the Gropen basis sets when scalar DKH approximations are used. Exchange-correlation functionals have significant effects on bond dissociation energy. The bond energy predicted by LSDA, PBE and TPSS are 5.05, 4.03 and 3.907, respectively. Hybrid B3LYP and PBE0 predict 3.06 and 3.02 eV/mol in case of Malli basis sets. The Spin-Orbit (SO) correction is found to be large. The SO correction is approximately 0.5-0.7 eV depending on the functionals used. The bond lengths calculated using all-electron basis sets are in excellent agreement. In case of ECP calculations, hybrid functionals underestimate the bond dissociation energy. B3LYP, HSE and PBE0 predict 2.50, 2.53 and 2.49 eV/mol bond energy. Interestingly, our newly developed hybrid TPSSh functionals predicts a value (2.93 eV/mol) that is close to the experimental value of 3.14 eV/mol. GGA functionals predict 3.40 eV/mol whereas LSDA severely overestimates (4.28 eV/mol). The novel TPSS functional

predicts 3.28, which is again in good agreement with experiment. All functionals predict a bond length that varies by 0.03 Å from the experimental value. No significant difference is found between ECP basis sets.

Future directions: We have started a theoretical study on both bulk and surface structures of RuS₂ complexes that have great potentials to be used in ORR catalysts. Bulk structure calculations have been performed using two modified Ru ECP basis sets derived from LANL2DZ and Stuttgart ECP basis sets. For S atom 31/31/1 valence basis set and 6-31G(d) basis sets are used. From comparative studies, modified LANL2DZ and 6-31G(d) basis set is found to best reproduce experimental lattice parameters, Ru-S, and S-S bond lengths. Our next step would be to study oxidation-reduction reactions (ORR) on RuS₂ (100), RuS₂ (111), and RuS₂ (210) surfaces.

References:

1. Gaussian Development Version, Revision B.07 and C.01, M. J. Frisch, G. W. Trucks, H. B. Schlegel, G. E. Scuseria, M. A. Robb, J. R. Cheeseman, J. A. Montgomery, Jr., T. Vreven, K. N. Kudin, J. C. Burant, J. M. Millam, S. S. Iyengar, J. Tomasi, V. Barone, B. Mennucci, M. Cossi, G. Scalmani, N. Rega, G. A. Petersson, H. Nakatsuji, M. Hada, M. Ehara, K. Toyota, R. Fukuda, J. Hasegawa, M. Ishida, T. Nakajima, Y. Honda, O. Kitao, H. Nakai, M. Klene, X. Li, J. E. Knox, H. P. Hratchian, J. B. Cross, C. Adamo, J. Jaramillo, R. Gomperts, R. E. Stratmann, O. Yazyev, A. J. Austin, R. Cammi, C. Pomelli, J. W. Ochterski, P. Y. Ayala, K. Morokuma, G. A. Voth, P. Salvador, J. J. Dannenberg, V. G. Zakrzewski, S. Dapprich, A. D. Daniels, M. C. Strain, O. Farkas, D. K. Malick, A. D. Rabuck, K. Raghavachari, J. B. Foresman, J. V. Ortiz, Q. Cui, A. G. Baboul, S. Clifford, J. Cioslowski, B. B. Stefanov, G. Liu, A. Liashenko, P. Piskorz, I. Komaromi, R. L. Martin, D. J. Fox, T. Keith, M. A. Al-Laham, C. Y. Peng, A. Nanayakkara, M. Challacombe, P. M. W. Gill, B. Johnson, W. Chen, M. W. Wong, C. Gonzalez, and J. A. Pople, Gaussian, Inc., Wallingford CT, 2004.
2. K. N. Kudin and G. E. Scuseria, *Phys. Rev. B* **61**, 16440 (2000).
3. (a) J. M. Millam and G. E. Scuseria, *J. Chem. Phys.* **106**, 5569 (1997), (b) J. C. Burant, G. E. Scuseria, and M. J. Frisch, *J. Chem. Phys.* **195**, 8969 (1996). (c) J. C. Burant, M. C. Strain, G. E. Scuseria, and M. J. Frisch, *Chem. Phys. Lett.* **258**, 45 (1996). (d) M. C. Strain, G. E. Scuseria, and M. J. Frisch, *Science* **271**, 51 (1996).

4. (a) J. C. Slater, *Quantum Theory of Molecular and Solids*; Vol. 4, The Self-Consistent Field for Molecular and Solids, McGraw-Hill, New York, 1974 (b) S. H. Vosko, L. Wilk, and M. Nusair, *Can. J. Phys.* **58**, 1200 (1980).
5. (a) J. P. Perdew, M. Ernzerhof, and K. Burke, *J. Chem. Phys.* **105**, 9982 (1996). (b) M. Ernzerhof, J. P. Perdew, and K. Burke, *Int. J. Quantum Chem.* **64**, 285 (1997).
6. (a) J. Tao, J. P. Perdew, V. N. Staroverov, and G. E. Scuseria, *Phys. Rev. Lett.* **91**, 146401 (2003). (b) V. N. Staroverov, G. E. Scuseria, J. Tao, and J. P. Perdew, *Phys. Rev. B*, **69**, 075102 (2004). (c) V. N. Staroverov, G. E. Scuseria, J. Tao, and J. P. Perdew, *J. Chem. Phys.* **119**, 12129 (2003).
7. (a) J. Heyd, G. E. Scuseria, and M. Ernzerhof, *J. Chem. Phys.* **118**, 8207 (2003). (b) J. Heyd and G. E. Scuseria, *J. Chem. Phys.* **120**, 7274 (2004).

Target 2: quantum mechanical embedding schemes (to treat the reaction zone with high accuracy, while still providing a basic quantum mechanical description of the rest of the system) will be developed (**Marzari**);

Synopsis:

Methods were developed to treat the electrochemical interface with greater accuracy and without major assumptions. First-principles methods were developed for the first time to treat the electron transfer process.

Detailed Report:

Electron-transfer diabatic free energy surfaces from first-principles molecular dynamics

P. H.-L. Sit (Department of Physics, MIT, Cambridge, MA 02139)

Matteo Cococcioni (DMSE, MIT, Cambridge, MA 02139)

Nicola Marzari (DMSE, MIT, Cambridge, MA 02139)

Electron transfer in aqueous solution is a fundamental process in physical chemistry, and since the introduction of Marcus theory it has been extensively studied using classical force-fields molecular dynamics. However, classical potentials contain fitted parameters, and have obvious limitations in describing structural effects related to hybridization and electronic polarization. In this work, we investigate electron transfer fully from first-principles, using the case of ferrous-ferric ions solvated in water as a paradigmatic example. The structure and dynamics of the aqua ions at ambient conditions are studied via Car-Parrinello molecular dynamics. The diabatic free energy surfaces in the limit of two ions infinitely apart are calculated with umbrella sampling, obtaining parabolic free energy curves, in agreement with Marcus theory. The extension of our approach to ions at finite distances is also discussed, and our solution to the specific challenges that this problem entails, ranging from self-interaction effects to localization constraints.

Target 3: Multi-scale modeling for the Structure of the Electrode/Catalyst:

interatomic potentials and charge transfer models derived from first-principles that can treat polarizable systems and metal/oxide interfaces (Neurock).

Synopsis:

This work was 'embedded' into other work by Neurock, Target 5.

Detailed Report:

See Target 5 for the report

Target 4: Effective Hamiltonian methods to equilibrate the shape and composition profile in multi-component nanoparticles (**Ceder**),

Synopsis:

Equilibrium models to explore the surface composition and segregation in alloys and oxides were developed. The effects of oxygen coverage and CO adsorption were investigated. Significant changes in the relative surface concentrations of different metals were induced by the presence of the adsorbates.

Detailed Report:

The objective of this work is to understand and predict the surface structure and composition of alloy catalysts, and relate it to performance. Currently, descriptions of the structure of alloy catalysts, such as Pt-Ru, range all the way from pure Pt surfaces to Pt cores with a Ru shell around it. Since the equilibrium structure of the catalyst may depend strongly on the environment with which the surface layer interacts, there is a need for a

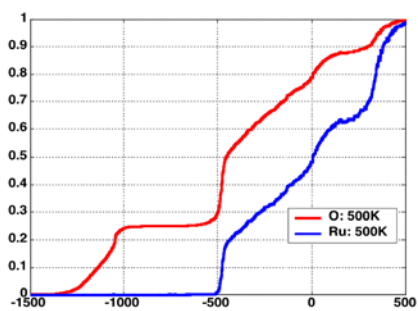


Fig. 1: Oxygen coverage (red) and Ru segregation (blue) as function of oxygen chemical potential in the environment.

comprehensive theory to describe and predict the equilibrium of alloy catalyst as a

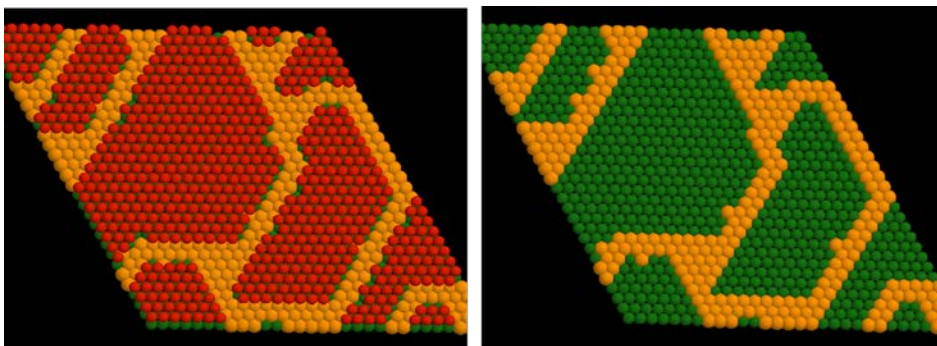


Fig. 2: Oxygen coverage (red) on a Pt-Ru alloy catalyst with underlying Ru (green) segregation. To make Ru visible in the left picture, oxygen was removed.

function of their chemical environment. In this project the formalism for the coupled

equilibrium between the metal surface layer and the surface adsorbants has been developed. This model derives its energetic input information from ab-initio Density Functional Theory (DFT) calculations, and can be used to evaluate the surface structure and adsorbate coverage at any temperature, and for any chemical potential of the adsorbate and catalyst alloying elements. A large amount of DFT calculations are mapped onto a coupled cluster expansion, with occupation variables describing the surface and adsorbate species. This coupled cluster expansion is then thermally equilibrated by Monte Carlo simulation.

Figure 1 shows the evolution of the surface of a Pt-Ru catalyst as function of the oxygen chemical potential in the environment at 500K. The Ru composition in the surface clearly tracks the oxygen adsorption. Figure 2 shows oxygen coverage of the catalyst surface (left figure) and the underlying Ru segregation (green). Oxidation of the catalyst pulls Ru to the surface. These initial results indicate there will be a significant effect of processing on the structure of these catalysts, and that there surface structure is likely to undergo slow changes when put in the operating conditions of a fuel cell. Future work will focus on other adsorbants and on relating these results to fuel cell performance.

Target 5 and 3: *Ab initio based analytical models to describe lateral interactions and alloying effects in atomistic simulations (Neurock);*

Synopsis:

Monte-Carlo-based simulated annealing methods were used to explore the surface composition and energetics of metal alloys. These method took advantage of newly developed EAM potentials describing various metals.

Detailed Report:

Theoretical Investigation of the Lowest Energy Structures of Nanoclusters of Pure Metals and Bimetallic Alloys:

Donghai Mei and Matthew Neurock

Department of Chemical Engineering and Department of Chemistry, University of Virginia, Charlottesville, VA 22904-4741

1. Introduction

The electrocatalytic behavior of metallic, bi- and multi-metallic nanoclusters is critically dependent upon their size, shape, composition and specific atomic arrangements. In addition, the synthesis of novel bimetallic nanoparticles can be controlled by the overall lowest energy structures that form. These nanometer size particles often display unique physical, chemical and catalytic properties. This motivation has invoked considerable investigations both experimentally and theoretically on the size-dependent optimum structures of transition metals and their alloys. Experimental techniques such as X-ray powder diffraction (XPRD), high-resolution transmission electron microscopy (HRTEM), and scanning tunneling microscopy (STM) have been used to provide spatial resolution that approaches the atomic level. Theory can be used to complement experimental studies by providing a critical analysis of the shape along with the explicit atomic structure and composition of the most stable nanoclusters that can form. Metallic nanoparticles, however, can be comprised of anywhere between 1 to 1000 atoms which can take on many different configurations with very similar energies. Screening through

these configurations in order to establish the lowest energy structures is a difficult challenge. The number of local minima grows exponentially with the number of atoms in clusters.

Traditional Metropolis Monte Carlo simulation methods¹ that are used to establish the low energy states for fluids or soft materials, start at low temperatures, or start in configurations that are far from the minimum energy structure can lead to local rather than global minimum. This is typically due the fact that the configurations that make the most important contributions to an ensemble average are those that are close to the minimum energy configuration. Traditional MC methods are inefficient at sampling configurations that require the ability to overcome high potential energy barriers. Simulated annealing,² basin-hopping³⁻⁶ and genetic⁷⁻¹⁴ algorithms, however, have helped in sampling phase space and identifying what appear to be more global minima. In the work described herein, we have developed a general Monte Carlo approach that can carry out simulated annealing to investigate the lowest energy structures of pure metal and bimetallic nanoclusters. The code is quite general and can, in principle, utilize a wide range of different interatomic potentials. More specifically, we have implemented and tested three different interatomic metal potentials: 1) embedded atom method (EAM) potentials,^{15,16} 2) n-body Gupta potentials¹⁷ and 3) Sutton-Chen potentials¹⁸. The Monte Carlo scheme employed herein can perform standard micro-ensemble (NVE) as well as canonical ensemble (NVT) simulations. In addition, we have developed a robust simulated annealing algorithm that can be used to help to establish the lowest energy structures. The Monte Carlo Simulated Annealing (MC-SA) is used herein to explore the optimum structures of different sized metallic and bimetallic nanoclusters. The simulation program can be used to study the optimum structures of 19 different pure transition metals and their binary alloys using EAM potentials developed by our colleague Professor Robert Johnson in the Department of Materials Science and Engineering at the University of Virginia. In addition to the MC-SA method development, we have carried out a range of ab initio density functional theoretical calculations for different structural arrangements of different bimetallic nanocluster in order to provide a database for comparison with the

structures and the energetics identified by the MC-SA approach. Herein we present simulation results for Pt, Ru, Au, Mo, and bimetallic Pt-Au, Pt-Ru, Pt-Mo nanoalloys. For Pt, Au, Ru and Mo clusters, the optimum structures and energetics of nanoclusters obtained from the simulation results are compared with first principles density functional theory calculations.

2. Monte Carlo Simulated Annealing Method

We have implemented a Monte Carlo simulated annealing (MC-SA) method to search the optimum cluster structure with global minimum energy. EAM, n-body Gupta and Sutton-Chen interatomic potentials were used in the simulation. The formalisms for the EAM and n-body Gupta potentials are given in Appendix A and B, respectively.

Simulated annealing is a generalization of the Monte Carlo method for examining the equations of state and frozen states of many body systems.¹ The concept is based on the manner in which liquids freeze or metals recrystallize in the process of annealing. In an annealing process, the melt, which is initially at a high temperature and disordered, is slowly cooled so that the system at any time is approximately in thermodynamic equilibrium. As cooling proceeds, the system becomes more ordered and approaches a "frozen" ground state at $T = 0$. Hence the process can be thought of as an adiabatic approach to the lowest energy state. If the initial temperature of the system is too low or cooling is too fast or inefficient, the system may become quenched forming defects or freezing out to form metastable states (i.e. trapped in a local minimum energy state).

In the original Metropolis scheme, an initial state of the system at thermodynamic equilibrium was chosen at energy E and temperature T , T is held constant while the initial configuration of the system is perturbed and the change in energy ΔE is computed. If the change in energy is negative, the new configuration is accepted. If the change in energy is positive it is accepted with a probability given

by the Boltzmann factor $\exp(-\Delta E/T)$. This process is then repeated over a number of times to provide sufficiently good sampling statistics for the current temperature. The temperature is then decreased by a small amount according to the cooling schedule and the sampling algorithm repeated. This process of cooling and re-equilibrating the system is repeated over and over according to the cooling schedule until one reaches the final $T=0$ frozen state.

Kirkpatrick and coworkers proposed a method of using a Metropolis Monte Carlo simulation to find the lowest energy (most stable) orientation of a system.² Their method is based upon a procedure that is used to make the strongest possible glass. This procedure heats the glass to a high temperature so that the glass is a liquid state and the atoms can move relatively freely. The temperature of the glass is slowly lowered so that at each temperature the atoms can move enough to begin adopting the most stable orientation. If the glass is cooled slowly enough, the atoms are able to "relax" into the most stable orientation. This slow cooling process is known as *annealing*, and so their method is known as *simulated annealing*.

The MC-SA algorithm used in this work can be described as follows:

- Step (1):** Initialize an arbitrary configuration for the cluster system at room temperature T_0 .
- Step (2):** Sample different state configurations using the Metropolis Monte Carlo algorithm with an acceptance probability of $\exp(-\Delta E/T_0)$.
- Step (3):** Replace T_0 with higher temperature $T_0 + \Delta T$ (heating rate, $\Delta T = 0.01$ K/step) and repeat the sampling again in step (2). Step (3) is repeated each time on the subsequent cluster configuration until the temperature of the system reaches the highest temperature T_{\max} (e.g. 1500 K)
- Step (4)** Sample different state configurations at T via a Metropolis Monte Carlo method with the acceptance probability of $\exp(-\Delta E/T_{\max})$ for 100,000 steps.

Step (5): Replace T_0 with a lower temperature $T-\Delta T$ (cooling rate $\Delta T = 0.001$ K/step) and repeat step (5). This step is repeated each time on the subsequent cluster configuration until the temperature of the system reaches at final equilibrium temperature T_f (e.g. 0.1 K)

Step (6): Sample the different state configurations at $T=0$ using the Metropolis Monte Carlo method with probability $\exp(-\Delta E/T_f)$ for 100,000 steps. The cluster structure with lowest configuration energy is obtained.

Generally five parallel simulation runs each starting with different structural configurations were performed. We also checked several factors that can affect the final optimum cluster structure. Different initial cluster structures and annealing schedules such as the choice of initial temperature, the number of iterations performed at each temperature, and the heating and cooling rates, were all explicitly tested. These effects are negligible on the simulation results reported here.

3. First Principles Calculations

First principle density functional theoretical calculations were performed herein by using DMol3 program.¹⁹ All atoms were described using double numerical basis sets which include d-polarization functions (DND) along with effective core potentials (ECP) to model the core electrons. All calculations were performed within the generalized gradient approximation (GGA) using the Perdew-Wang (PW91) exchange-correlation potential. Relativistic effects were treated using relativistic core pseudopotentials.^{20,21} This was particularly important for Au and Pt cluster calculations. The structure of cluster was optimized with a SCF energy convergence of 1.0×10^{-5} Hartree.

4. Results and Discussion

To validate EAM and n-body Gupta potentials and our simulation code, we first performed canonical Monte Carlo simulations of bulk Pt, Au, Ru, and Mo systems at room temperature. Simulation results of cohesive energies and equilibrium bond distances, along with experimental data and DFT calculations from the literature, are given below in Table 1. Since both of these two potentials were originally fit to bulk experimental data we expect to see good agreement. Small disparities between DFT results and experimental data were also found, especially for Au and Mo.

Table 1 Comparison of cohesive energies and equilibrium bond distances

	Cohesive Energy / eV/atom				Equilibrium Bond Distance / Å			
	Exp.	DFT	EAM	Gupta	Exp.	DFT	EAM	Gupta
Pt	5.77	5.45	5.77	5.72	2.77	2.81	2.77	2.75
Au	3.93	3.21	3.93	3.70	2.89	2.97	2.89	2.91
Ru	6.74	6.69	6.75	-	2.68	2.70	2.68	-
Mo	6.81	4.59	6.81	-	2.73	2.72	2.73	-
Ni	4.45	-	4.45	4.37	2.49	-	2.49	-

4.1 Pt Clusters

The optimal structures (lowest energy states) for Pt clusters of 2 to 38 atoms generated by our simulated annealing Monte Carlo simulations using EAM potential are given in Figure 1. The same structures also are obtained by using n-body Gupta potential. For Pt₃ to Pt₅ clusters, our simulated stable structures are in agreement with DFT-GGA calculations.²² The binding energies for DFT, and MC-SA (EAM) and MC-SA (Gupta) potentials are shown in Fig. 2. The MC-SA (EAM) calculated binding energies were found to be weaker than those reported from the DFT-GGA results.

Our simulated binding energies for Pt₄ and Pt₅ were found to be 1.80 eV/atom and 2.22 eV/atom respectively. The DFT values reported by Xiao and Wang were found to be 2.68 eV/atom (Pt₄) and 2.91 eV/atom (Pt₅).²² The lower binding energies for the EAM potential is likely due to the fact that the potentials were fit to the properties of the bulk metal systems. The embedded energy arising from local electron density for small clusters underestimated in the simulation using the EAM potentials. We also found that the simulated bond lengths are generally about 0.1 Å to 0.2 Å shorter than the DFT results. For Pt₆ cluster, our simulations using both EAM and n-body Gupta potentials predict a three dimensional bipyramidal stable structure. DFT calculations, on the other hand, predict a more stable planar structure.²² DFT results showed that the difference in the binding energy between the three dimension bi-pyramidal and the planar structure is 0.18 eV/atom where the two-dimensional structure is more stable.²² From Pt₇ cluster to Pt₅₅ cluster, both our simulations results as well as the previously reported DFT results find that the three dimension structures are more stable. The cluster shapes and the specific spatial configurations found for the DFT and MC-SA results were slightly different. The simulation results using EAM potential are in good agreement with DFT calculations as seen in Fig. 2. The binding energies found from by using n-body Gupta potentials within the MC-SA algorithm, however, were higher than those from DFT calculations.

4.2 Au Clusters

The lowest energy structures established from MC-SA simulations for Au clusters with sized between 2 to 38 atoms are given in Figure 3. Previous DFT calculations predict that small Au clusters (<13 atoms) prefer to adopt planar type structures^{21,23-27}. Our MC-SA simulation results, however, indicate that Au clusters between 4 to 13-atoms tend to adopt more three-dimensional structures. The difference is likely due to the fact that the EAM potentials were based on bulk Au whereby Au prefers a closed-packed arrangement.. Both the EAM and n-body Gupta potentials used in the MC-SA tend to overestimate the bulk properties of 3D

structure fail to predicted the most stable structures for small Au clusters. We have performed first principles calculations for various Au clusters which help to confirm previous theoretical results and are providing data to refine the EAM potentials

The binding energy of cluster generally increases with the cluster size. Our simulated binding energies for larger Au clusters in general agree with the DFT-LDA calculations (see Figure 4)²⁸ but it is well established the LDA overestimates the binding energy.

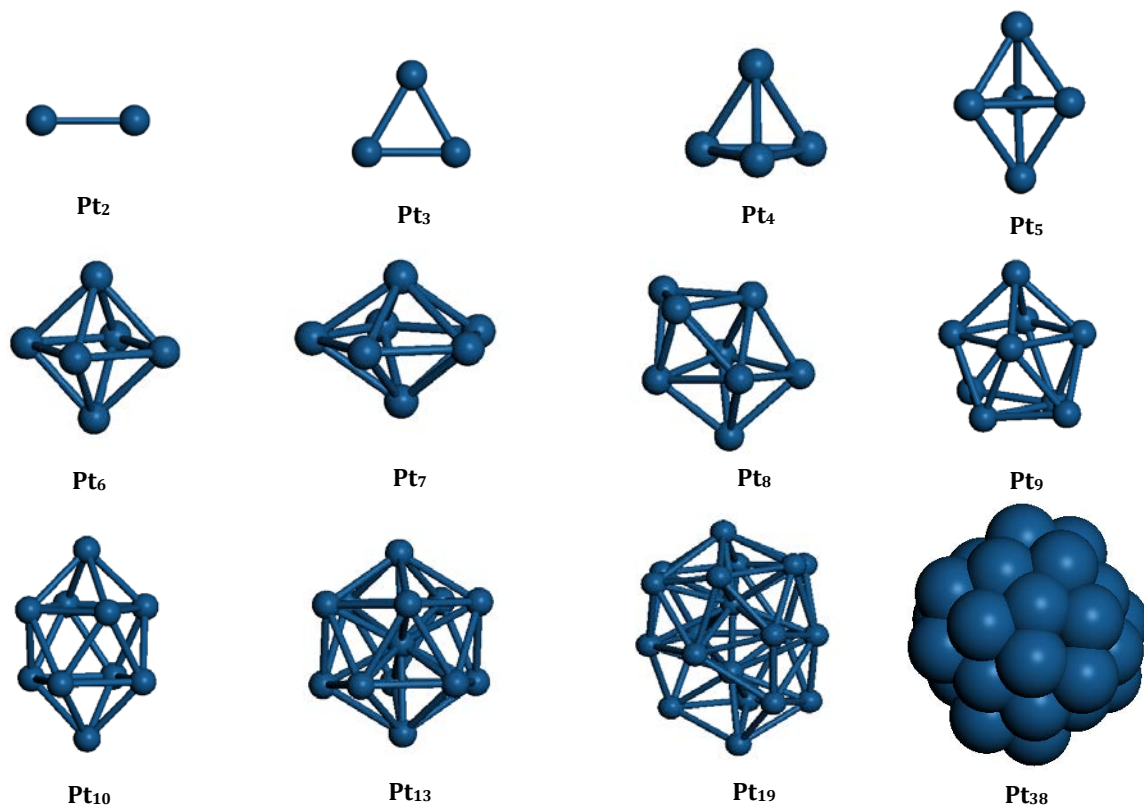


Fig. 1: Structures of lowest energy minima states for platinum clusters predicted by MC-SA simulations using an EAM potential for Pt.

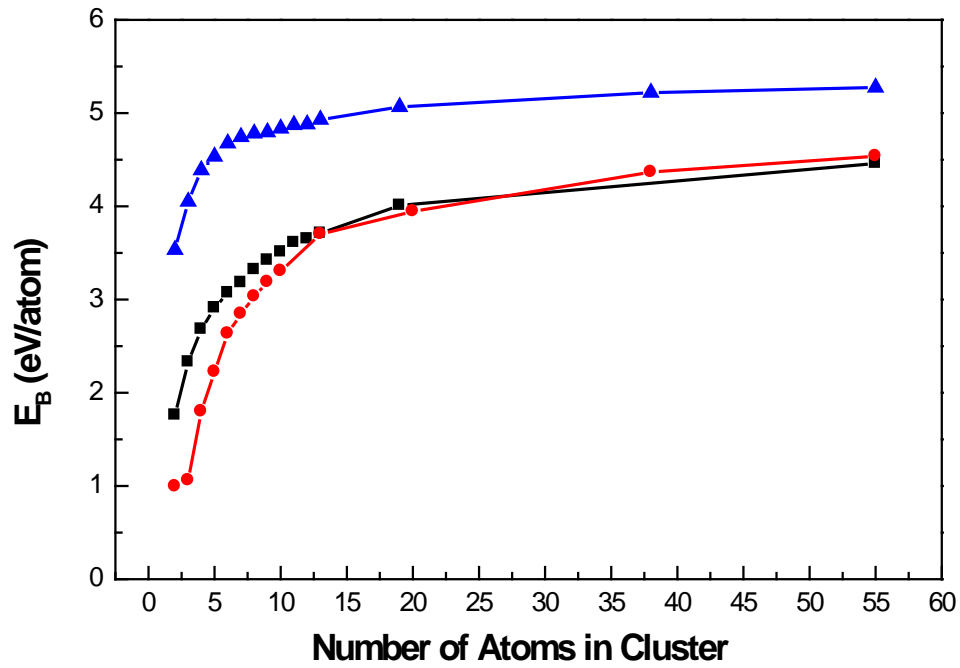


Fig. 2: Comparison of binding energies predicted from MC-SA simulations with EAM potentials and DFT calculations for platinum clusters. (■) DFT²² (●) simulation (EAM) (▲) simulation (Gupta)

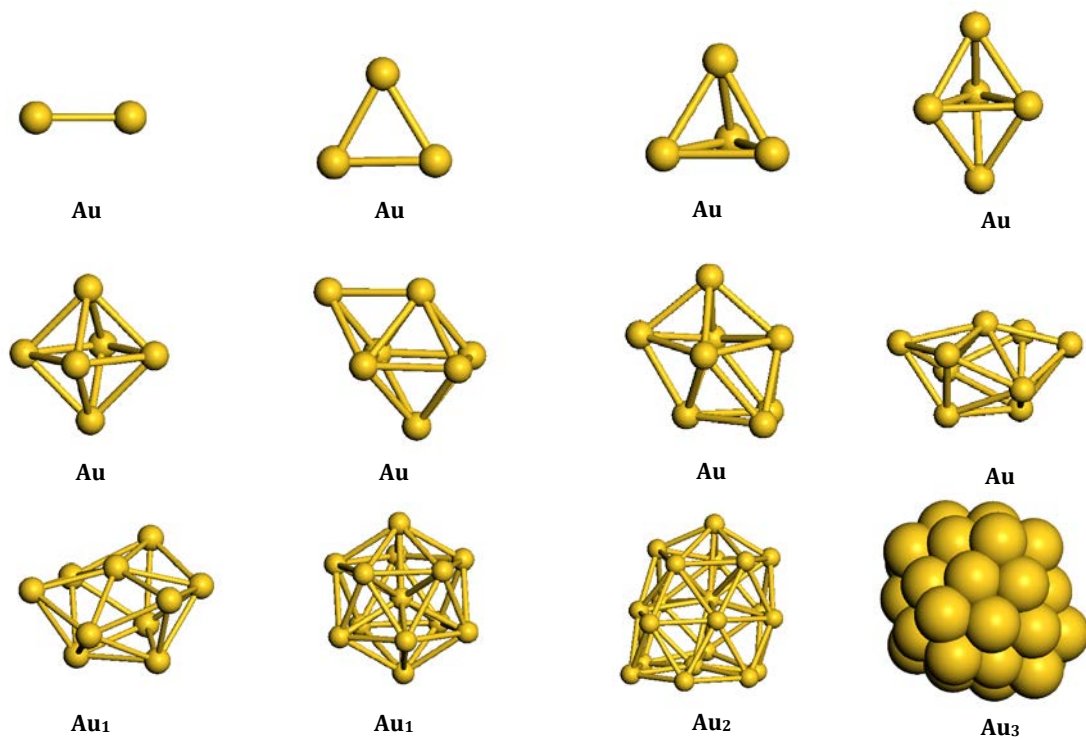


Fig. 3: Structures of the lowest energy minima for gold clusters predicted from MC-SA simulations using an EAM potential for Au.

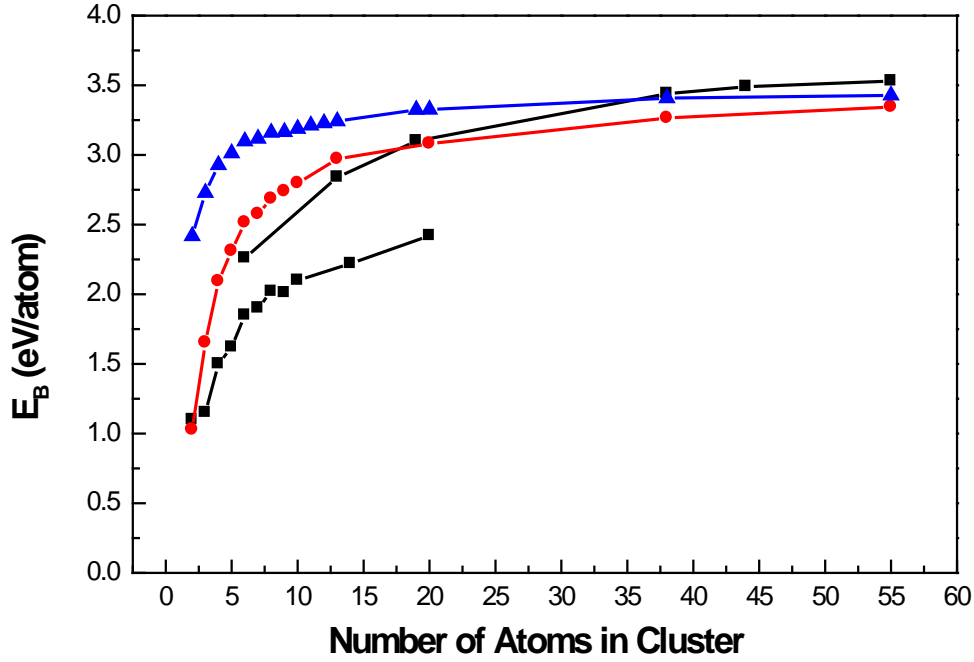


Fig. 4: Comparison of binding energies between simulations with EAM potential and DFT calculations for gold clusters. (■) DFT^{24,28} (●) simulation (EAM) (▲) simulation (Gupta)

The GGA calculated binding energies for Au clusters predict binding energies that are lower than the LDA as is expected and the experimental results.^{24,28} Similar to Pt clusters, the simulated results using n-body Gupta potential predicted higher binding energies, which were also shown in Figure 4.

4.3 Ru Clusters

The simulated structures with lowest energies for Ru clusters of 2 to 38 atoms using EAM potential are given in Figure 5. The clusters that form from the MC-SA simulations are three dimensional in shape and are in excellent agreement with DFT-GGA calculations.²⁹ The most stable structure for Ru cluster shifts from the simple cubic structure to icosahedron or cubo-octahedron when the cluster size

becomes larger. The most stable icosahedral structure for the Ru_{13} cluster predicted by the simulation was confirmed by DFT calculation.²⁹ The results in Figure 6 indicate the binding energies predicted from our MC-SA simulations are somewhat higher than those previously calculated using density functional theory.²⁹

4.4 Mo Clusters

The lowest energy structures simulated using the MC-SA simulation are nearly identical with those predicted for Ru. The lowest energy structure for Mo clusters made up of 2 to 38 atoms predicted using the MC-SA with the n-body Gupta potential are given in Figure 7. Our simulated stable structures also agree very well with DFT-GGA calculations.³⁰ The binding energies from simulations using n-body Gupta potentials, however, are higher than from the DFT-GGA results (Figure 8).

4.5 Pt-Au Clusters

Two sizes of Pt-Au clusters (13-atom and 55-atom) were studied in this work. For 13-atom bimetallic Pt-Ru clusters, both Monte Carlo simulations using EAM potential and DMOL3 calculations were performed. For 55-atom Pt-Ru clusters, only the simulation results are obtained at this time.

4.5.1. 13-atom Pt-Au Clusters

The simulated structures with lowest total energies for 13-atom Pt-Au clusters using EAM potential are given in Figure 9. Except for four clusters of Pt_8Au_5 , Pt_6Au_7 , Pt_5Au_8 and Pt_4Au_9 , the icosahedral

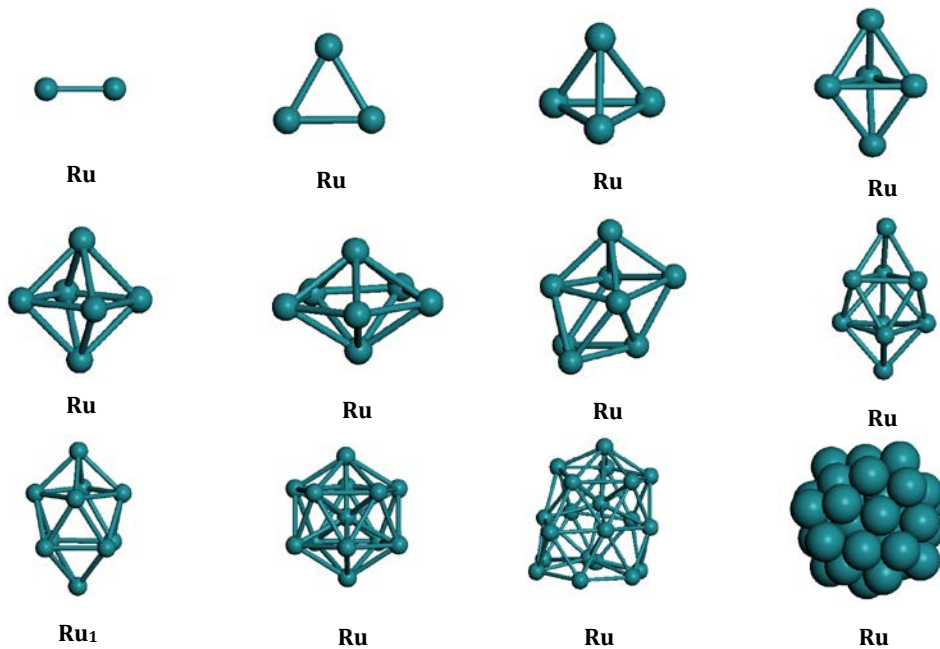
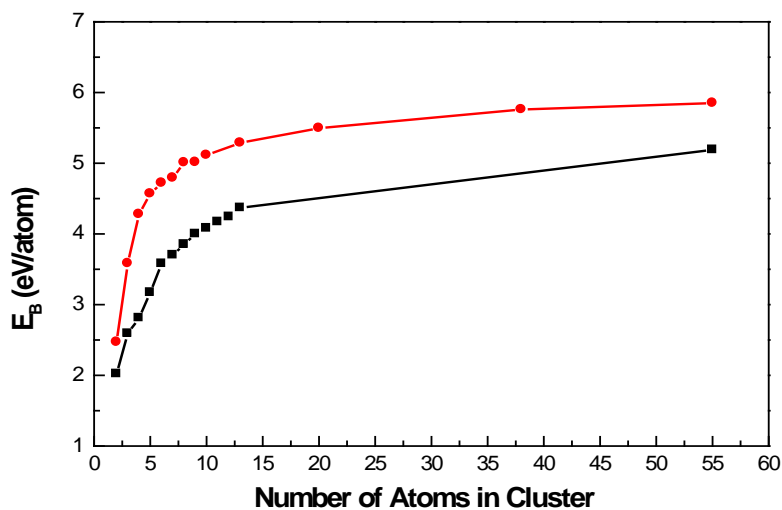


Fig. 5: Structures of global minima for ruthenium clusters by simulated annealing MC simulation using EAM potential



Fi. 6: Comparison of binding energies between simulations with EAM potential and DFT calculations for ruthenium clusters. (■) DFT²⁹ (●) simulation (EAM)

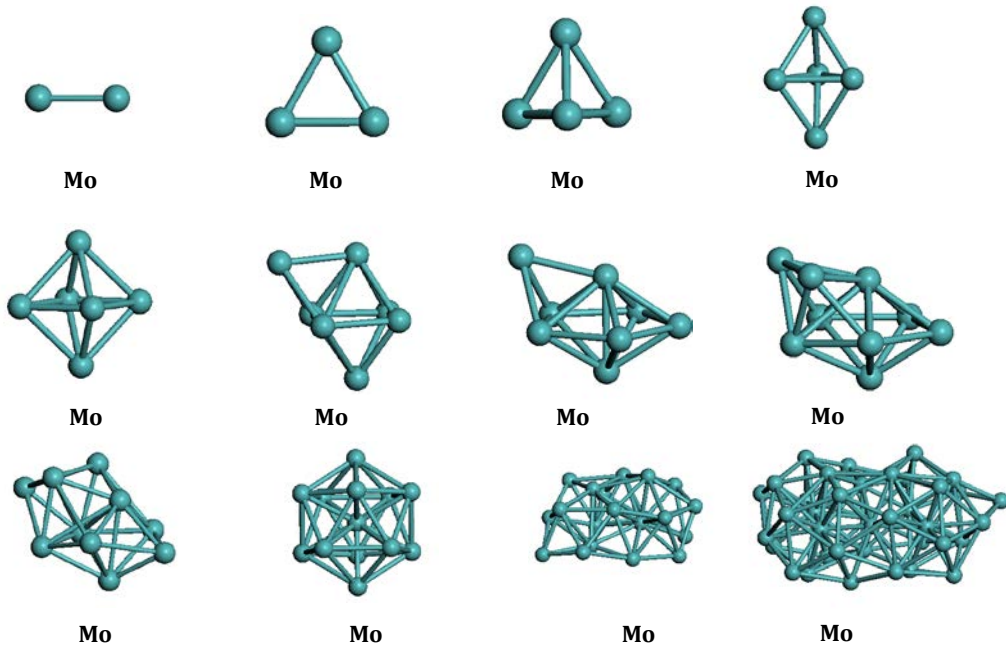


Fig. 7: Structures of global minima for molybdenum clusters by simulated annealing MC simulation using Gupta potential

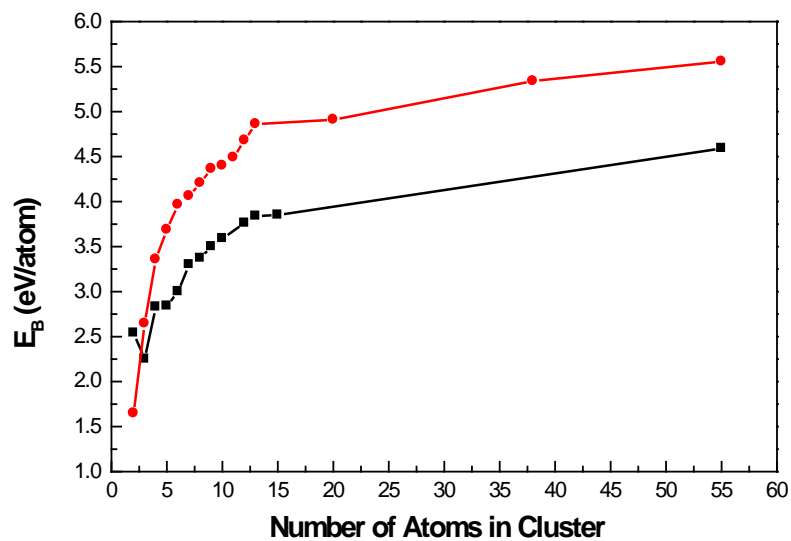
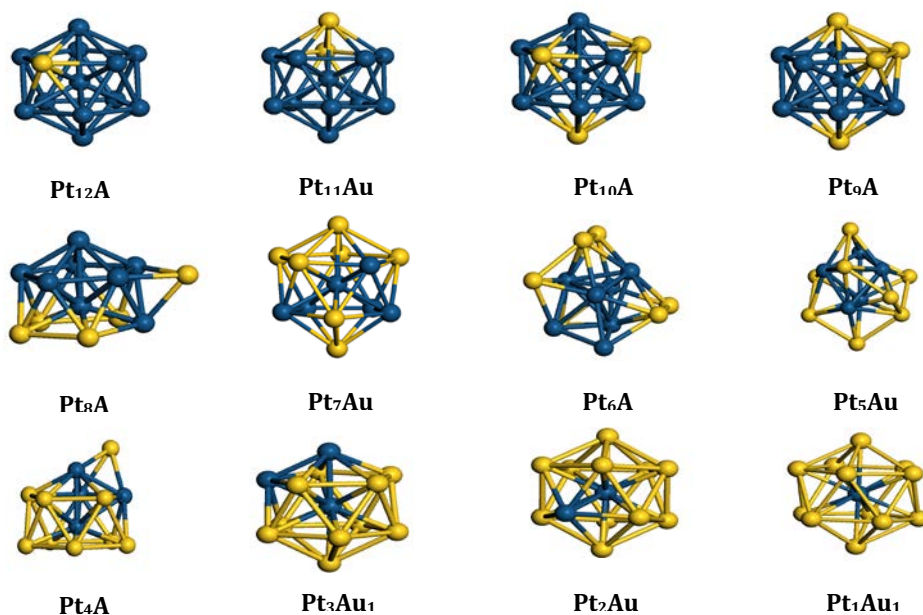


Fig. 8: Comparison of binding energies between simulations with EAM potential and DFT calculations for molybdenum clusters. (■) DFT³⁰ (ℓ) simulation (Gupta)



Fi. 9: Structures of global minima for 13-atom platinum-gold clusters by simulated annealing MC simulation using EAM potential

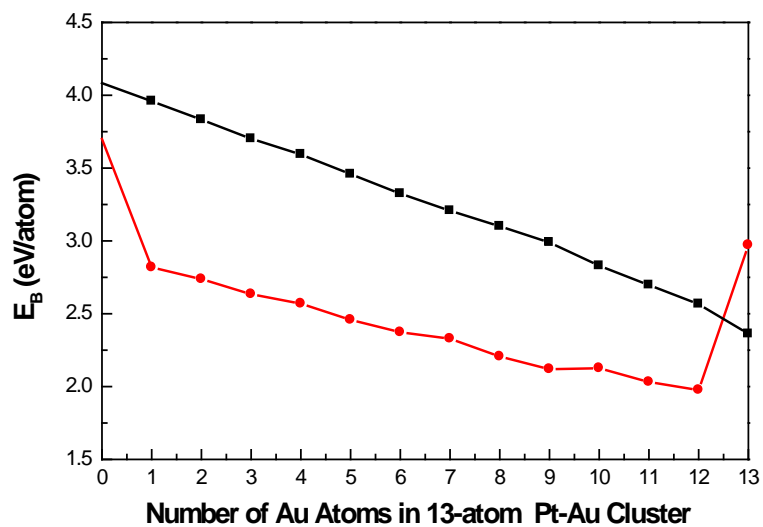


Fig. 10: Comparison of binding energies between simulations with EAM potential and DFT calculations for 13-atom bimetallic platinum-gold clusters. (■) DFT (●) simulation (EAM).

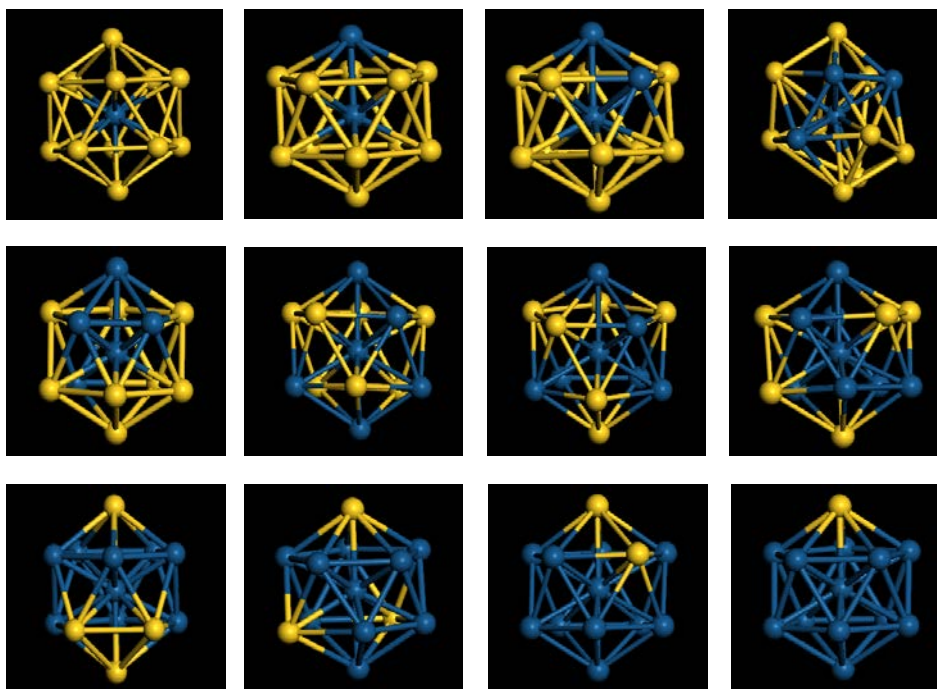


Fig. 11: Optimized structures of 13-atom bimetallic platinum-gold clusters by Dmol3 calculations

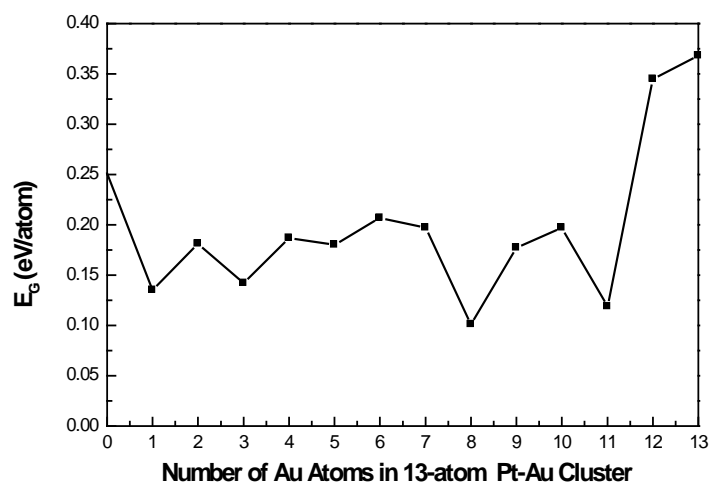


Fig. 12: HUMO-LUMO energy gap for 13-atom bimetallic platinum-gold clusters.

structures were found for all other 13-atom Pt-Au clusters. It had been found that Au atoms segregate to the surface of Pt-Au clusters. This is in agreement with previous first principles calculations³¹ and experimental observations. Increasing number of Au atoms in 13-atom Pt-Au clusters, the binding energy decreases. Figure 10 showed the calculated binding energies by DMol3 method are higher than the results by simulations with EAM potentials for the optimized icosahedral structures of 13-atom Pt-Au clusters (see Figure 11).

In order to confirm that the icosahedral structure is the most stable structure for all 13-atom Pt-Au clusters with all compositions, we performed DMol3 calculations for four non-icosahedral Pt-Au clusters predicted by simulations. For non-icosahedral structure Pt_4Au_9 clusters the binding energy is 3.03 eV/atom while the value of 2.99 eV/mol is obtained for icosahedral structure Pt_4Au_9 cluster. Similarly, DMol3 calculated the binding energies of 3.20 eV/atom, 3.50 eV/atom, and 3.59 eV/atom for non-icosahedral structures comparing to the values of 2.91 eV/atom, 3.32 eV/atom, and 3.46 eV/atom for icosahedral structures of Pt_5Au_8 , Pt_6Au_7 , Pt_8Au_5 clusters. This indicates that the non-icosahedral structure may be more stable than the icosahedral structure for 13-atom Pt-Au clusters with certain compositions. A more thorough investigation is under way.

The HOMO-LUMO energy gap by DMol3 calculations for 13-atom icosahedral Pt-Au clusters was shown in Figure 12. No explicit trend was found for 13-atom icosahedral Pt-Au clusters with different concentrations. Moreover, the relatively small HOMO-LUMO energy gap indicated that these 13-atom “perfect” icosahedral Pt-Au clusters have good electric conductivity.

4.5.2. 55-atom Pt-Au Clusters

The lowest energy structures for 55-atom Pt-Au clusters simulated using MC-SA with EAM potentials are given in Figure 13. Pt-rich structures were found to form well-defined 3D structures with well-defined surface facets. Au-rich clusters, on the other hand, tend to form more disordered and amorphous structures. The Au

atoms in these simulations tend to segregate to the outside. This is the result of higher surface free energies for Au over Pt. The results for both 13 atom clusters as well as 55 atom clusters see similar results. The results in Figure 14 indicate that the cluster binding energies increase with increasing Pt content as would be expected from the stronger Pt-Pt bond energy over that of Pt-Au and Au-Au bond energies.

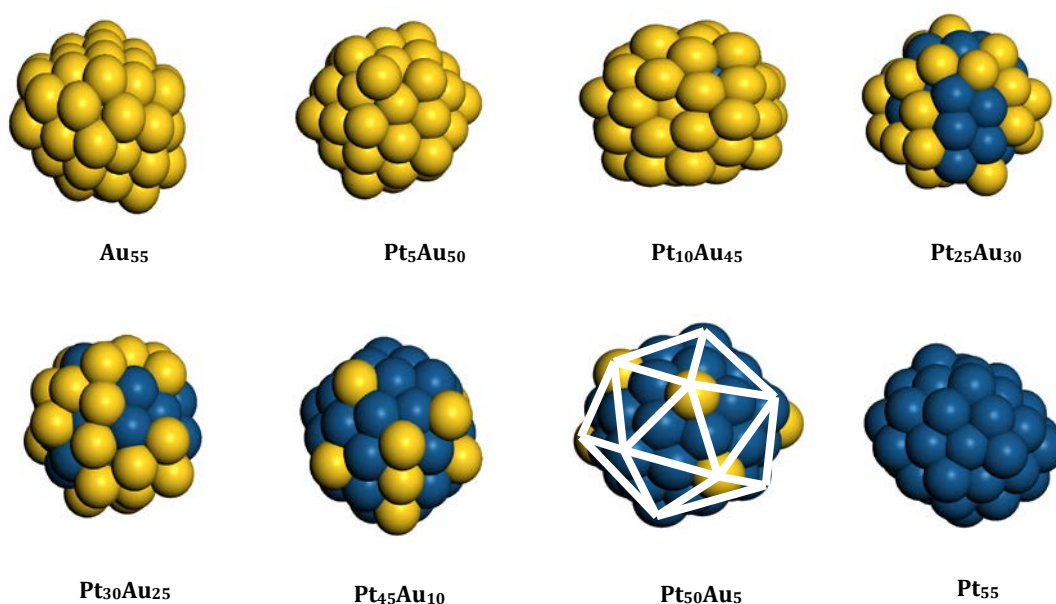


Fig. 13. Lowest energy structures for 55-atom platinum-gold clusters predicted from the MC-SA simulations using EAM potentials.

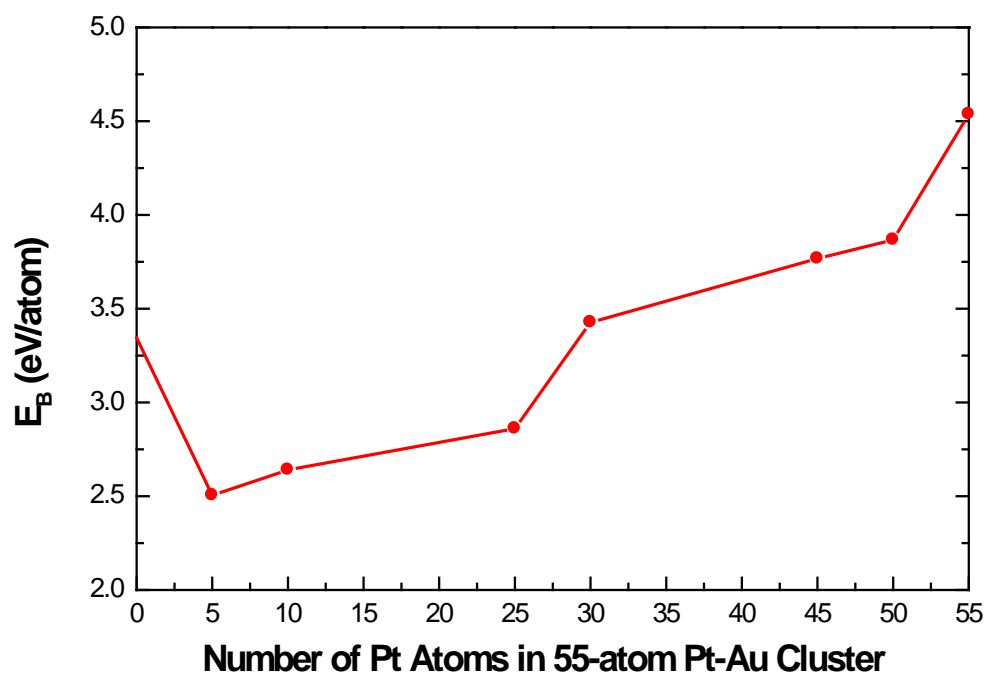


Fig. 14. The binding energies for 55-atom bimetallic platinum-gold clusters predicted from the MC-SA simulations with EAM potentials.

4.6 13-atom Pt-Ru Clusters

The lowest energies structures for 13 atom Pt-Ru clusters predicted by from the MC-SA simulations using EAM potentials are shown in Figure 15. The simulations predicted that Pt_4Ru_9 , $\text{Pt}_3\text{Ru}_{10}$, $\text{Pt}_2\text{Ru}_{11}$ and $\text{Pt}_1\text{Ru}_{12}$ clusters all like to form non-icosahedral structures while the other remaining 13-atom Pt-Ru clusters did form icosahedral structures. We also noticed that there was no consistent trend for Pt surface segregation was found in the simulated structures. The optimized icosahedral structures of 13-atom Pt-Ru clusters by DMol3 calculations were shown in Figure 16. The binding energy increases with the number of Ru atoms in 13-atom Pt-Ru clusters. Figure 17 compared the simulated binding energies with Dmol3 calculation results for 13-atom Pt-Ru clusters with icosahedral structures.

4.7. 13-atom Pt-Mo Clusters

The simulated structures with lowest total energies for 13-atom Pt-Mo clusters using EAM potential are given in Figure 18. Except for Pt_4Mo_9 , $\text{Pt}_3\text{Mo}_{10}$ and $\text{Pt}_2\text{Mo}_{11}$ clusters, the icosahedral structures were found for other 13-atom Pt-Mo clusters. The binding energy of 13-atom Pt-Mo cluster increases with Mo concentration (Figure 19).

5. Summary

A general Monte Carlo simulation approach has been developed to investigate the lowest energy structures of pure metal and bimetallic nanoclusters. A variety of interatomic potentials such as EAM, n-body Gupta potential and Sutton-Chen potential had been incorporated in the simulation program. By using simulated annealing MC method developed in this work, we can explore the optimum structure of metallic nanocluster with global minima. In this report, we present some of simulation results of pure Pt, Ru, Au, Mo, and bimetallic Pt-Au, Pt-

Ru, and Pt-Mo nanoalloys. For pure Pt, Au, Ru and Mo clusters, a systematic comparison between our simulation results and density functional theory calculations from literatures was given. For 13-atoms Pt-Au and Pt-Ru nanoclusters, we also use first principles density function theory method to calculate the optimized structures and surface segregations.

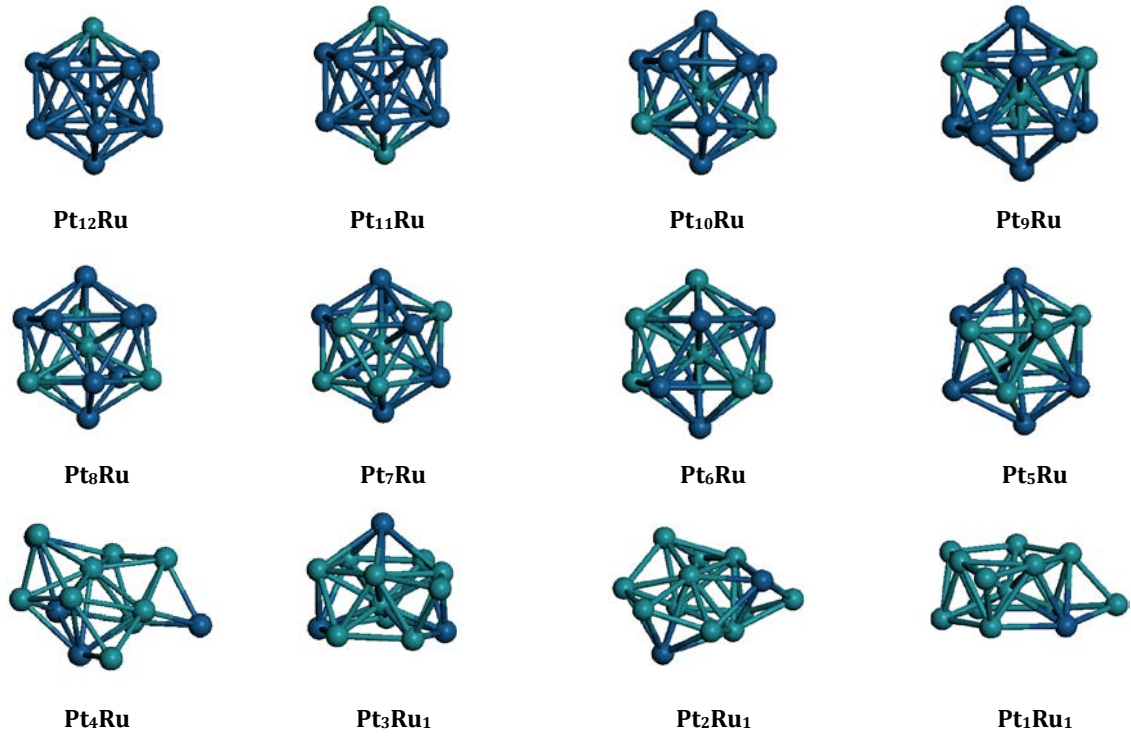


Fig. 15: Structures of global minima for 13-atom platinum-ruthenium clusters by simulated annealing MC simulation using EAM potential

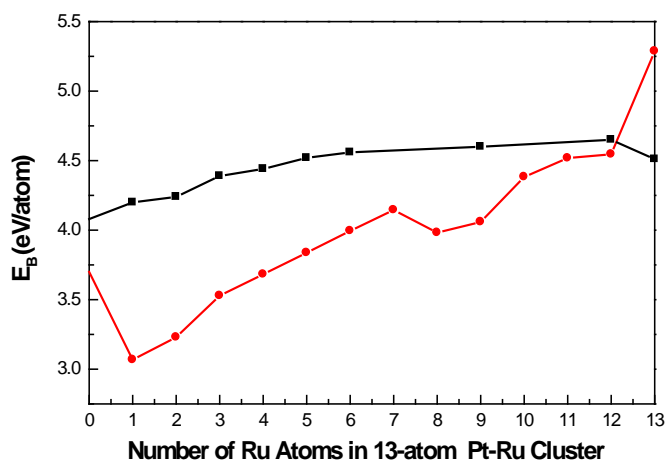


Fig. 16: Comparison of binding energies between simulations with EAM potential and DFT calculations for 13-atom bimetallic platinum-ruthenium clusters. (■) DFT (●) simulation (EAM)

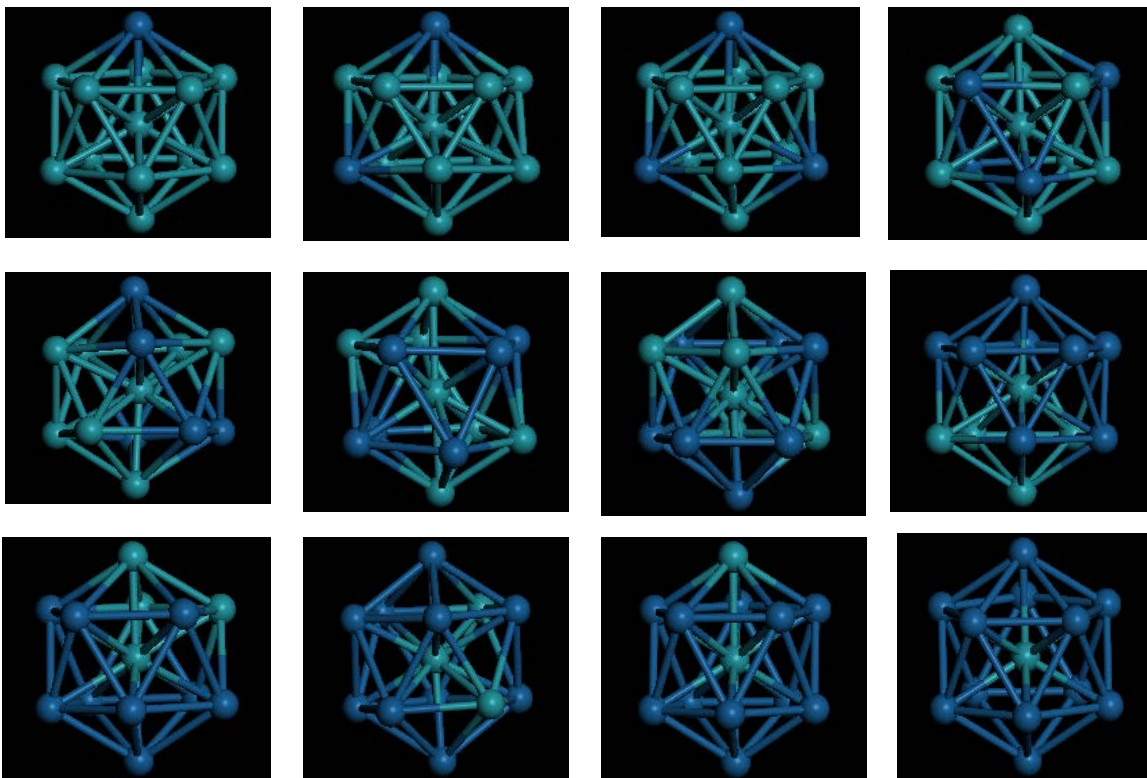


Fig: 17: Optimized structures of 13-atom bimetallic platinum-ruthenium clusters by Dmol3 calculations

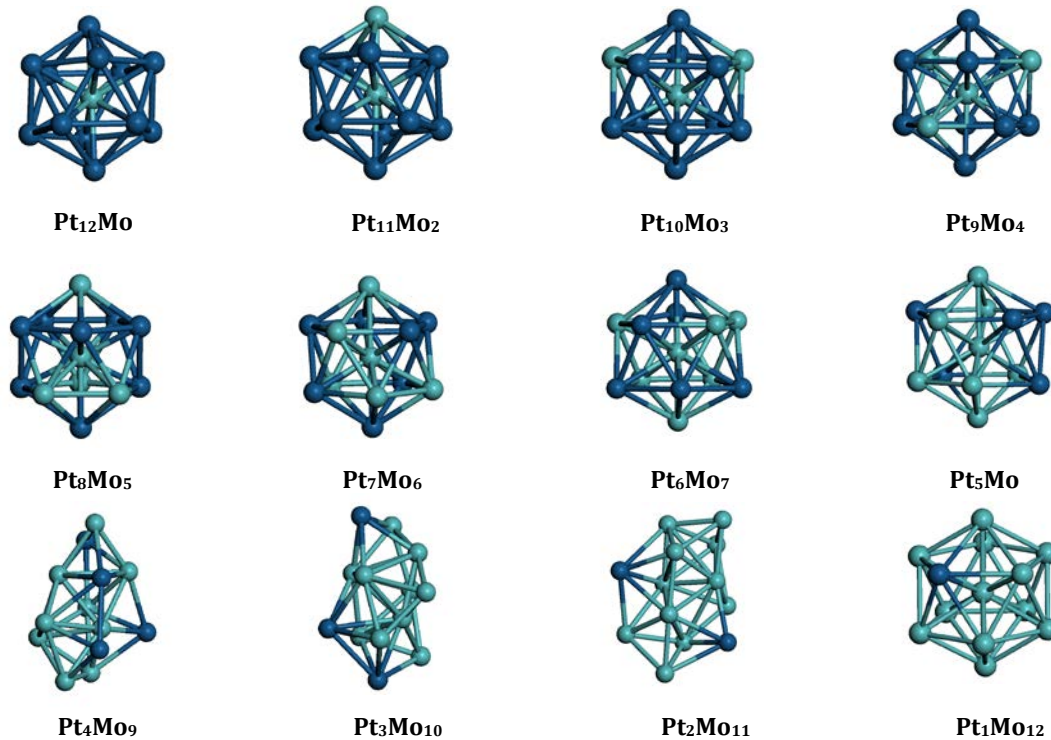


Fig. 18: Structures of global minima for 13-atom platinum-molybdenum clusters by simulated annealing MC simulation using EAM potential

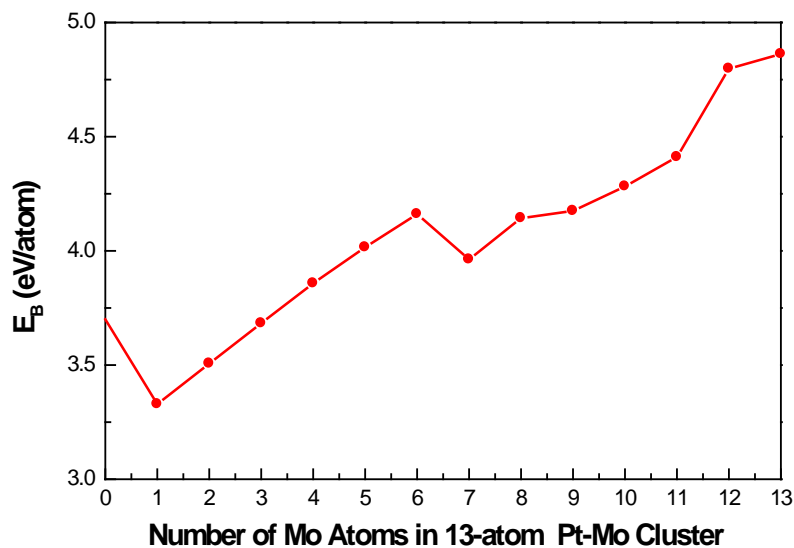


Fig. 19: Simulation results of binding energies for 13-atom bimetallic platinum-molybdenum clusters using EAM potential

References For the Section

1. Metropolis, N.; Rosenbluth, A. W.; Rosenbluth, M. N.; Teller, A. H.; Teller, E. *J. Chem. Phys.* **1953**, *21*, 1087.
2. Kirkpatrick, S.; Gelatt, C. D.; Vecchi, M. P. *Science* **1983**, *220*, 671.
3. Doye, J. P. K. *Phys. Rev. E* **2000**, *62*, 8753.
4. Doye, J. P. K.; Calvo, F. *J. Chem. Phys.* **2002**, *116*, 8307.
5. Doye, J. P. K. *Phys. Rev. B* **2003**, *68*.
6. Doye, J. P. K.; Wales, D. J.; Zetterling, F. H. M.; Dzugutov, M. *J. Chem. Phys.* **2003**, *118*, 2792.
7. Hartke, B. *J. Comput. Chem.* **1999**, *20*, 1752.
8. Lloyd, L. D.; Johnston, R. L.; Salhi, S.; Wilson, N. T. *J. Mater. Chem.* **2004**, *14*, 1691.
9. Lloyd, L. D.; Johnston, R. L.; Roberts, C.; Mortimer-Jones, T. V. *Chem. Phys.* **2002**, *3*, 408.
10. Lloyd, L. D.; Johnston, R. L. *J. Chem. Soc. Dalton Trans.* **2000**, 307.
11. Johnston, R. L. *J. Chem. Soc. Dalton Trans.* **2003**, 4193.
12. Johnston, R. L.; Mortimer-Jones, T. V.; Roberts, C.; Darby, S.; Manby, F. R. Application of Genetic Algorithms in nanoscience: Cluster geometry optimization. In *Applications of Evolutionary Computing, Proceedings*, 2002; Vol. 2279; pp 92.
13. Johnston, R. L. *Phil. Trans. Royal Soc. London Ser. A* **1998**, *356*, 211.
14. Massen, C.; Mortimer-Jones, T. V.; Johnston, R. L. *J. Chem. Soc. Dalton Trans.* **2002**, 4375.
15. Zhou, X. W.; Johnson, R. A.; Wadley, H. N. G. *Phys. Rev. B* **2004**, *69*.
16. Johnson, R. A. *private communications* **2005**.
17. Cleri, F.; Rosato, V. *Phys. Rev. B* **1993**, *48*, 22.
18. Sutton, A. P.; Chen, J. *Philos. Mag. Lett.* **1990**, *61*, 139.
19. *DMol³ is a density functional theory (DFT) package distributed by Materials Studio Modeling.*

20. Pyykko, P. *Chem. Rev.* **1988**, 563.
21. Hakkinen, H.; Moseler, M.; Landman, U. *Phys. Rev. Lett.* **2002**, 89.
22. Xiao, L.; Wang, L. C. *J. Phys. Chem. A* **2004**, 108, 8605.
23. Michaelian, K.; Rendon, N.; Garzon, I. L. *Phys. Rev. B* **1999**, 60, 2000.
24. Xiao, L.; Wang, L. C. *Chem. Phys. Lett.* **2004**, 392, 452.
25. Hakkinen, H.; Landman, U. *Phys. Rev. B* **2000**, 62, R2287.
26. Garzon, I. L.; Reyes-Nava, J. A.; Rodriguez-Hernandez, J. I.; Sigal, I.; Beltran, M. R.; Michaelian, K. *Phys. Rev. B* **2002**, 66.
27. Bravo-Perez, G.; Garzon, I. L.; Novaro, O. *J. Mol. Struct. Theochem* **1999**, 493, 225.
28. Haberlen, O. D.; Chung, S. C.; Stener, M.; Rosch, N. *J. Chem. Phys.* **1997**, 106, 5189.
29. Zhang, W. Q.; Zhao, H. T.; Wang, L. C. *J. Phys. Chem. B* **2004**, 108, 2140.
30. Zhang, W. Q.; Ran, X. R.; Zhao, H. T.; Wang, L. C. *J. Chem. Phys.* **2004**, 121, 7717.
31. Ruban, A. V.; Skriver, H. L.; Norskov, J. K. *Phys. Rev. B* **1999**, 59, 15990.

Appendix A: Embedded Atom Method (EAM)^{15,16}

In the EAM, the total energy E of the metal cluster is expressed as

$$(A.1) \quad E_{cluster} = \frac{1}{2} \sum_{i,j,j \neq i} \phi(r_{ij}) + \sum_i F(\rho_i)$$

where $\phi(r_{ij})$ represents the pair energy between i and j separated by a distance r_{ij} , and $F(\rho_i)$ is the embedded energy for the embedded an metal atom i into a local electron density associated with neighboring atoms. The electron density ρ_i can be calculated by

$$(A.2) \quad \rho_i = \sum_{j,j \neq i} f(r_{ij})$$

with $f(r_{ij})$ the electron density at the site of atom i arising from atom j at a r_{ij} distance away. The pair energy $\phi_{ij}(r_{ij})$ can be calculated by

$$(A.3) \quad \phi(r_{ij}) = \frac{A \exp[-\alpha(r_{ij}/r_e - 1)]}{1 + (r_{ij}/r_e - \kappa)^{20}} - \frac{B \exp[-\beta(r_{ij}/r_e - 1)]}{1 + (r_{ij}/r_e - \lambda)^{20}}$$

where r_{ij} is the equilibrium spacing distance between nearest neighbors. A, B, $\alpha, \beta, \kappa, \lambda$ are six adjustable parameters. For alloys, the generalization of pair energy potential between different metal species a and b is expressed as

$$(A.4) \quad \phi^{ab}(r) = \frac{1}{2} \left[\frac{f^b(r)}{f^a(r)} \phi^{aa}(r) + \frac{f^a(r)}{f^b(r)} \phi^{bb}(r) \right]$$

where $f^a(r)$ and $f^b(r)$ can be calculated by

$$(A.5) \quad f(r_{ij}) = \frac{f_e \exp[-\beta(r_{ij}/r_e - 1)]}{1 + (r_{ij}/r_e - \lambda)^{20}}$$

The embedded energy need three equations to smooth the potential slope over a wide electron density range. These equations are

$$(A.6) \quad \begin{aligned} F(\rho_i) &= \sum_{i=0}^3 F_{ni} (\rho_i / \rho_n - 1)^i & \rho < 0.85\rho_e \\ F(\rho_i) &= \sum_{i=0}^3 F_i (\rho_i / \rho_e - 1)^i & 0.85\rho_e \leq \rho < 1.15\rho_e \\ F(\rho_i) &= F_e [1 - \ln(\rho_i / \rho_s)] (\rho_i / \rho_s)^\eta & \rho > 1.15\rho_e \end{aligned}$$

where $\rho_e, \rho_n, \rho_i, F_{ni}, F_i$ and F_e are fitted parameters

Appendix B: N-body Gupta Potential¹⁷

The n-body Gupta potential derived from the tight-binding second-moment model. The total energy of metal cluster can be written as a summation of each atom i

$$(B.1) \quad E_{cluster} = \sum_i^N \{E^r(i) - E^m(i)\}$$

where the repulsive term E^r and the attractive term E^m are given below

$$E^r(i) = \sum_{j, j \neq i}^N \left\{ A(i, j) \exp \left[-p(i, j) \left(\frac{r_{ij}}{r_0(i, j)} \right) - 1 \right] \right\}$$

(B.2)

$$E^m(i) = \left\{ \sum_{j, j \neq i}^N \zeta^2(i, j) \exp \left[-2q(i, j) \left(\frac{r_{ij}}{r_0(i, j)} \right) - 1 \right] \right\}^{\frac{1}{2}}$$

(B.3)

In equations B.2 and B.3, r_{ij} is the distance between atoms i and j , and A , r_0 , ζ , p and q are fitted by experimental data for bulk structure

Target 6: Quantum mechanics for the electrochemical half cells under potentials: Periodic-boundary approaches that explicitly treat non-periodic, finite external fields and applied potentials, overcoming one of the major limitations in the simulation of extended systems in the condensed phase; **Marzari, Neurock, and Anderson**

Synopsis:

A variety of approaches were developed to treat and explore the effects of potential on reactivity patterns revealed by computational studies. In this work, fields were explicitly added via adjustment of boundary conditions.

Detailed Reports:

First-principles derived novel descriptions for the mechanisms of **electron and cation charge transfer. (Anderson, Marzari, Ceder, and Neurock)**

One set of tools and techniques has involved the study of chemical reactions in a solvated environment [3,4], developing both an extensive explicit study of the thermodynamic properties of liquid water [3], and an efficient solvation model that, for the first time, can be applied in periodic boundary conditions [4]. This has led to the first-ever determination from first-principles of the full diabatic free energy surfaces of an electron-transfer reaction in the presence of a liquid solvent (water, [2]). All these activities were necessary and preliminary to our current study of the oxygen-reduction reaction at the platinum-water interface, fully from first-principles.

The last methodological accomplishment [1] has shown how a self-consistent Hubbard U extension to density-functional theory allows to calculate with great accuracy (much superior to common approximation, such as GGAs and B3LYP hybrid functionals) the structure, energetics, and multiplet splitting of transition metal complexes.

We are now applying these techniques to study what we believe is our paradigm for improved activity at the electrode: bimetallic nanoparticles where a core bulk metal is surrounded by a 1- to 2- atomic layers thick skin of platinum. The rationale

for this is that while at higher thicknesses, the outer platinum layer will change its catalytic properties only due to the strain and morphology effects that the core of the nanoparticle induces, at a thickness of 1- to 2- layers, the bimetallic system acquires properties that are different from either the strained skin, or from the alloy. Our initial calculations show how the catalytic activity and resistance to poisoning can be simultaneously optimized for such system. So, we are pursuing the study of bimetallic nanoparticles both at the anode and at the cathode, and will complement this. The final challenge will be to design a system for which the outer layer is either resilient to dissolution, or that exhibits slow release and segregation from a core alloy.

Our goal is to describe accurately with large-scale first-principles molecular dynamics the electrochemical environment, to follow the dynamical and thermodynamical evolution of adsorbed species and to elucidate complex reaction pathways in the aqueous environment.

For this purpose, we have developed several of the novel tools needed to address this complexity. Validation of the microscopic structures is then given by comparison between predicted and measured spectroscopic information. In particular, we have developed and coded in our electronic-structure tools the algorithms needed for

- Full ab-initio molecular dynamics in metals, with efficient and strictly variational dynamical evolution of wavefunctions, subspace rotations, and occupation numbers (ensemble-DFT). This is the core tool needed to simulate efficiently and robustly large-scale systems.
- Finite electric fields in periodic boundary conditions, via the minimization of an electric enthalpy functional, where the macroscopic polarization is given by a single-point Berry phase of the wavefunctions

- Coupling quantum-mechanical modeling with a mesoscopic environment, via the introduction of
 - Tunable pseudometal potentials for the catalyst
 - Periodic-boundary continuum solvation models for water or electrolytes (LLNL collaboration, non-MURI)

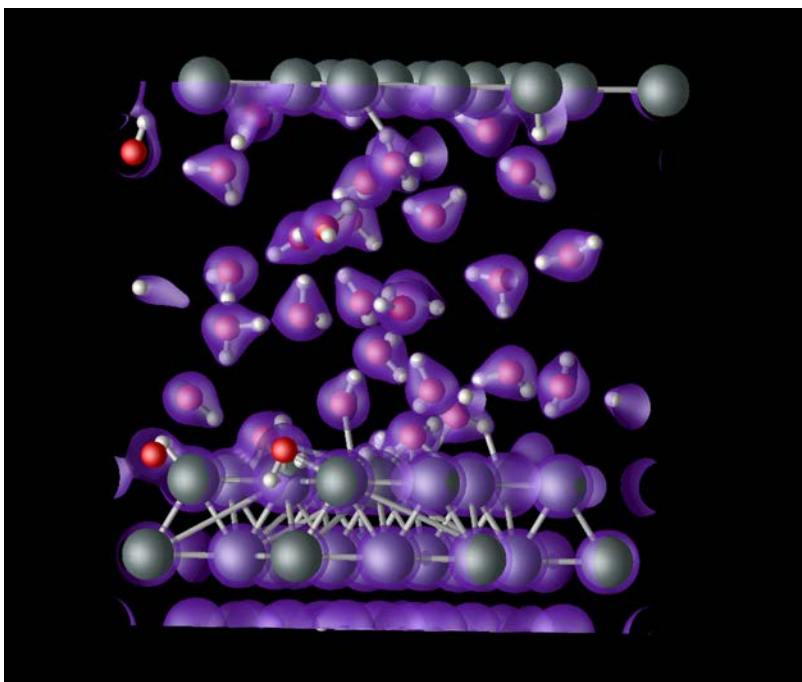


Fig. 1: Dynamical evolution of the interface between Pt(111) and water

First-principles spectroscopic predictions are then compared to available experimental data. As an example, we report here the exceptional degree of site-recognition found for CO adsorbed on Pt(111) or Ru-islands on Pt(111), together with experimental results found in Wieckowski group.

Freq (cm ⁻¹)	Ontop	Ontop 1ML Ru	Bridge	Fcc
DFT-PBE	2051	1978	1851	1757
Expts.	2063-2070	1967-2003	1828-1852	1764-1782

Table: Predicted (DFT-PBE) and measured (Wieckowski) vibrational frequencies for CO adsorbed on different surface sites on Pt(111) and on Ru-island covered Pt(111).

Target 7: linear free energy relationships to correct for potential changes (**Marzari, Neurock, Anderson**);

Synopsis:

A variety of approaches were developed to treat and explore the effects of potential on reactivity patterns revealed by computational studies. In this work, 'ad hoc' linear free energy corrections to calculated energies were used to estimate the effects of potential on the reactions.

Detailed Report:

Anderson For studies of Oxygen electro reduction over platinum and platinum alloys in acid, a collaborative theoretical-experimental interaction with Sanjeev Mukerjee was completed wherein new experimental results were obtained for comparison with theory. Activation energies for carbon supported Pt, Pt-Co, and Pt-Fe nanoparticles in 1 M trifluoromethane sulfonic acid were measured at four different electrode potentials, and they showed increases with electrode potential similar to the theoretical values.

Activation energies predicted from Tafel data by means of the above Arrhenius formula paralleled the potential dependence of the theoretical activation energies, indicating that in the 0.8-0.95 V range the active site density is ~constant.

Formation of the OH(ads) on the platinum skin on a platinum-cobalt alloy was probed in a collaborative theoretical-experimental interaction with Sanjeev Mukerjee was completed wherein VASP slab-band calculations were used to *predict a higher onset potential for OH(ads) formation on the Pt skin on Pt₃Co, which in turn explained the experimental observation of a decreased overpotential for O₂ reduction on the alloy.*

Target 8: Data mining approaches to correlate catalyst performance with calculated quantities, to rapidly screen new materials, compositions, and morphologies (**Neurock, Ceder**);

Synopsis:

A rapid predictive approach was developed to allow us to determine promising new compositions for reactions. This led to the expectation that adding Au to PtRu alloys would enhance methanol oxidation kinetics. This was verified by work at Johnson-Matthey. However though the intrinsic rate was indeed substantially higher, the difficulty of maintaining suitable surface compositions essentially 'washed out' the enhancement.

Detailed Report:

A computational method has also been developed to efficiently screen various metals for catalytic activity for CH₃OH dehydrogenation and H₂O activation and is based on a simple thermodynamic cycle utilizing computationally-fast vapor-phase periodic-slab calculations in addition to estimates for solution-phase contributions. The overall activity is found to be dependent on both the energy of C-H or O-H cleavage and the ability of the metal to accept an electron. The energy of O-H cleavage is favored for upper-left Pt-group metals and of C-H cleavage is favored for lower-left Pt-group metals. Preliminary results have been determined for Cu(111), Ru(0001), Pd(111), Pt(111) and Au(111) and show that H₂O activation is favored over Ru and Rh, due to intermediate work function combined with favorable OH activation and that CH₃OH dehydrogenation is favored over Pt and Pd due to their high work function.

Target 9: Predictive Catalysis Model: A multiscale approach that uniquely integrates ab-initio methods to determine reaction kinetics, interatomic potentials, molecular dynamics and simulated annealing methods to predict the most stable catalytic structures, and 3D kinetic Monte Carlo methods to simulate electrocatalytic performance at the anode and cathode. **(Neurock)**

Target 10: Multiscale Model of Composite Electrode formation: A multiscale approach that builds up the 3-D structure of catalyst layer using Hamaker/Landau-Lifshitz approach couple with MC description of lattice; **(Mann, Zawodzinski).**

Synopsis:

A model of a composite electrode was developed starting from a description of individual components and their interactions and building to a 3-D composite electrode.

Detailed Report:

Theoretical:

The theoretical model developed as a tool to the understanding and design of the structure and dynamics of the Pt – carbon system is based on a Poisson process for adsorption and desorption that Mann *et al.* developed some time ago. The model features a statement of the conditional probability for adsorption and the inclusion of a conditioning event in the desorption process. The conditioning event is represented by the neighborhood pattern of the chosen particle. The pattern was converted into energy differences through the DLVO model of particle interaction. The focus was on the Van der Waals forces that obtain for this system. Code for what amounts to a Monte Carlo algorithm was written debugged and applied to the adsorption of Pt nanoparticles on spherical carbon support particles. An example of the simulation is shown in Fig 1. The next step is the refinement of the model to include reactions at the Pt nanoparticle surface using the information produced by the molecular theory group. A modification of the algorithm will allow us to study the aggregation of the decorated carbon particles as shown in Fig. 1.

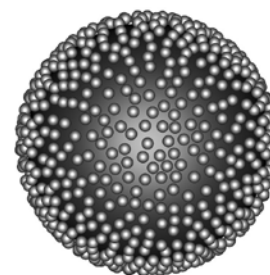


Fig. 1 Stochastic model of Pt nanoparticles decorating a Carbon particles.

Experimental Target 1: Anode

Neurock and Wieckowski combined study of methanol

Synopsis:

A joint theory-experimental study of the methanol oxidation pathway was developed, with experimental studies tailored to address questions or validate aspects of the theory.

Detailed Report:

D. Cao and G. Q. Lu (UIUC); S. Wasileski and M. Neurock (UVA); N. Marzari (MIT), A. Anderson (CWRU); A. Wieckowski (UIUC)

(1) Intensive experiment/theory dialog was initiated to address the key methanol DMFC and EC-NMR theory issues. Experimentally, Dr. Cao completed the project on the decomposition pathways of methanol on low index Pt(hkl) single crystal electrodes. Data were shared with S. Wasileski and M. Neurock (UVA) and the experimental part of the joint paper is being written at UIUC. The “dual path” may be the most elementary set of surface reactions that can be approached by high level theory that may yield satisfactory agreement with experiment. The success of this project will answer the question what is the predictive power of theory (in this specific and important case), and will set stage for more advanced catalyst modeling and related theoretical design of new materials for fuel cells.

(2) The reactivity of Pt/Ru bimetallic surfaces as catalysts for methanol oxidation is critically dependent on the presence of edges of ruthenium nanoislands on platinum on both model single crystal and nanoparticle surfaces. On such surfaces, the steady-state oxidation of methanol occurs at acceptable (for fuel cells) potentials only if surface CO is catalytically removed as CO₂ at the Ru edge. However, the CO stripping from ruthenium on platinum occurs with the lower overpotential than at the ruthenium edge (Lu et al. at UIUC) leading to questions: (i) Is the edge less reactive than the Ru nanoisland interior or weakening of the CO bond on Pt sites neighboring Ru results in reduced “uphill diffusion” rate of CO to Ru/Pt sites. (ii) What can be done to regain the reactivity lost at the Pt/Ru edge vs. that found on the Ru interior. (iii) How to extrapolate this work to theoretical prediction of new catalytic

bimetallic/ternary fuel cell materials. These issues are dealt with M. Neurock and N. Marzari and collaborators.

Periodic density functional theory (DFT) calculations have been used to investigate the elementary C-H and O-H cleavage steps of methanol dehydrogenation over Pt(111) surfaces. The influence of aqueous solvent as well as electrochemical potential has been systematically analyzed. Results show that hydrogen bonding with nearby H₂O solvent molecules influences the stability of surface-bound CH_xO intermediates and the ability to form protons. In addition, a method has been developed to measure and tune the surface potential within the periodic DFT calculations. At potentials relevant for fuel cell applications, two pathways are found: the first proceeds with C–H cleavage to form hydroxymethyl (CH₂OH*), which further decomposes to form CO; and the second proceeds with O–H cleavage to form methoxy (CH₃O*), which can go on to form formaldehyde (CH₂O). These results are consistent with the experimental studies by Iwasita¹ which suggest that formaldehyde is formed via the methoxy intermediate and with experimental results from MURI-funded research by Andrzej Wieckowski, which give evidence for the onset of a dual CH₃OH dehydrogenation path over Pt(111) toward higher potentials.

Anderson; Electrooxidation of CO(ads) on Pt in base is being studied in an interaction with Andrzej Wieckowski to find the mechanism, which appears from experimental investigation to be E-R. Using a local reaction center model, Pt-COOH⋯(H₂O⋯H₂O)₃ + e⁻(U⁰) ↔ Pt-CO⋯OH⋯(H₂O⋯H₂O)₃, it has been found that OH⁻ will bond to CO(ads), forming Pt-COOH⁻ which is ionized in the right potential range to form the Pt-COOH intermediate. *This supports the assignment of the E-R mechanism for the first step.*

Experimental Target 2: combined predictive NMR on metals

Marzari and Wieckowski

Synopsis:

A theoretical framework for rigorous understanding of shifts in the metal NMR spectra in the electrochemical environment was developed.

Detailed Report:

Work on EC-NMR is carried out with N. Marzari (involving Mayeul d'Avezac, a student working on NMR theory from Mauri's group). Due to a considerable drop in the $5d$ -like local density of states at the Fermi level, (E_F -LDOS), between the bulk (at 1.138 G/kHz) and the surface (at 1.10 G/kHz) in a Pt nanoparticle, the surface Pt atoms have higher resonance frequencies from those in the bulk. It is unknown however, which type of Fermi level electrons, d or s , relax the ^{195}Pt spins in Pt nanoparticles. This is being considered both experimentally and theoretically.

***Ab Initio* Theory of Nuclear Magnetic Resonance Shifts in Metals**

Mayeul d'Avezac (Laboratoire de Mineralogie-Cristallographie de Paris)

Nicola Marzari (Department of Materials Science and Engineering, MIT)

Francesco Mauri (Laboratoire de Mineralogie-Cristallographie de Paris)

A comprehensive approach for the first-principles determination of all-electron NMR shifts in metallic systems is presented. Our formulation is based on a combination of density-functional perturbation theory and all-electron wavefunction reconstruction, starting from periodic-boundary calculations in the pseudopotential approximation. The orbital contribution to the NMR shift (the chemical shift) is obtained by combining the gauge-including projector augmented-wave approach (GIPAW), originally developed for the case of insulators (C.J. Pickard, Francesco Mauri, Phys. Rev. B, 63, 245101(2001)), with the extension of linear-response theory to the case of metallic systems (S. de Gironcoli, Phys. Rev. B, 51, 6773 (1995)). The spin contribution (the Knight shift) is obtained as a response to a

finite uniform magnetic field, and through reconstructing the hyperfine interaction between the electron-spin density and the nuclear spins with the projector augmented-wave method (PAW, C. G. Van de Walle, P. E. Blochl, Phys. Rev. B, 47, 4244(1993)). Our method is validated with applications to the case of the homogeneous electron gas and of simple metals.

Experimental Target 3: Cathode ORR

Anderson, Neurock, Mukerjee

Synopsis:

Theory and experiment was also combined in descriptions of cathode processes for the oxygen reduction process.

Detailed Report:

Problem:

What limits the decrease in overpotential for O_2 reduction in those cases where evidently no blocking $OH(ads)$ are forming on the electrode surface?

Solution:

Adsorbed H_2O bonds strongly to the surface at high electrode potentials and blocks O_2 adsorption even when the H_2O has not been oxidized to form the strongly adsorbed $OH(ads)$ poison.

Approach:

A combination of:

- (i) predictions of shifts in reversible potentials for $OH(ads)$ formation on Pt skins on Pt alloys relative to pure Pt (Anderson approach);
- (ii) predictions of shifts in adsorption energies with electrode potential for O_2 and H_2O on pure Pt (Neurock approach);
- (iii) measurements of water oxidation and O_2 reduction currents on Pt and Pt alloy electrocatalysts under conditions of high and low H_2O activity (Mukerjee approach).

Background, Results, and Discussion:

It has been well established in the past dozen years that when first transition series metals are combined with platinum to form alloys, generally compositions PtM_3 have been studied, there is a 50 mV – 60 mV reduction in overpotential at moderate current densities for the four-electron of O_2 to H_2O . Evidence has been accumulating from EXAFS studies of the Northeastern University (NEU) group and high resolution transmission electron microscopy (HR-TEM), Auger, and low energy ion scattering (LEIS) of the Lawrence Berkeley laboratory (LBL) group that indicates the alloy electrocatalysts, whether carbon-supported nanoparticles or polycrystalline films, have ~ 1 monolayer Pt skins on their surfaces. Cyclic voltammograms showed positive shifts in the onset of electrode surface oxidation on the skins relative to the pure Pt electrodes and this indicated that $\text{OH}(\text{ads})$, the first product on water oxidation, which bonds strongly to the electrode surface, formed only at higher potentials on the skins and left the surface Pt atoms available for adsorption of O_2 and its subsequent reduction to water. The O_2 reduction overpotential seemed well correlated with the formation of $\text{OH}(\text{ads})$.

The Case western Reserve University (CASE) quantum theory group used its approach relating the adsorption bond strengths of reaction intermediates to the reversible potentials for their formation and predicted a reduction of 110 mV for $\text{OH}(\text{ads})$ formation on the monolayer Pt skin on Pt_3Cr . This was qualitatively consistent with the observed decrease in the O_2 reduction overpotential for this electrode. The CASE group went on to consider Pt_3Co in a joint study with the NEU group and obtained essentially the same results, a calculated 80 mV increase in potential for $\text{OH}(\text{ads})$ formation. This compared well with the Tafel plot shown in Fig. 1 and the voltammograms in Fig 2.

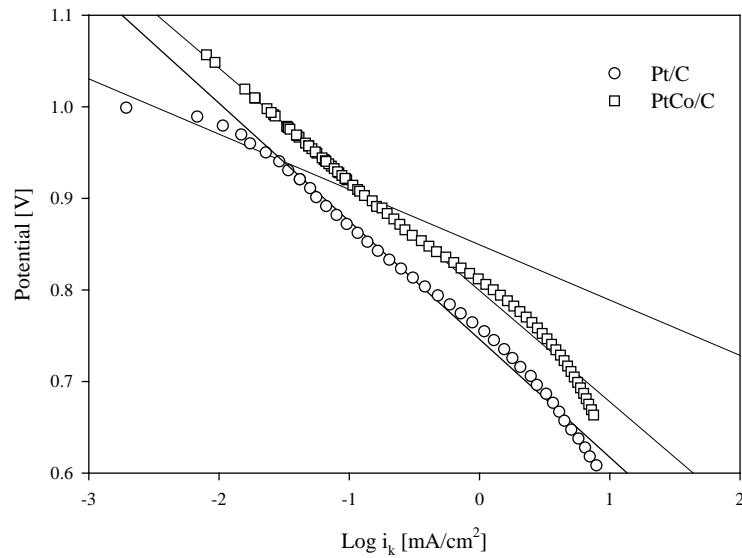


Fig. 1. Tafel plots for carbon supported Pt and Pt₃Co nanoparticles in 1M TFMSA.

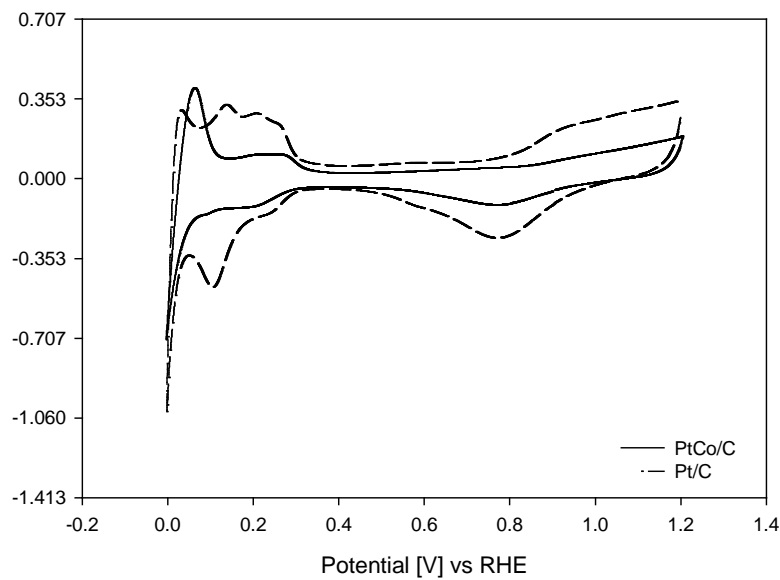


Fig 2. Voltammograms (50 mV/s) for carbon supported Pt and Pt₃Co nanoparticles.

The CASE group considered Pt skins on Pt/Co alloys of other compositions and found that with increasing Co concentration OH(ads) formed on the Pt skin at higher

and higher potentials. Figure 3 shows the slab models used for pure Pt, and Pt skins on Pt_3Co , PtCo , PtCo_3 , and Co in VASP band calculations.

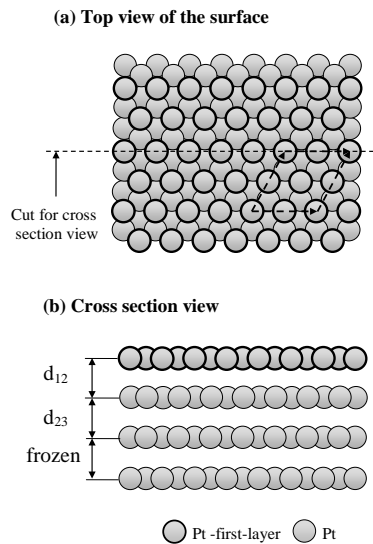


Fig. 3

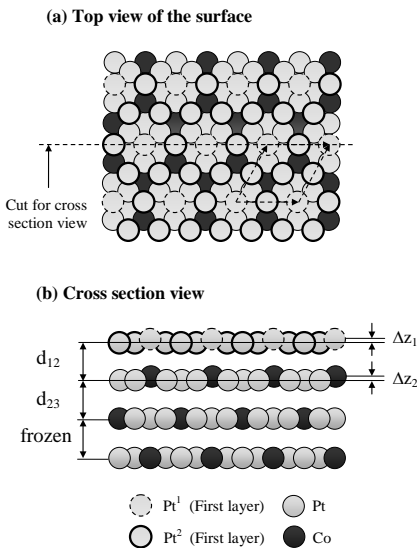


Fig. 4

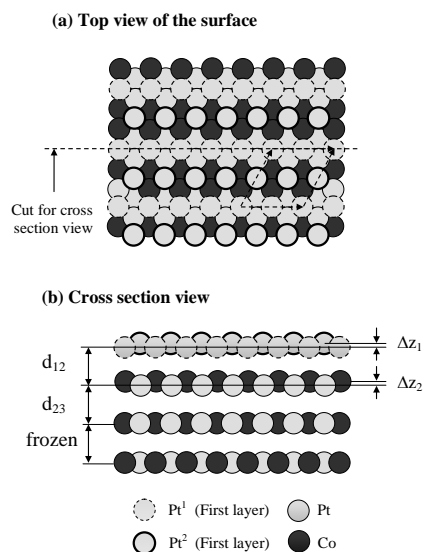


Fig. 5

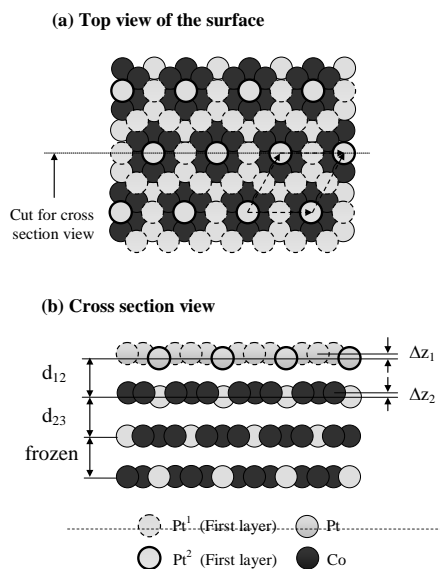


Fig. 6

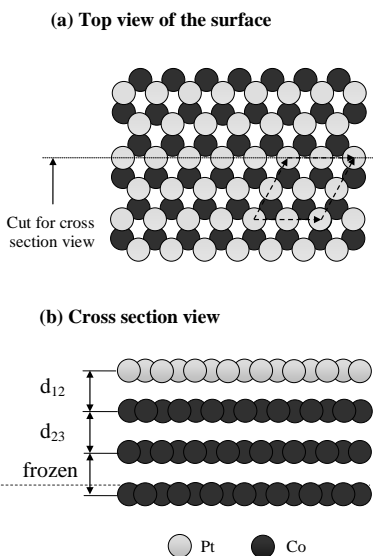


Fig. 7

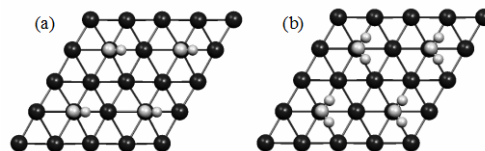


Fig. 8

Figure 3-8 above. Models and parameters for skins on alloys used in ¼ ML H₂O and OH adsorption studies.

Resulting shifts in OH(ads) formation potentials are in Table 1.

Table 1. Shift of the reversible potential, ΔU (V), of OH_{ads} formation from H₂O_{ads} on Pt skin on three layers of Pt₃Co(111), PtCo(111), Co₃Pt(111) and Co(001) at ¼ ML coverage, relative to the Pt(111) four-layer model.

Catalyst	Fig.	Cobalt concentration in the 2/3/4/ layers	U (V)*	ΔU (V) relative to Pt(111)
Pt(111)	3	0 %	0.67	
Pt skin on Pt ₃ Co(111)	4	25 %	0.75	0.08
Pt skin on PtCo(111)	5	50 %	0.85	0.18
Pt skin on Co ₃ Pt(111)	6	75 %	0.94	0.27
Pt skin on Co(001)	7	100 %	0.92	0.25

The NUE group showed that upon decreasing the water activity by going to 6 M TFMSA OH(ads) formation was retarded on pure Pt nanoparticles as shown in Fig. 9.

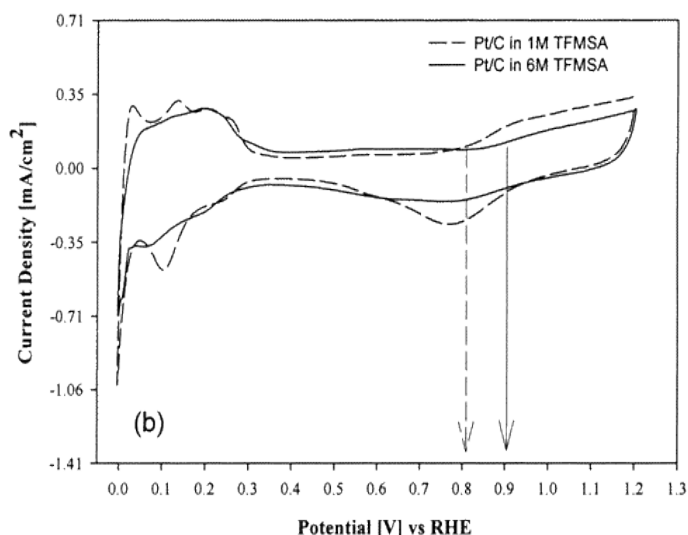


Fig. 9. Cyclic voltammograms for a 20% Pt/C in oxygen-free 1 M (---) and 6 M (-) $\text{CF}_3\text{SO}_3\text{H}$ at room temperature at 50 mV/s vs RHE1 and RHE6 reference electrodes, respectively. Current densities based on geometric electrode area.

The formation of $\text{OH}(\text{ads})$ is clearly suppressed. Relatively more water molecules are tied up in solvating the protons and anions in the 6 M solutions and this contributes to the low activity and inability of the electrode to oxidize H_2O . As shown in Fig. 10 there is a small reduction in overpotential for O_2 reduction in the 6 M acid, much smaller than the 80 mV overpotential reduction over Pt_3Co in 1 M acid as mentioned above. The

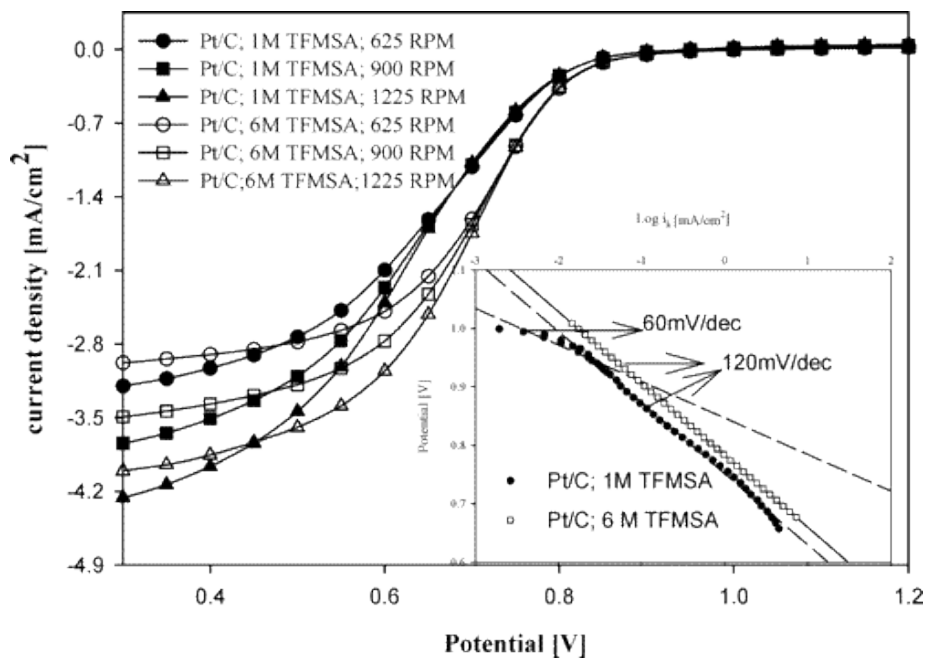


Fig. 10. Disk currents obtained on the 20% Pt/C during ORR in the cathodic sweep at room temperature in 1 and 6 M $\text{CF}_3\text{SO}_3\text{H}$ at various rotation rates (625, 900, and 1225 rpm). Inset shows the Tafel plots for ORR at room temperature at 1225 rpm based on cathodic sweep from 1.2 V to 0.3 V at 25 mV/s in 1 and 6 M $\text{CF}_3\text{SO}_3\text{H}$.

smallness of the reduction in overpotential is probably due to H_2O blocking the catalyst surface against O_2 adsorption beginning in the 0.8 V – 0.9 V range. Note that O_2 reduction has never been observed at smaller overpotentials on any Pt alloys despite the above prediction of even higher potentials for $\text{OH}(\text{ads})$ formation on Pt alloys of higher Co concentration.

The University of Virginia (UV) group has undertaken an electrode potential dependent VASP slab band study of O_2 and H_2O adsorption to find out if in fact O_2 is expected to displace $\text{H}_2\text{O}(\text{ads})$ as the electrode potential is increased. The CASE group showed in 1981, using a semiempirical cluster band shift molecular orbital technique that H_2O and OH bond increasingly more strongly to an iron electrode as the potential is increased. This was due to increased O lone-pair donation to the surface metal atoms as the band was stabilized. However, the present CASE model, though employing modern self-consistent quantum calculation methods, does not include the effects of surface charging. Modern self-consistent density functional calculations, including surface charging, are expected to produce similar trends for Pt electrodes and with excellent accuracy. The trend for O_2 was not studied with the semiempirical theory and could go either way depending the relative π and 5σ donation mixing and back-donation to the π^* orbitals, all of which will depend on potential.

The UV group adds various charges to the slab models of the metal electrode and compensates them with a diffuse homogeneous background charge. The electrode potential is determined by finding the average potential difference between the slab surface and the midpoint between the slabs and adding this to the thermodynamic

workfunction of the standard hydrogen electrode. They find a rapid increase in H_2O adsorption bond strength with increasing potential and a slower increase in the O_2 adsorption bond strength.

There is potentially another aspect of this that may need to be studied, and that is specific anion adsorption on the positive surface for 6 MTFMSA. If water does not displace oxygen, the (partially) solvated anions might. In more typically studied cases of 0.1M or 1 M acid on Pt skins, where the $\text{OH}(\text{ads})$ formation potential is shifted to 0.9 V or so, water will displace oxygen, and this is what has been directly modeled in this theoretical work.

Experimental Target 4 and 6: EXAFS, XANES to reveal electrode structure

Synopsis:

New methods using synchrotron spectroscopy were developed to probe adsorbates on nanoparticles under reaction conditions.

Detailed Report:

Northeastern University research team's focus in the first year has been to develop further our capabilities in using in situ synchrotron spectroscopy for enabling site specific adsorption information on electrocatalysts nanoparticles. This is complemented by our efforts in both tailored nanoparticle synthesis as well as the use of an experimental design involving varying concentrations of TFMSA (Trifluoromethanesulfonic acid) to probe the influence of water activation (water activation: $x\text{H}_2\text{O} + \text{Pt}^*(\text{M}) \rightarrow (\text{M})\text{Pt}-[\text{OH}]_x + x\text{H}^+ + x\text{e}^-$) on Pt and binary Pt alloys for both oxygen reduction and anodic CO tolerance and methanol oxidation. Results of these efforts are enumerated below:

(1) Recently, it has been shown that the Pt-adsorbate scattering, visible in the near edge XANES region, is very sensitive to the adsorbate site symmetry. Using a novel analysis technique that allows isolation of this Pt-adsorbate scattering, combined with theoretical calculations, allows for the *in situ* determination of adsorption sites on electrocatalysts nanoparticles (such as on platinum electrodes utilizing Pt $L_{2,3}$ X-ray Absorption Near Edge Structure, XANES).ⁱ This XANES data can be interpreted with full multiple scattering theoretical results and a comparison of theory with experimental data allow unique spectral signatures to be determined for CO, H, OH, and O in atop, bridged, and/or 3-fold fcc absorption sites. In this work, XANES analysis of the Pt L_3 edge data for Pt-M alloy materials (M=Co, Cr, Ni, Fe) has been accomplished for electrodes in HClO_4 .

(2) The scope of our efforts in oxygen reduction reaction on Pt and Pt alloy electrocatalysts is to (a) Compare the inherent activity for ORR on supported Pt and Pt alloy nanoparticles without the effect of oxide formation via activation of water, this was enabled at higher concentrations of TFMSA (6 M), (b) Examine the relative formation of peroxides via a parallel pathway for Pt and Pt alloy electrocatalysts in 1

and 6 M TFMSA, (c) To examine the site specific adsorption of OH and (d) Understand the surface morphology of Pt alloys under a working electrochemical environment using *in-situ* XAS.

Our results confirm that for Pt/C in a poorly hydrated system (6 M TFMSA concentration), the shift in the formation and extent of water activation on the Pt alloy surfaces can be correlated with *in-situ* XAS data using a novel analysis technique as well as via direct EXAFS probe of formation of oxygenated species above 0.75 V (typical potential for initiation of surface oxides on Pt). Our results on the measured activation energies on a number of Pt alloys in TFMSA has been correlated with calculated values from Professor Anderson's group and a remarkable match was found. In addition his calculations have shown correlations with spectroscopic data showing a lowering of oxide formation in Pt alloys as compared to Pt nanoparticles.

Further our studies using varying concentrations of TFMSA have shown that affinity of molecular oxygen adsorption to Pt sites is affected by changes in the electronic states brought about by alloying. This is reported in a joint paper between us and Professor Anderson's theoretical group.

In addition we have found that the formation of peroxides at the interface is also dependent on presence of water; hence controlling the water activity at the interface provides with important insight on the role of the electrocatalyst surface properties (electronic and short range character) and its relation to the extent of two electron peroxide formation. The enhancement of ORR activity for Pt/C under low water content was shown to agree well with the lowering of oxide formation.ⁱⁱ

Finally the EXAFS data on Pt and Pt-M allows us to examine the surface morphology of the alloy clusters. Based on their co-ordination with Pt it suggests that the various (Co, Ni, Cr, Fe) alloying metal atoms are either at the surface or in the core. This supports the conjecture that the enhancement on Pt-M (M=Co, Ni) alloys occurs via a lateral interaction mechanism between the alloying metal and adsorbate species. However, EXAFS data also confirms that this mechanism is not universal to all alloys and that it is dependant on the cluster morphology. In alloys where the alloying

metal is in the core (Cr, Fe) with a Pt skin, an electronic effect dominates over the lateral interaction. *Pt Skin Formation and Self Segregation*

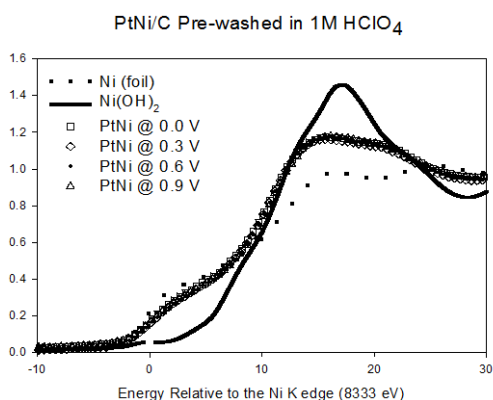


Fig. 3 (a)

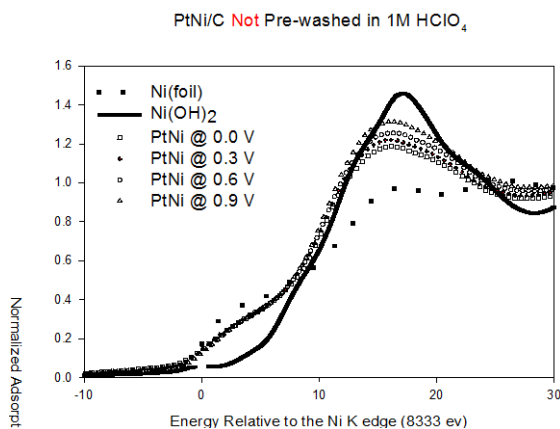


Fig.3 (b)

Evidence of Pt skin formation can be gauged from the comparison of two XANES spectra (Figure 3) at the Ni K edge for a PtNi/C (20% on C) electrocatalysts measured in situ in 1 M HClO₄ as a function of potential. β -Ni(OH)₂ spectra is added as a reference. Figure 3 (a) shows the comparison of the spectra for a catalyst sample washed for 24 hours in 1 M HClO₄ prior to electrode preparation and incorporation into the cell, while the corresponding figure 3 (b) is a comparison of a sample which was not subject to pre-acid treatment. Comparison of the two figures indicate that the latter has significant Ni species on the surface which exhibits the expected oxide growth as a function of potential (seen from the increase in the intensity of the XANES spectra). The former however is largely unaffected, a situation possible only if the Ni was subsurface in the core of the alloy with the surface of the washed catalyst rendered largely Pt rich. Pt skin formation and its effect on the surface electronic states is an important matter for the future design of low Pt loading electrocatalysts and has been examined thoroughly using these experimental evidence, a combination of such *in situ* XAS data as well as electrochemical activity determinations with theory. This paper is recently published in the *Journal of the Electrochemical Society*³⁵.

Experimental Target 5: Vibrational and SFB Methods

Synopsis:

New methods based on sum-frequency generation spectroscopy were deployed for the study of interfacial adsorbates in situ in an electrochemical cell.

Detailed Report:

Since new experimental tools need to be developed to match growing data expectations by theorists, **Wieckowski** has co-developed electrochemical broadband sum frequency generation spectroscopy (BB-SFG) as the next generation method for coherent vibrational surface analysis. (The development began via local funding and the MURI-ARO, DAAD19-03-1-0169 grant, but is now fully MURI-ARO supported via this grant.) The development involved the **Wieckowski** UIUC faculty colleague, Prof. D. D. Dlott [7].) The use of BB-SFG has the potential to trigger new discoveries for optimized fuels and catalysts to closely approximate thermodynamically allowable conversion rates and cell voltages for fuel cells. Dlott's laboratory had developed a femtosecond IR laser system for studies of time-resolved material dynamics that used the broadband multiplex [8,9] vibrational sum-frequency generation spectroscopy (SFG) technique. Owing to the method high spectral sensitivity and reduced IR beam attenuations, Wieckowski developed electrochemical cells where the gap filled by the electrolyte film is controlled by a spacer of thickness of at least 25 μm or more [7,8]. The importance of a thicker electrolyte layer cannot be overemphasized. Thinner electrolyte layers used in the FTIR research can significantly distort the electrochemistry and have led to major errors of interpretation. Too-thin layers also preclude studies of fast kinetics commensurate with fuel cell reaction rates necessary in the fuel cell catalysis work. The broadband multiplex technique is termed **second-generation SFG**, and the Wieckowski-Dlott collaboration is the first to apply this method to fuel cell catalysis, electrochemistry and electrochemical surface science. The authors obtained better SFG spectra in much less time. This is more than a speed advantage; it is a quantum leap in technology.

The current discovery relates to intriguing effects in CO saturated media showing that there is an abrupt jump in the SFG signal amplitude in a certain potential range (that is a function of CO concentration in solution) followed by a plateau [10]. This abrupt jump in signal intensity signifies a phase transition of the CO adlattice [11] from a (2x2)-3CO lattice at lower potential to a $(\sqrt{19} \times \sqrt{19})R23.4^\circ$ -13CO lattice at higher potentials. Recent surface x-ray scattering experiments [12] show surface structures supporting this assignment, so we interpret our amplitude jump data in these terms.

However, even more importantly, the authors proved that BB-SFG is a perfect tool to study catalytic decomposition reactions of fuel cell molecules such as methanol and formic acid. With the second-generation BB-SFG apparatus, methanol and formic acid electrochemical adsorption/decomposition kinetics were measured in acidic media. A polycrystalline Pt electrode and the 0.1 M H₂SO₄ electrolyte containing 0.1M methanol were used and **Wieckowski & Dlott** demonstrated the potential-dependent properties of the CO adsorbate that results from methanol and formic acid decomposition. For methanol, the amplitude (CO coverage) increases quickly initially (Fig. 1-B) and then slows down, reaches a maximum around 0.3 V, then decreases and disappears at around 0.5 V. As the potential scans back, CO reappears at around 0.47 V and reaches max at around 0 V. The frequency reflects the CO coverage effect plus the stark tuning effect (Fig. 1). The width curves are almost the inversion of those amplitude curves. For kinetic studies, we held the potential at

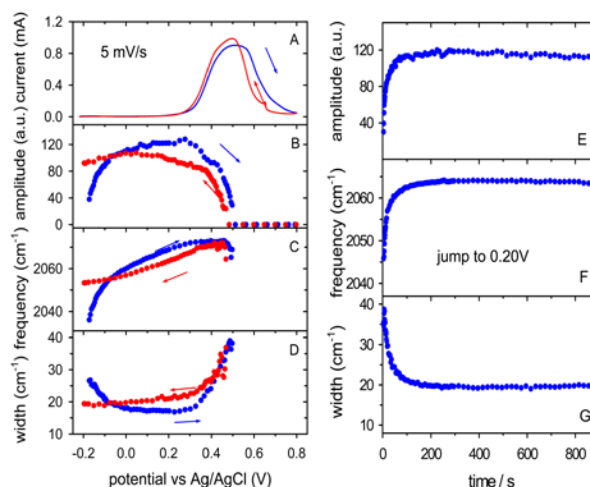


Fig. 1. Electrochemistry and kinetics of CO resulting from methanol decomposition on polycrystalline Pt with acidic electrolyte and 0.1M methanol. A-D Current, SFG amplitude, frequency and width of adsorbed CO, scanning the potential in both directions as indicated. E-G. Starting at 0.75V where the adsorbed CO is rapidly electrooxidized, the potential is then jumped to 0.2V. The formation of the CO layer due to methanol decomposition occurs in about 20s. The adsorbed CO molecules are redshifted and have a broader spectrum at shorter times when the adlayer coverage is low.

0.75 V where CO is removed quickly while the bulk methanol oxidation activity is low (less depletion of methanol in the 25 μm gap). As CO is deposited on the bare electrode and the coverage rises, the CO frequency blueshifts as a result of interactions among adsorbed molecules. The FWHM narrows on the same 20s time scale, it behaves the opposite way comparing to the amplitude and frequency, but all are consistent.

For formic acid, joint analyses by the BB-SFG and electroanalytical fast voltammetry and chronoamperometry techniques were carried out. Consistent behaviors between the two approaches were observed, addressing the issues of formic acid reactivity and poisoning (the dual or even the triple formic acid paths). Intensive email exchange with **Matt Neurock** has developed to connect the theoretical and experimental data on this molecule and its catalytic decomposition pathways. (First ever observation of acetic acid adsorption, a product of ethanol oxidation was also made and was reported at the MURI meeting at Cleveland.) The data obtained by BB-SFG will be used by practical **all MURI team members** and more support for the second generation SFG use will be sought from ARO for expanding the science base of fuel cell catalysis on model and practical fuel cell catalytic systems.

Vibrational recognition of adsorption sites for CO adsorbed on transition-metal surfaces

Ismaila Dabo (Department of Materials Science and Engineering, Massachusetts Institute of Technology, Cambridge, MA 02139)

Andrzej Wieckowski (Department of Chemistry, University of Illinois at Urbana-Champaign, Urbana, IL 61801)

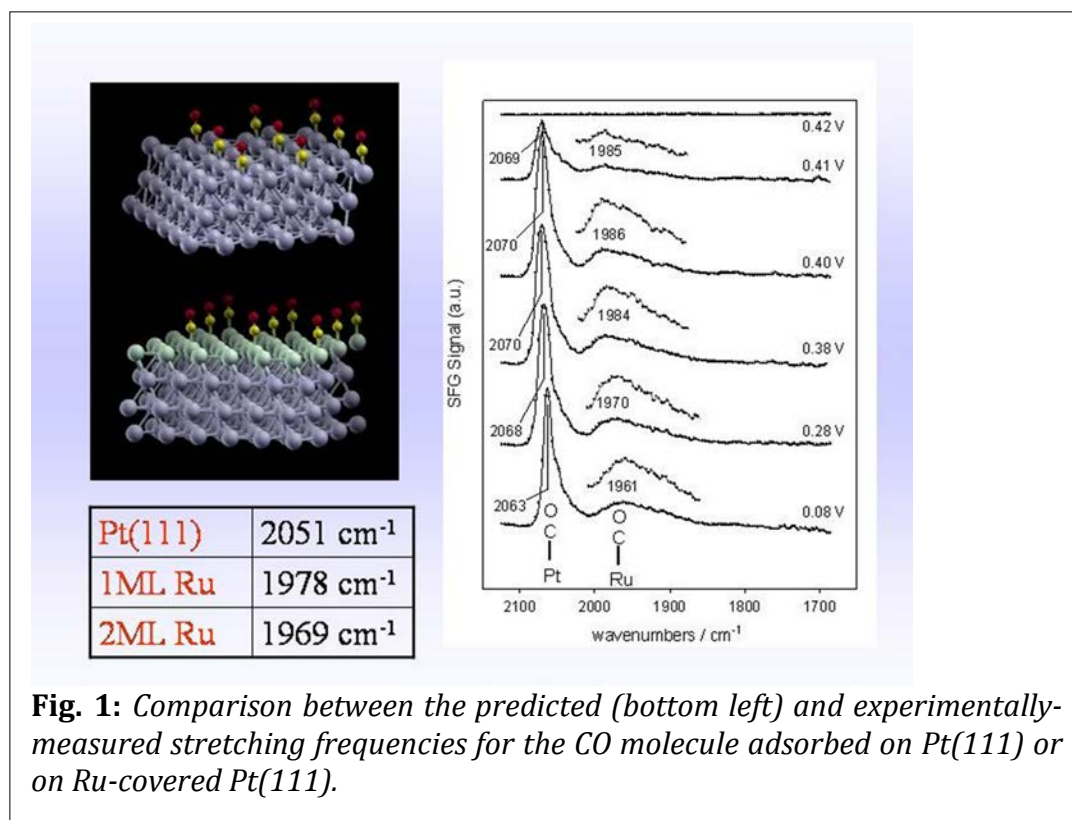
Nicola Marzari (Department of Materials Science and Engineering, Massachusetts Institute of Technology, Cambridge, MA 02139)

Understanding CO interaction with transition metals is fundamental to the design of poison-tolerant fuel cells. Predicting the thermal population of adsorption sites for CO on platinum is however unexpectedly problematic: state-of-the-art energy calculations do not yield the experimentally-observed site preference. Despite this fact, an excellent quantitative determination of the vibrational properties can be achieved by density-functional perturbation theory, allowing the vibrational recognition of CO adsorption sites on platinum and platinum-ruthenium surfaces.

The adsorption energies and structural properties of CO adsorbed on platinum and platinum-ruthenium surfaces have been calculated by density-functional methods. The vibrational properties have been studied within density-functional perturbation theory. To determine the most stable adsorption site, the theoretical vibrational frequencies have been compared to the experimental spectra obtained by Prof. Wieckowski's group.

To investigate the effects of orbital hybridizations on the C-O stretching frequency, we have developed a novel orbital-resolved force approach. We have employed a “GGA + molecular U” exchange-correlation functional to vary the amount of electron transfer between the adsorbate and the substrate, in order to rationalize the accuracy of density-functional theory in predicting vibrational spectra while failing in determining the correct adsorption energy sequence.

(1) Despite major qualitative energy errors, density-functional perturbation theory yields accurate vibrational frequencies for CO adsorbed on platinum and platinum-ruthenium surfaces.



(2) Contrary to the adsorption energies, an overhybridization of the lowest unoccupied molecular orbital has little direct bearing on the C-O stretching frequencies. The frequency shifts are indeed primarily related to the hybridization of the occupied 1- π CO orbital. This fact rationalizes the accuracy of density-functional stretching frequencies in spite of the low reliability of the calculated adsorption energies.

Experimental Target 6: Delta-u method

Synopsis:

This is largely covered in Target 4 above.

Experimental Target 7: Non-precious metal materials

Synopsis:

Several classes of metal-based non-Pt catalysts were studied in combined experimental and theoretical efforts. Laccase (Cu centers), Ru-Se and Rh-chalcogenide compounds were studied.

Detailed Report:

Anderson: An extensive model study of O₂ reduction over supported copper laccase has been completed. A mechanism has been found for the 3 Cu^I site wherein O₂ can coordinate, become reduced to OOH, and dissociate with small barrier to HO-Cu^{II} and Cu^{II}-O-Cu^{II} so that *the reversible potential, U^0 , for this step is 1.86 V. Subsequent reduction steps to very weakly held H₂O occur at $U > 1.23$ V. The E_a for the first step is probably rate determining*

Wieckowski Similar experimental database for the theoretical treatment is now available for **ORR** [6-16]. As well known, methanol crossover occurs through the solid electrolyte membrane from the anode to the cathode, where it is oxidized. The simultaneous **ORR** and oxidation of methanol at the cathode leads to additional drop in the cathode potential and hence the decrease in the **DMFC** performance. The development of highly active, methanol tolerant cathode catalysts is one of the most important stumbling blocks preventing design of high-efficiency DMFCs. In response, we have carried out oxygen reduction studies on Ru and Rh nanoparticles modified with selenium and sulfur. Apparently, the most active **ORR** catalysts from those examined is Ru/Se: the cathodic current commences at 0.9 V, and the diffusion limiting current develops at 0.4 V vs. RHE (Figure 2). The activity of **ORR** does not decrease in presence of methanol, showing a complete methanol tolerance. It is proposed below that metallic Ru atoms surrounded by Se are the active sites for **ORR**. For the reasons that are still being investigated, these favorable activity conditions were not fulfilled on smooth Ru surfaces.

We synthesized novel metal-chalcogen catalysts, using commercial Ru or Rh nanoparticles and elemental Se and S. Details of the Ru/Se syntheses are still proprietary pending patent decision on the LANL invention disclosure No. 2005-055/S-104, 947. The critical strategy in the synthesis was that the commercial Ru nanoparticle catalyst was first reduced at ca. 100 C for 1h under hydrogen (UHP) flow using the apparatus reported previously. The same approach was used for the synthesis of Ru/S, Rh/Se and Rh/S nanoparticle chalcogenide materials. To prepare an electrode made of the nanoparticle catalyst for electrochemical (and partially for XPS) measurements, a suspension of a 2.5-mg catalyst and 1-mL water was prepared by sonication for 30 min, 4.2 μL ($\sim 10.5 \mu\text{g}$) of the resulting suspension was placed onto a Au rotating-disk electrode (RDE), and dried in air at room temperature for 2 h. A thin layer of nanoparticles was thus formed on a Au RDE, giving a catalyst loading of approximately $150 \mu\text{g cm}^{-2}$.

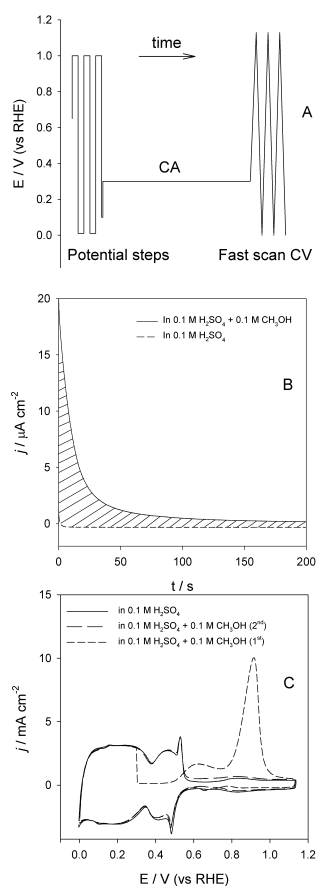


Fig. 1. The combination of chronoamperometry and fast scan cyclic voltammetry: CA/CV. (A) Potential steps for cleaning, (B) Chronoamperometry, (C) Fast scan cyclic voltammetry. After chronoamperometric decay at a methanol decomposition time t , a fast voltammetric scan is taken. The stripping CV charge after t is the measure of the CO amount accumulated after the time t .

The EC NMR data -- after comparing the T_1 results on Ru_xSe_y (the Alonso-Vante cluster-like) and Ru/Se (obtained at UIUC) -- show that Se is in the metallic state in both of these catalysts. Data obtained by XPS provide further details of the Ru/Se catalyst structure. The potential cycling causes Se removal from the Ru surface. XPS spectra of Se 3d show that then that the Se remaining after the potential cycling is significantly oxidized (most likely to SeO_2). The Ru component is also affected; the oxidation of Ru

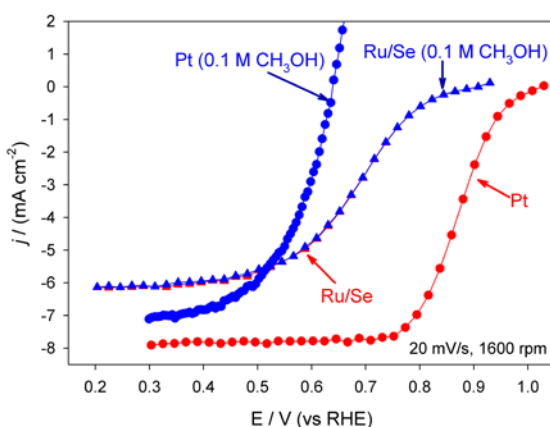


Fig. 2. Ru/Se synthesized at UIUC (Ru/Se, red and blue) is a very promising cathode catalyst for ORR, confirmed on the membrane at LANL.

is represented by the extent of the Ru 3d peak broadening (FWHM). The data show that FWHM is significantly larger when Se is removed, which is indicative of the major change in the nature of the Ru-O bond. When the oxidized Ru/Se sample was compared to the oxidized Ru black sample (in air) the additional O-compound, located at lower BE side on the O 1s spectrum, was detected for Ru but not for Ru/Se (Figure 3). This O-compound can be assigned to the more strongly bonded O on Ru, which cannot be formed when Se is present. This observation, along with the observed significant Ru 3d_{5/2} peak FWHM increase when Se is removed, suggests that Se is modifying the electronic properties of Ru. This overall confirms the Alonso-Vante theory of how the Ru_xSe_y and, apparently, Ru/Se materials work. Namely, that the role of Se is to chemically stabilize the metallic Ru centers against oxidation.

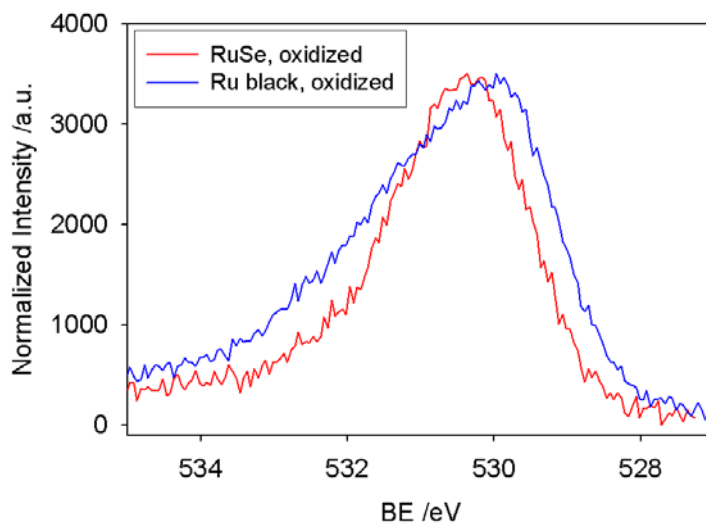


Fig. 3. BE O1s XPS spectra of the Ru/Se sample exposed to air. There is no strongly bonded oxygen formation (red line) when Se is on the surface (expected at lower BE vs. pure Ru, blue line)

In conclusion, we synthesized Ru/Se, Ru/S, Rh/Se, and Rh/S catalysts by the reaction between Ru and Rh nanoparticles with Se and S elements. The **ORR** was performed on the four catalysts with the comparison of Ru and Rh nanoparticle blacks. Among the four synthesized catalysts, a significant increase in activity of Ru/Se was found. On Ru, the sulfur adsorbate also worked as a promoter. On Rh, both Se and S were poisonous towards the **ORR**. All the four catalysts were methanol tolerant. An active site approach was proposed for Ru/Se, which is similar to that previously reported for a Ru_xSe_y cluster catalyst. Further, it shows that Ru on the nanoscale favors the reaction with Se as compared to the flat surface. Due to disorder of the surface atoms, this fact provides evidence that the chemical state is different at the nanoscale vs. in the equivalent Ru/Se bulk material. We confirm that the role of Se in promoting the ORR activity is to chemically stabilize the metallic Ru centers against oxidation.

Mukerjee

Current State of the Art in Chalcogenide based Electrocatalysts

The original work performed in the 1970's and 1980's showed that chalcogenide clusters were indeed active towards ORR, but lacked stability in the

harshly acidic environment of fuel cells.³⁻⁵ In a 1986 communication to *Nature*⁶, Alonso-Vante and Tributsch reported that MoRu-based Chevrel-phase chalcogenides showed significantly high activity towards ORR. Although the initial work was based on an incorrect Chevrel-phase structural model, a growing body of literature attracted attention from other groups.⁷⁻¹³ Based on the limited work done, the best reported ORR chalcogenide electrocatalysts for PEMFC applications can be ranked as follows: MoRuSe > MoRuS > WRuSe > RuSe > RuS > MoSe > MoS, with respect to ORR activity. The exact mechanism of the ORR at these centers is still in dispute, however, although several *in situ* EXAFS studies have been conducted.¹⁴⁻¹⁷

A wealth of work regarding the methanol tolerance of chalcogenide catalysts has generally pointed to pseudo-binary $X_xRu_yS_z$ clusters (where X = Rh, Re, or Mo) as exhibiting the best performance to date.^{10, 18-22} While several clusters are completely nonselective towards methanol, the moiety which gives the best performance is still hotly debated. In general, Alonso-Vante holds to a MoRuS composition²³, Tributsch favors RuSe²¹, and the Hamnett group has published extensively on RhRuS and ReRuS²⁰. The exact role of the catalytic center together with the chalcogen in the depolarized environment of methanol and chloride ions is still unclear. Most of these reports have indicated favorable stabilities of some of the compositions in an acid environment; however there are no systematic studies in this arena. In addition, there is no study to the best of our knowledge on the nature of chloride ion tolerance.

Summarized below is our initial set of data aimed at furthering our attempt to understand more clearly the nature of oxygen reduction at a chalcogenide surface.

Water Activation and Effect on Cathodic Oxygen Reduction at a Polymer Electrolyte Interface:

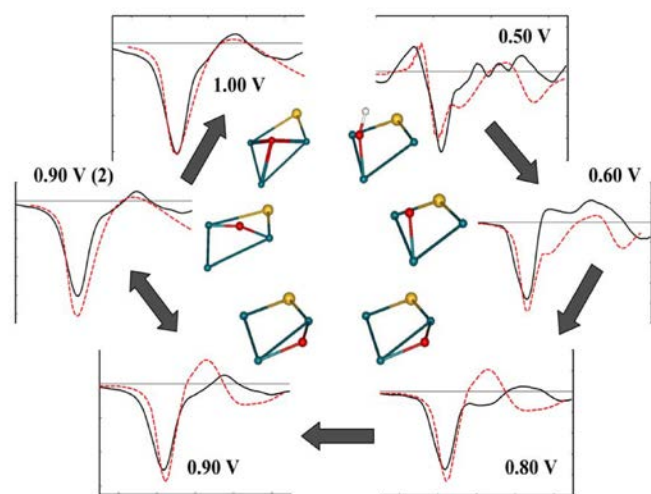


Fig. 1. Theoretical FEFF 8.0 fits (dashed) and experimentally derived (solid) $\Delta\mu$ curves for the 30wt% $\text{Rh}_x\text{S}_y/\text{VXC72}$ (E-TEK) electrocatalyst in 1M TFMSA shown with the corresponding oxygenated models used to generate the fits.

Application of the $\Delta\mu$ XANES technique to *in situ* XAS data collected under real electrochemical conditions coupled with activation energy measurements has allowed, for the first time, the direct observation of the water activation on a heterogeneous 30wt% $\text{Rh}_x\text{S}_y/\text{VXC72}$ (E-TEK) chalcogenide electrocatalyst via the modeling of the Rh_3S_4 phase. As mentioned in the previous years report, the application of this technique is a major

advance over the current state of the art *in situ* XAS technique which is bulk averaged and hence unable to provide the atomic level surface adsorption information currently possible with the $\Delta\mu$ XANES technique (see references ^{2, 24-26} for further information). Not only is a clear delineation between one and n-fold adsorbed O(H) species observable, but the specific site symmetry of adsorption on the catalyst has been clarified. Akin to Pt/C electrocatalysts, the surface of Rh_3S_4 is dominated by 1-fold O(H) species at low potentials (figure 1). Beginning at 0.80 V, a successive parade of 2-fold to n-fold adsorbed O dominates on the surface (figure 1). Similarities to the activation energies for ORR of Pt/C systems non-withstanding, the nearly identical nature of the water activation process is remarkable. The ramifications of this examination are significant. First, the $\Delta\mu$ technique has been previously successfully applied to homogeneous Pt and Pt-alloy electrocatalysts. Compared to a mixed-phase chalcogenide material, however, those prior investigations were considerably easier to perform. Here the $\Delta\mu$ analysis was proven not only to function in a mixed-phase environment, but also supplied the chemical information necessary to discern the active sites for ORR in respect to

potential. Indeed, considering the considerable amount of work performed over the past decades to understand the kinetics of ORR on Pt-based electrocatalysts, the time scale of this investigation on a chalcogenide electrocatalyst is significantly brief. It is anticipated that future examinations on the phases present in the 30wt% Rh_xS_y/VXC72 electrocatalyst will convey similarly detailed information.

Previous work suggests that one can tune one of the three mechanisms to dominate by changing the particle morphology and size. Further, since the bifunctional mechanism and the two different direct mechanisms dominate at different potentials, this data suggest that the particle morphology determines whether a catalyst will be operative optimally in reformat or in methanol, since the anode is generally at lower potential in reformat (when the bifunctional mechanism is operative) and higher potential in methanol when the direct mechanisms are operative. Further work on this will be reported in a forthcoming publication.³³ This work will be used in the simulations of activation energy barriers on the two different mechanistic pathways previously published by Wieckowski and Neurock³⁴

Experimental Target 7: Synthesis of Nanoparticles (Mukerjee, Zawodzinski)

Synopsis:

A variety of efforts were developed for nanoparticle synthesis. Mukerjee propagated these methods throughout the team. In the study reported below, a series of reducing agents was deployed to prepare nanoparticles on carbon fiber supports.

Detailed Report:

The catalyst performance in a fuel cell is also affected by the support used. This is manifested in several ways, ranging from the catalyst activity to the stability of given catalyst sizes to the accessibility of the catalyst in the composite electrode. In another project activity, we explored the preparation of supported Pt on fibrous support materials.

Many different carbon forms, such as activated carbon, carbon black, carbon nanofibers and nanotubes, can be used as support materials for precious metal catalysts used in fuel cell electrodes. We first compare the ability of functionalized high surface area graphitic (carbon nanofibers) and amorphous (activated carbon) carbons to homogeneously support finely divided platinum catalyst particles, then contrast the performance of platinum/carbon composite electrodes within a hydrogen fuel cell. Functionalization by concentrated acid treatment results in the creation of various oxygen carrying functionalities on the otherwise inert carbon surfaces. The degree of surface functionalization is found to be a function of the functionalization treatment strength. Chemical reduction of the platinum precursor complex using milder reducing agents in the temperature range of 75–85°C, and using ethylene glycol at 140°C yields the smallest platinum particle sizes observed in this study, a result confirmed by X-ray diffraction and transmission electron

microscopy measurements. X-ray photoelectron spectroscopy measurements confirm the existence of platinum in primarily its metallic state on the functionalized carbon surfaces.

In another study, the influence of carbon support morphology on the fuel cell performance of its corresponding MEA was investigated. Platinum catalyst supported on fibrous (carbon nanofibers) and particulate carbon (Vulcan® XC-72) supports were employed to prepare supported catalyst inks and membrane electrode assemblies. The level of Nafion binder in the supported catalyst ink was varied and the consequence on polarization behavior of the MEA determined. The trend in polarization behavior was found to be independent of the support morphology, which reaffirmed a key conclusion from one of our previous publications. Upon mixing the two types of supports in various weight concentrations and depositing platinum by the glycol method, key supported catalyst properties such as supported platinum content, size of the platinum catalyst and electrochemically active surface area were found to be very similar. The results indicated that lower surface area supports of various morphologies can be interchangeably employed as catalyst supports in PEM fuel cells.

The electrochemical performance of platinum (Pt) catalyst deposited on various functionalized carbon supports was investigated and compared with that of a commercial catalyst, Pt on Vulcan XC-72 carbon. The supports employed were graphitic or amorphous with a wide range of surface areas. Cyclic voltammetry and Rotating disk electrode studies on the supported catalysts indicated equivalent platinum catalyst activities, especially for the low surface area carbons studied. Fuel

cell performance and electrochemical parameters were determined for Membrane Electrode Assemblies (MEA) fabricated from the supported catalysts. The use of high surface area supports did not necessarily translate into a higher electrochemical utilization of platinum, as was otherwise expected. Electro-impedance spectroscopy (EIS) measurements indicated lower ohmic losses for low surface area carbon MEAs; this was explained by the supported catalyst electrode microstructures and their resistivities. Correlation of the morphology and resistivity data with the electrochemical parameters determined from the fuel cell performance indicated that for low surface carbons, the nature of the support does not significantly affect the Pt catalytic activity (and hence the overall fuel cell performance). Influence of the support is much more critical when higher surface area carbons are used because of the vastly different electrode morphology and resistivity.

Experimental Target 8: HRTEM studies

Synopsis:

A variety of HRTEM and related methods for studies of nanoparticles were deployed for the project. These provided information related to particle size, orientation, strain, alloying and other aspects of structure, including glimpses of distortion induced by particle-support interactions. For quantitative interpretation, the methods required correction for distortions in images to reveal nanoparticles strain effects.

Detailed Report:

Three graduate students supported by this project have been trained in the theoretical background of (HRTEM) high-resolution transmission electron microscopy, operation of the high-resolution microscope Tecnai F30, and HRTEM image simulations by the responsible PI (F. Ernst) and a postdoctoral research associate in his group (K. Du).

First experimental results have been obtained on catalyst particles consisting of (i) pure Pt, (ii) a Pt core nominally coated with a monolayer of Ru, and (iii) a Pt₅₀Ru₅₀ solid solution. The results have generally shown the feasibility of imaging such catalyst particles with atomic resolution. Common features that were observed include a relatively broad size distribution, a clear trend for faceting, and the presence of internal defects, such as stacking faults, which intersect with the surface of the particle and locally change its atomistic structure. Experimental observations of intensity variations of the black and bright spots representing atomic columns in $\langle 110 \rangle$ projected HRTEM images of the alloy clusters (iii) suggests that conclusions can be drawn from HRTEM images about the spatial distribution of Pt and Ru atoms in these clusters. This hypothesis has been further explored and confirmed by HRTEM image simulations of various cluster models.

In the course of these first studies, the following problems were identified:

(i) The clusters tend to agglomerate, which renders them difficult to image under optimum HRTEM conditions.

(ii) The high coherence of the illumination system of the Tecnai F30, which is based on a field-emission gun, causes substantial delocalization of information in the HRTEM image. In order to deal with this problem, exit wave reconstruction from defocus series will be explored and employed in the next phase of the project.

(iii) In order to analyze strain state of the clusters, it will have to be imaged at an extremely high magnification ($\approx 10^7$) in order to obtain a sufficiently high a sampling rate of the image. This requirement interferes with the magnification limit of our instrument.

In the next phase of the project, the adverse effects of delocalization shall be eliminated by exit-wave reconstruction from series of HRTEM images recorded at different defocus settings of the objective lens. An experimental scheme will be devised to overcome the magnification limit and pave the way for analyzing the strain state of the clusters with high accuracy. High-resolution scanning TEM, and particularly Z-contrast imaging, will be explored as alternative method to conventional HRTEM imaging. Provided that corresponding equipment will become available, we three-dimensional information about the catalyst particles will be obtained by electron tomography.

Microcharacterization of Catalyst Particles

M. Pelsozy and F. Ernst

The goal of this part of the project is to obtain detailed information about the atomistic structure of catalyst particles of various compositions and fabricated under various conditions by means of HRTEM (high-resolution transmission electron microscopy). In conjunction with catalytic activity, the most important aspects of the atomistic structure include:

- the size distribution of the particles,
- information about neighbor interactions (e.g. agglomeration, stability of the size distribution),

- typical particle shape (possibly a function of particle size),
- interaction with the globular carbon support (e.g. wetting angle, which determines the surface-to-volume ratio)
- extended defects in the interior (e.g. stacking faults affecting the surface morphology),
- the spatial distribution of solute atoms in alloy clusters (e.g. tendency to form core-shell structures),
- the morphology of the surface (e.g. preferred crystallographic facets, possibly a function of particle size)
- surface defects (e.g. facets, edges, and steps), and
- strain (introduced by the proximity of free surfaces and surface segregation of solute elements).

To investigate these aspects, we have received specimens of cluster particles on globular carbon support from several project partners and prepared them for observation in the high-resolution electron microscope.

HRTEM is the only available experimental technique that can provide the interior atomistic structure and surface structure of individual macroscopic metal particles. The technique is extremely powerful, however it also suffers from a couple of problems. HRTEM inherently produces two-dimensional projections of the object structure. One important problem, therefore, is to prepare specimens in which the catalyst particles can be imaged without any supporting material in the path of the electrons, since this would disturb the image of the particle.

The specimen preparation we have established to maximize the chance of observing catalyst particles situations suitable for HRTEM imaging of the atomistic structure is to deposit the material from its solvent onto a planar, holey carbon support film. Basically, this is an ultra-thin carbon film supported by a somewhat thicker carbon film containing holes (like a Swiss cheese), which in turn is supported by a square

Cu grid. A variety of such support films has been purchased from TEM suppliers, and we have identified films with a suitable density of holes.

While the state-of-the-art instrument we are using provides information about atom spacings as small as 0.14 nm, another inherent problem of HRTEM is that meaningful information can only be obtained from these images when the viewing direction coincides with a load-indexed crystallographic direction in the crystal structure of the particle. While it is theoretically possible to tilt an individual cluster into such a viewing direction, this is not feasible in practice because specimen tilt usually introduces large specimen translations and instability. Moreover, it is hardly possible to determine the exact actual orientation of an individual catalyst particle because in the case of nanoscopic particles the electron diffraction pattern, which is normally employed for orienting crystalline specimens, does neither contain sufficient intensity nor detailed information (Kikuchi lines) about the crystal orientation. Therefore, the only viable method to observe catalyst particles in the viewing direction suitable for HRTEM is to observe a large number of particles and focus on those that are correctly oriented by chance.

Owing to the small size of the particles, fortunately, the tolerance for misorientations is somewhat larger than it is for larger crystals, which increases the chances to find correctly oriented particles. Still, the probability is relatively small and needs to be multiplied by the equally small (or smaller) probabilities of finding a particle sticking out laterally from the globular carbon support *and* the even smaller probability the particle is accidentally hanging over a hole in the holey carbon support film.

As reported earlier, we found that HRTEM images of the catalyst particles (strong electron scatters) suffer from considerable artifacts related to the high degree of temporal and spatial coherence of the electron wave carrying the information about the atomistic structure. In particular, the images suffer from a significant *delocalization* of spatial information: the electrons that arrive at a particular point in

the image are usually not exclusively from the corresponding point of the object but from broad region around the object point. Moreover, an inherent problem of plain HRTEM images is that they only reveal the intensity of the electron wave. The electron wave amplitude, however, is a complex-valued function of two spatial coordinates, while the image intensity is a real-valued function. This means that by just obtaining the image intensity, 50% of the information contained in the electron wave is lost.

For this reason, methods of electron holography have been developed to recover both the amplitude and the phase of the electron wave in the image plane. One particularly powerful method of this arsenal is "exit-wave reconstruction from focus series." The approach is to record a series of HRTEM images at different focus settings of the objective lens. From these data, a reconstruction algorithm implemented on a computer recovers both the amplitude and phase of the electron wave at the exit surface of the specimen, while simultaneously compensating for aberrations (mainly spherical aberration) introduced by the electron optical components of the transmission electron microscope.

In the period covered by this report, we have successfully upgraded our instrument (hardware and software) to provide this capability. First tests of acquiring focus series and processing the data have been performed. While a couple of problems remain to be solved, our overall impression is that the method is viable and particularly powerful for our purpose of studying the atomistic structure of nanoscopic catalyst particles.

In the following, we report experimental results obtained by plane HRTEM and to electron holography by focus-series reconstruction from two different kinds of specimens:

- (i) Pt particles on globular carbon support from E-Tek.
- (ii) Pt particles on globular, high-surface area carbon support prepared by the reverse micellar method from Northeastern University (S. Mukerjee).

Particle Size

For both kinds of specimen, the mean particle diameter, D , and the FCC lattice parameter, a_{FCC} , were determined by XRD (X-Ray diffraction) via measuring the line broadening due to particle size and the 2θ position of the Pt (220) reflection. Table I compiles results we have obtained for the mean lattice parameter and the mean particle size on two specimens of each charge by inserting the results of least-square fits to the data into the Scherrer equation

$$D = \frac{0.9\lambda}{B \cos[\theta]} \quad (1)$$

where λ is the X-ray wavelength, B is the half-width at half-height for the diffraction peak (in radians), and θ is the Bragg angle (half of the diffraction angle). The columns labeled σ_D and σ_a in Table I indicate the standard deviation of the mean particle size and the lattice parameter, respectively. The column labeled $\sigma_a(\%)$

Specimen	D (nm)	σ_D (nm)	a_{FCC} (nm)	σ_a (nm)	σ_a (%)
Pt/C	3.32	0.04506	0.02253	0.3929	2.294E-04
Pt/C	3.32	0.02619	0.01171	0.3927	9.127E-05
Pt-Co/C-1	3.24	0.08246	0.03688	0.3929	1.755E-04
Pt-Co/C-2	3.12	0.07516	0.03361	0.3905	9.934E-05
Pt-Co/C-3	3.61	0.03826	0.01711	0.3894	8.893E-05

indicates the deviation of the mean lattice parameter of the particles from the standard lattice parameter of bulk Pt.

Table I above: Particle size and lattice parameter of catalyst particles.

Plain HRTEM Imaging

Figure 1 shows a HRTEM image of a Pt cluster on a high-surface area carbon support prepared by the reverse micellular method at North Eastern University. The diameter across the widest horizontal dimension of the Pt metal atom cluster is ≈ 3 nm, in good agreement with the mean particle size indicated in Table I. The platinum particle is in the center of the image. In the background behind the platinum particle, a diffuse pattern appears that represents the thin amorphous carbon foil in a "hole" of the holey carbon support film. In the lower half of the image, the image exhibits a pattern of horizontal ripples. This contrast pattern originates from the globular carbon support.

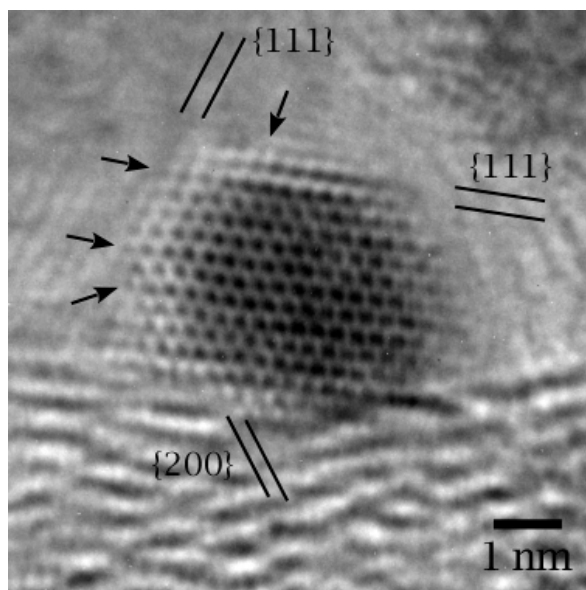


Fig. 1: HRTEM image of a Pt particle (S. Mukerjee, North Eastern University).

The atoms in the platinum particle appear as regular pattern of black dots. The viewing direction corresponds to $\langle 110 \rangle$, exposing two sets of $\{111\}$ planes intersecting at an angle of 71° . In the particle shape approximately corresponds to a sphere, however with a clear preference of $\{111\}$ and $\{200\}$ facets. The facets that are apparent in the present $\langle 110 \rangle$ projection are consistent with the assumption that the idealized shape of the particle corresponds to a "truncated octahedron,"

mainly faceted on {111} planes but truncated by {200} planes at the tips, where otherwise the surface-to-volume ratio would be unfavorably high.

At the high magnification of $\approx 10,000,000$ times of this image, the surface of the globular carbon support (bottom half) appears practically straight. It partly projects over (or under) the bottom of the pattern representing the atomistic structure of the particle. The orientation of the line that marks the surface of the carbon support in this projection corresponds to the orientation of a {111} plane in the platinum particle. This observation suggests an attractive interaction between the platinum and the carbon support, striving to maximize the contact area while maintaining the ideal shape of a truncated octahedron.

In addition to the facets, Fig. 1 shows monatomic steps oriented parallel to the viewing direction in the surface of the particle (arrowed). It is likely that these regions, where the interatomic bonding is particularly disturbed, play an important role for the catalytic activity.

As mentioned before, plain HRTEM micrographs usually suffer from substantial artifacts. In Fig. 1, in particular, the periphery of the particle exhibits a bright "Fresnel" fringe, reflecting limitations of the electron optics in transferring high spatial frequencies, that is small spacings and abrupt changes in the projected electrostatic potential, as they occur at the sharp facets of the particle in this projection. Therefore, the information about the mono atomic steps one can gain from this image is not particularly detailed and prone to errors. Moreover, the positions of the black spots in this image will most likely not represent the true positions of the atom columns in the particle because of the abovementioned localization effect: the electrons that form the image of one column actually originate not only from the corresponding column but also from neighboring columns. Therefore, an analysis of the strain in this particle, for example, can only be carried out after deconvolving the image from these effects, e.g. by focus series reconstruction.

The HRTEM images of Figs. 2, 3, and 4 are part of a focus series. Comparing these images is instructive for understanding potential artifacts in HRTEM images and, in particular, the effect of delocalization. In the center of Fig. 2, a platinum particle

sticks out into the specimen hole. The particle is viewed in a $\langle 110 \rangle$ projection, and the atomistic structure is clearly resolved. However, the surface appears blurred. Moreover, a fine pattern of the fringes "leaches" out into the hole. Since the object points that have generated this pattern are certainly not located in the specimen hole, this feature of the image constitutes an artifact of delocalization.

Figures 3 and 4 show the same field of view as Fig. 2, but were recorded at slightly different focus settings of the objective lens. The surface of the particle is imaged in much better quality than in Fig. 2. Similar to Fig. 1, the surface is faceted on $\{111\}$ planes. However, considerable surface roughness is introduced by monoatomic steps (arrowed in Fig. 3) parallel to the $\langle 110 \rangle$ viewing direction.

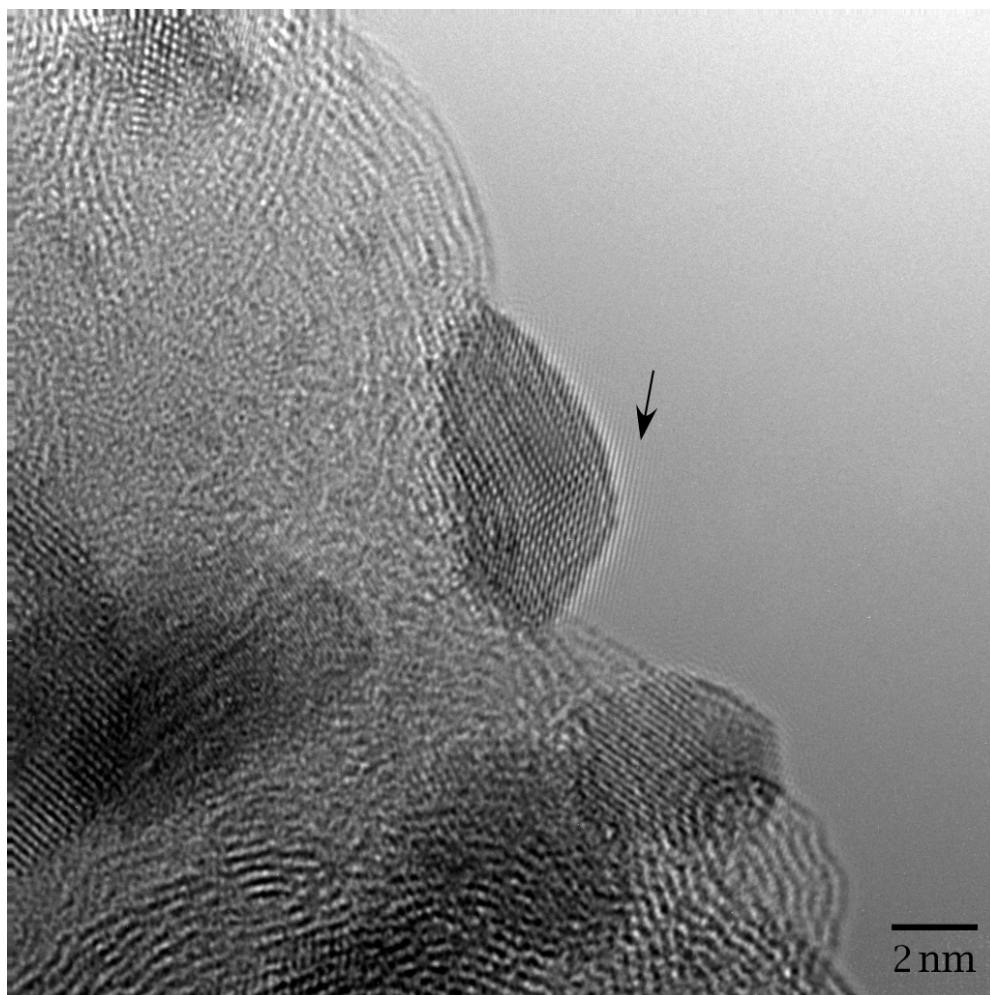


Fig. 2: Atomic resolution image of Pt catalyst particles on globular carbon support (S. Mukerjee, North Eastern Univeristy).. The arrow points at a region in which limitations of the electron optical imaging system cause the appearance of lattice fringes in the hole ("delocalization"). This image is #1 of a focus series.

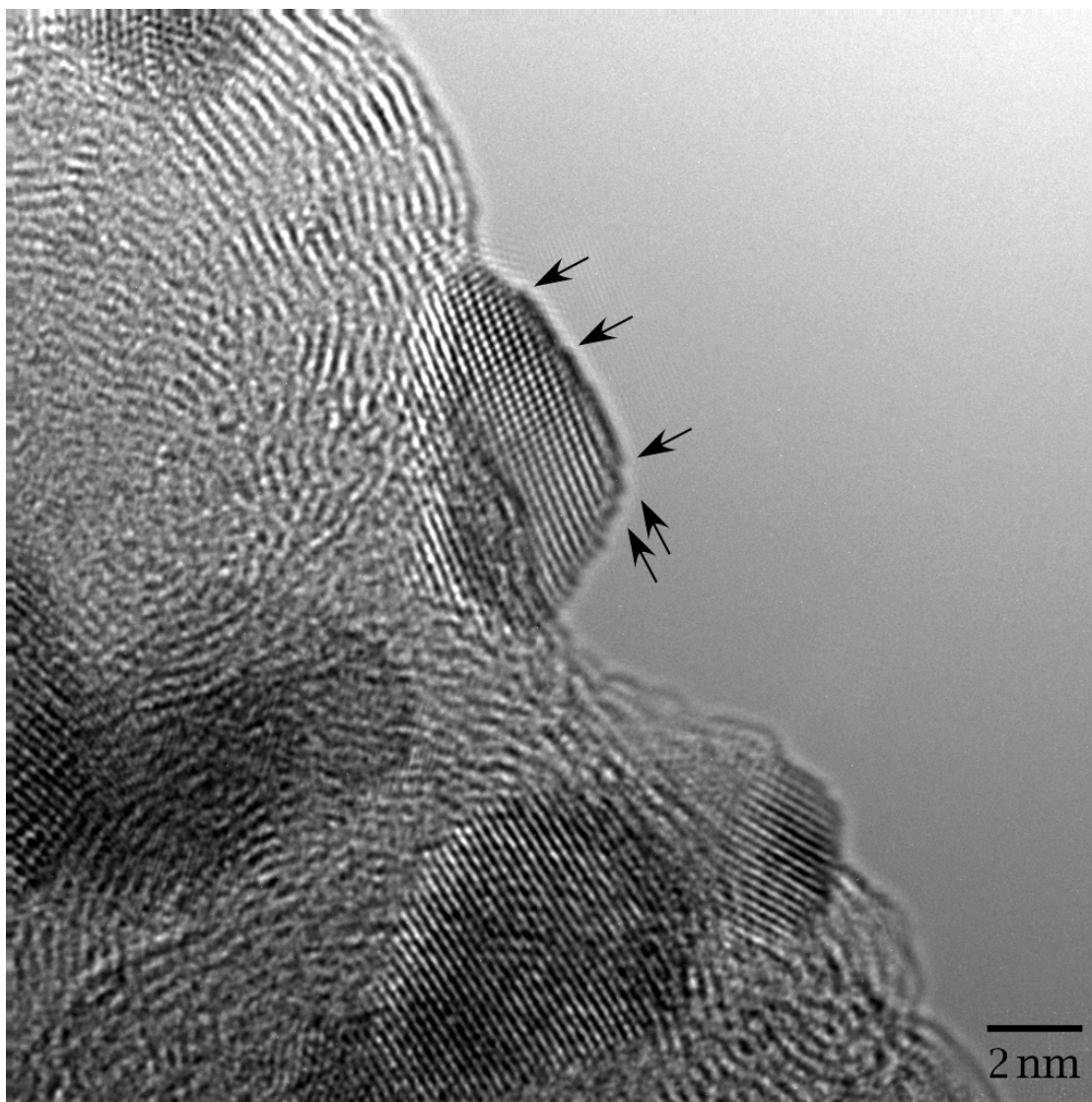


Fig. 3: The same specimen area as in Fig. 2, but recorded at a different focus setting of the objective lens. The arrows point at model atomic steps in the surface of a platinum particle. This image is #2 of a focus series.

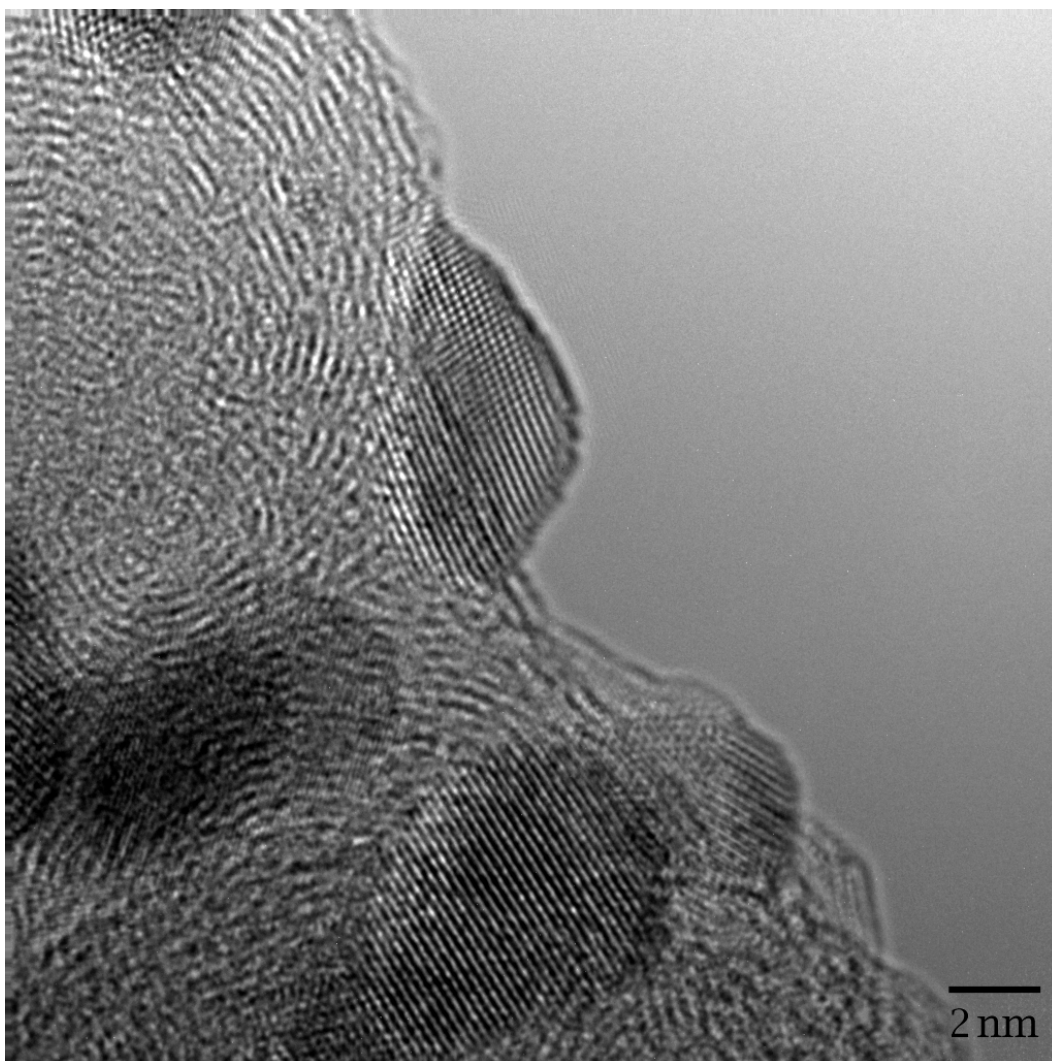


Fig. 4: The same specimen area as in Figs. 2 and 3, but recorded at a different focus setting of the objective lens. This image is #3 of a focus series.

Remarkably, the particle in Figs. 2, 3, and 4 does not have a particularly regular shape because it resides in a region where the globular carbon support exhibits negative curvature. In this location, the platinum particle can maximize its contact area with the support and minimize the area of its free surfaces by adopting a lens-like shape. From the viewpoint of catalysis, this situation is disadvantageous because introduces the active surface area per unit volume.

Exit Wave Reconstruction and Strain Analysis

Figures 5, 6, and 7 show a corresponding set of three images that are part of a defocus series we have obtained from the material we received from E-Tek. In contrast to Figs. 1, 2, 3, and 4, however, the particle imaged here (in the center) is not sticking out into the specimen hole. Therefore, the pattern that represents the atomistic structure is superimposed with the speckle pattern of the carbon support film. The viewing direction of the three images corresponds to $\langle 110 \rangle$, the same viewing direction as in Figs. 1, 2, 3, and 4. However, the shape of the particle in the center of Figs. 5, 6, and 7 appears much more globular and less faceted than the particles in Figs. 1, 2, 3, and 4. Still, a tendency for faceting is recognized at the bottom right, where an extended section of the surface is parallel to $\{111\}$.

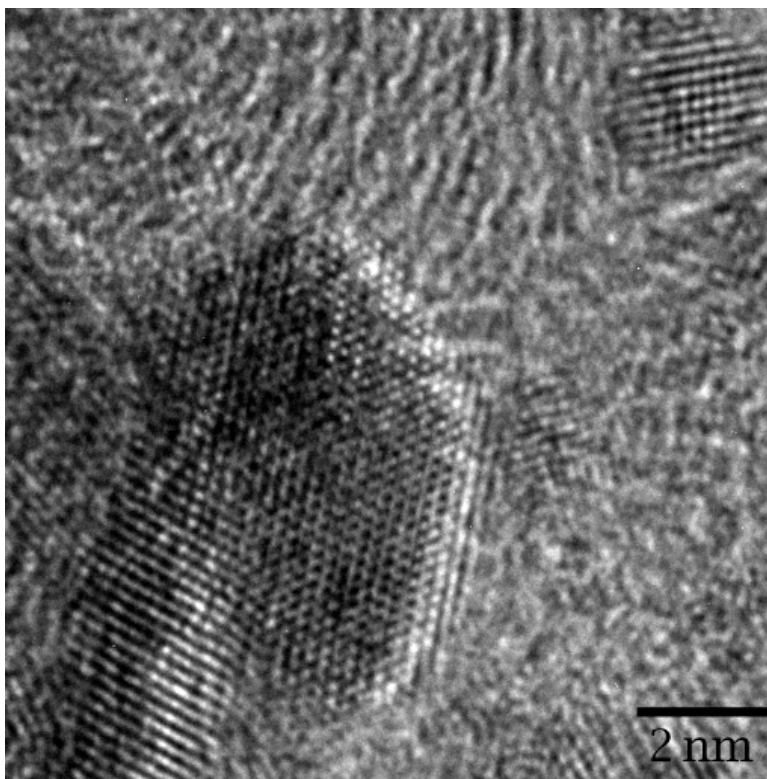


Fig. 5: Atomic resolution image of Pt catalyst particles on globular carbon support (E-Tek). The arrow points at a region in which limitations of the electron optical imaging system cause the appearance of lattice fringes in the hole (“delocalization”). This image is #1 of a focus series.

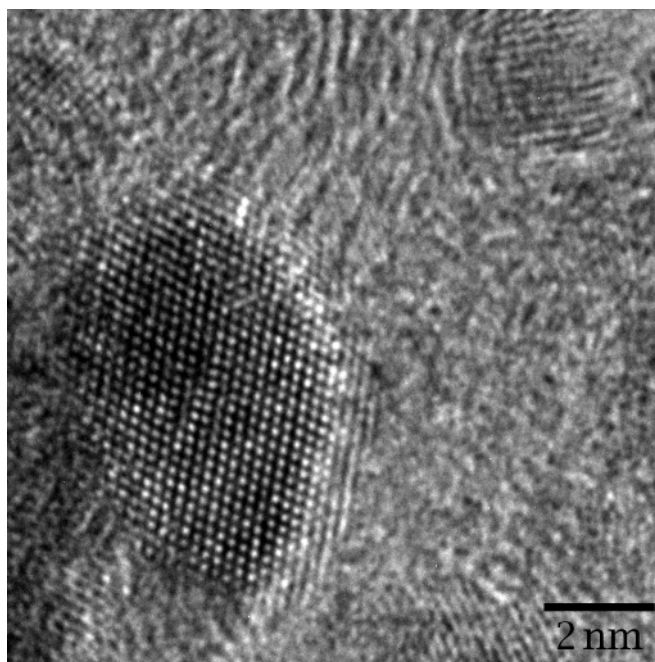


Fig. 6: The same specimen area as in Fig. 5, but recorded at a different focus setting of the objective lens. The arrows point at model atomic steps in the surface of a platinum particle. This image is #2 of a focus series.

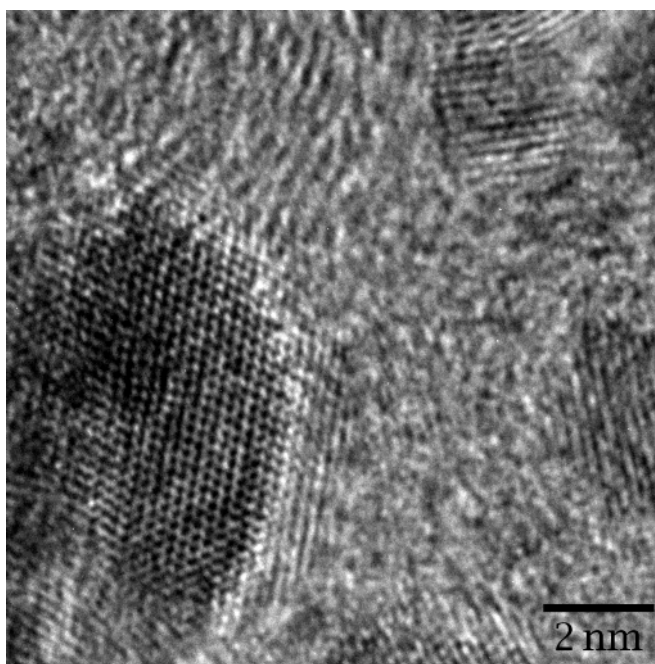


Fig. 7: The same specimen area as in Figs. 5 and 6, but recorded at a different focus setting of the objective lens. This image is #3 of a focus series.

Again, comparison between the three images in Figs. 5, 6, and 7 exposes the problems related to HRTEM imaging. In Fig. 5, the atomistic structure appears with

a weak and confusing contrast. In Fig. 6, in contrast, the atom columns appear as white spots with a strong contrast. In Fig. 7, finally, the atom columns also appear with a strong contrast, but this time they are dark.

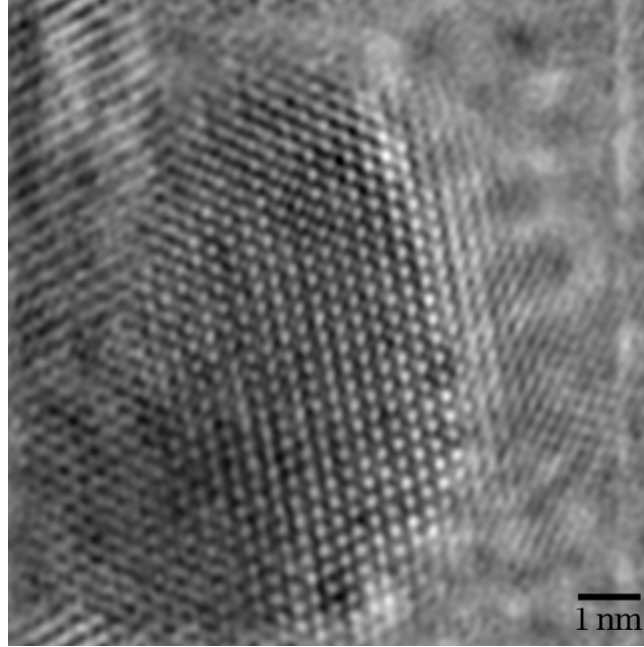


Fig. 8: Amplitude of the exit wave reconstructed from the focus series of Figs. 5, 6, and 7.

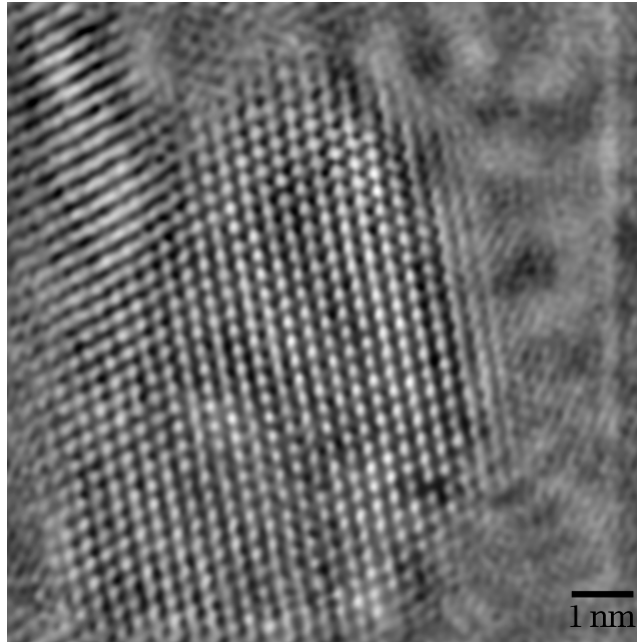


Fig. 9: Phase of the exit wave reconstructed from the focus series of Figs. 5, 6, and 7.

Figures 5, 6, and 7 and further images of the same focus series have been processed for construction of the complex-valued electron exit wave amplitude. The amplitude and the phase we have obtained by this procedure are shown in Figs. 8 and 9. Both images exhibit a substantial reduction of noise in the speckle pattern constituting the background. The more intuitive of the two images and the one that provides the strongest contrast pattern is the phase image in Fig. 9. It is a general experience in HRTEM that the phase provides the most directly interpretable information. Still, "ghost" fringes are observed to leach out beyond the area of the particle. This indicates that the reconstruction of the exit wave function has not completely removed the effect of the limited transfer capability of the microscope for high spatial frequencies. The reasons for this problem are presently being investigated.

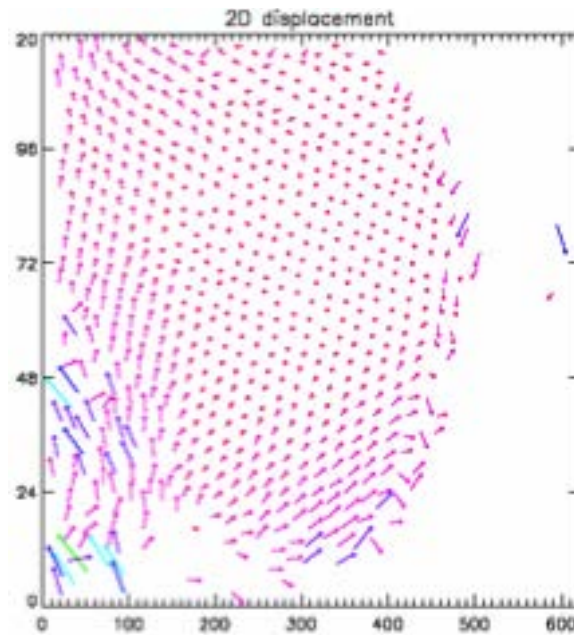


Fig.10: Local displacement derived from the phase of the exit wave reconstructed from the focus series of Figs. 5, 6, and 7.

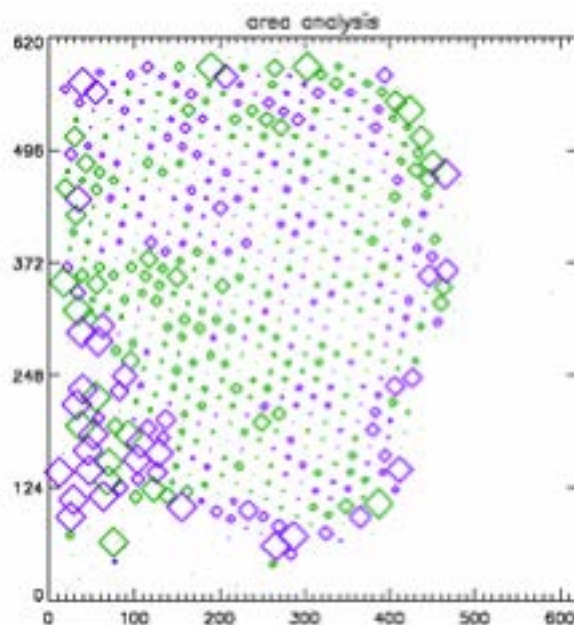


Fig. 11: Local volume expansion derived from the phase of the exit wave reconstructed from the focus series of Figs. 5, 6, and 7.

In spite of the relatively poor quality of the exit wave reconstruction we have achieved so far, we have further analyzed these images with respect to strain in the particle. For this purpose, we have applied the software package LADIA. Basically, this software fits Gaussian intensity profiles to the intensity maxima in the phase image (Fig.) and compares the position to the position of the points of a two-dimensional reference lattice. Evaluating the relative position of the experimental intensity maxima with respect to the reference lattice points, the algorithm determines the local displacement and the volume expansion at each point in the image. Figures 10 and 11 show the result we have obtained by analyzing Fig. 9 in this way. Interestingly, Fig. 11 exhibits compressive strain at the periphery as well as in the middle left of the platinum particle. Figure 10 exhibits correspondingly strong displacements in these areas.

These results demonstrate that quantitative analysis of high-resolution images by means of focus series, exit wave reconstruction, and strain analysis provide much more detailed information than plain HRTEM images about properties of the catalyst particles that are of prime interest with respect to their catalytic activity in fuel-cells.

Experimental Target 10: Simulations of Alloys

Synopsis:

Methods to simulate HRTEM images of alloys were developed to allow interpretation of atom-resolved images.

Detailed Report:

2. Image Simulation

The ability to simulate HRTEM images is an invaluable tool. For instance, it is possible to test whether or not the necessary resolution is attainable to solve a particular problem before expending any time at the microscope. Image simulation can be performed with readily available software packages. The primary inputs to this software are microscope parameters and an object model structure. The practicing electron microscopist can judiciously select microscope operating parameters for which the simulation is to be performed. The object model structure, on the other hand, may not be known. So, simulations are usually performed for a host of structures. In the case of the fuel cell catalyst particles in question, the purported object structure is assumed to be a truncated octahedron. The model structure is specified by the atom positions which comprise it. The truncated octahedron is built-up by assuming that the atoms of the Pt particles pack in a face-centered cubic fashion.

The first image simulation task in this undertaking was to test whether or not exit-wave reconstruction could produce the desired result as discussed above. For this purpose a defocus series of a Pt particle was simulated. Three images from this defocus series are shown in figs. 12, 13, and 14. These images are the 1st, 10th, and 20th images of the defocus series, respectively.

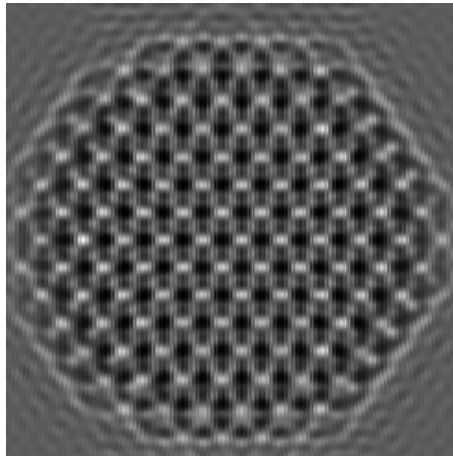


Fig. 12: The 1st image of a simulated defocus series of a Pt particle viewed in the <110> direction.

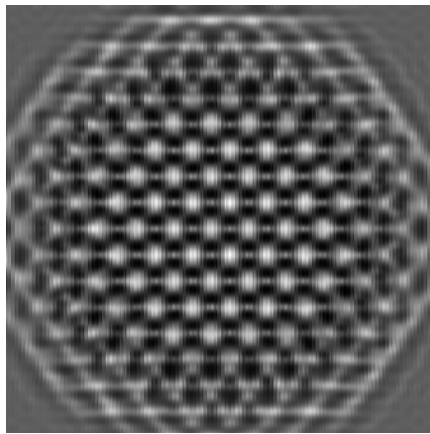


Fig 13: The 10th image of a simulated defocus series of a Pt particle viewed in the <110> direction.

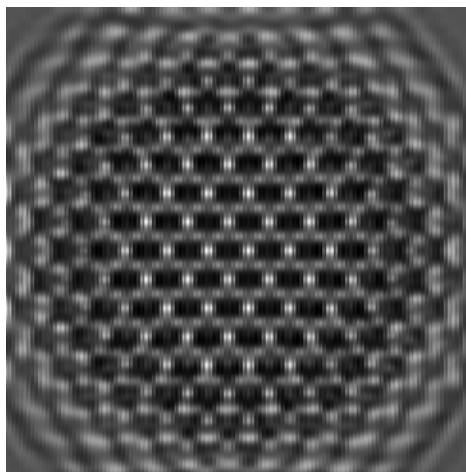


Fig. 14: The 20th image of a simulated defocus series of a Pt particle viewed in the <110> direction.

It is clear from these images that the defocus of the primary imaging lens has a significant effect on the contrast of the metal atom columns. That is, the weak and confusing contrast changes substantially with the defocus setting. Also, the aforementioned artifacts are readily observed in these simulated images.

The simulated focus series was processed to perform the exit wave construction. The results of the construction are shown in figs. 15 and 16. Both figures show a substantial reduction in the aforementioned artifacts. Specific attention should be paid to the phase image, fig. 16. The delocalization artifact seems to have been removed. Also, the atom columns that constitute the particle appear with a much stronger contrast. Metal atom columns at the particle edge are clearly recognizable. It can be concluded that the exit wave reconstruction method produces the desired result. However, the reason why exit wave reconstruction from an experimental defocus series has not produced the desired result is not clear. Further experimental investigation needs to be conducted.

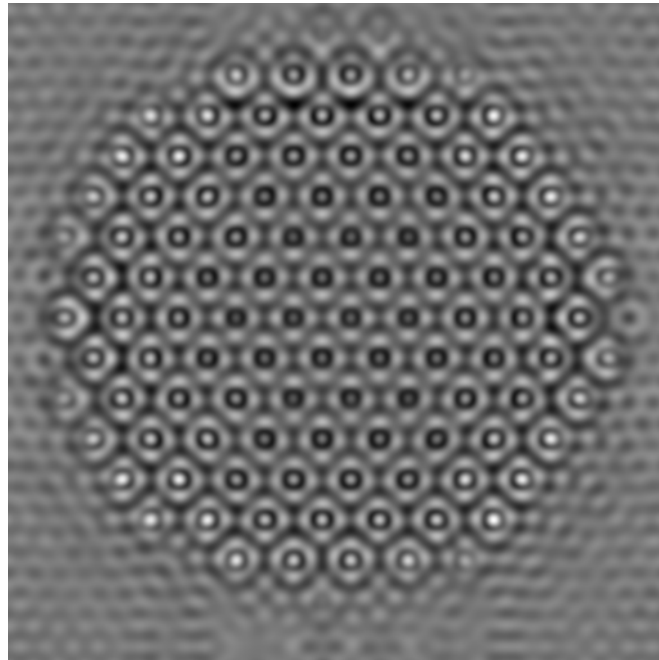


Fig. 15: Amplitude of the exit wave reconstructed from the simulated defocus series.

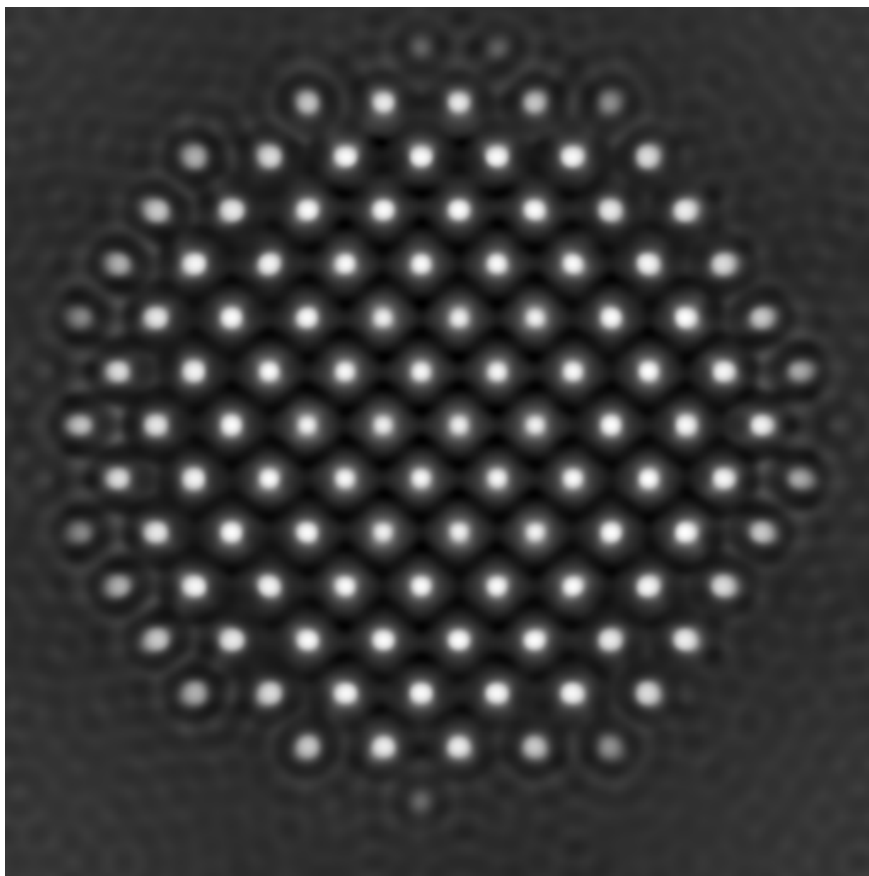


Fig 16: Phase of the exit wave reconstructed from the simulated defocus series, holey carbon support film.

Experimental Target 11: Simulations of support-particle interactions

Synopsis:

MD simulations of support-particle interactions were combined with microscopy to reveal the influences of the interaction on structure and, for alloys, phase separation of elements.

Detailed Report:

Understanding the strained structure of supported catalysts from molecular dynamics simulations -- A case study for PEM fuel cell electrocatalysts

Ram Subbaraman, Jay Adin Mann Jr and Tom Zawodzinski Jr.

Structure of supported nanocatalysts plays a significant role in kinetics of fuel cell reactions. An approach to understanding the structure from the basis of interaction energy between the nanocatalyst and support is presented. The effect of particle size on the "strain" observed through the nanoparticle is discussed. Effect of alloying elements and nature of support are discussed. Bond orders for atoms in the clusters were calculated to further understand the presence of a secondary Mackay transformation. Geometric utilization of catalyst particle based on the change in surface area due to the change in shape of the particle is estimated. Application of the results from the MD simulations for HRTEM simulations and design of new catalyst materials are discussed. Trapping of the particles by the support is described in terms of *Lévy* diffusion process. Particle size effect and shapes are discussed.

Introduction

Electrocatalysis of oxygen and hydrogen are the two main characteristic reactions for fuel cell operation. Catalysts of platinum and platinum based alloys are commercially used as fuel cell catalysts. Recent drive towards commercialization of fuel cells have led towards use of supported catalysts. Platinum electrocatalysts are dispersed as small particles on high surface area conductive supports for effective use of costly Pt. The size and structure of platinum particles plays an important role

in the oxygen reduction kinetics for fuel cell applications in terms of both electrocatalytic activity and practical application of catalysts. Carbon-supported platinum (denoted as Pt/C) shows a large surface area and increased catalytic activity. Alloy catalysts with various transition metals were employed to increase the catalytic activity and to reduce the cost. Various Pt-based alloy catalysts (binary, ternary and quaternary alloy) have been tested for last two decades. Many researchers have reported that Pt-based alloy catalysts showed higher activity than Pt-alone [stamenkovic2005], [stamenkovic22005], [stamenkovic2007], [Nenad2003] .

The effect of Pt crystallite size on the kinetics of the oxygen reduction reaction is a long-standing problem in electrocatalysis. An excellent review of experimental work with carbon-supported Pt was presented by Kinoshita [kinoshita1990] for work prior to about 1990. Kinoshita concluded that the change in fraction of surface atoms on the (100) facets of Pt nanoparticles, which were assumed to be cuboctahedral, could be correlated to the specific activity, the activity per unit area of Pt. The primary method for physical characterization of nanoparticle catalysts is transmission electron microscopy (TEM). Because the support is electronically conducting, the materials are free of nuisances like charging, and the samples are easily prepared for microscopy, e.g., dispersion in alcohol and adsorption onto a carbon grid full of holes. The large difference in electron scattering cross section between carbon and the metals used in electrocatalysts makes the metallic phases easy to distinguish from the carbon support. Essential properties like particle size and number density are relatively easily obtained and do not require a sophisticated microscope. However, the nanosize of these particles presents challenges to their microstructural characterization. Lattice structure characterization can be obtained by high-resolution electron microscopy (HREM), which can reveal the presence of defects, such as dislocations and/or twins. The advantages of the application of TEM in catalyst characterization are described in several review articles [Datya1992],[poppa1993],[HRTEM2]. More specifically, HREM has been extensively used to determine faceting planes, geometric shapes, the presence of surface steps,

as well as the size and distribution of supported metallic catalysts [sattler1986],[smith1985]. The structures observed using HRTEM shows the actual structure of electrocatalysts to be a derivative of cuboctahedral or icosahedral structure. Obtaining a realistic structure for the nanoparticle is the main focus of this work.

Molecular dynamics (MD) simulation has been shown to be a very useful tool for the understanding and investigation of physical processes in the condensed state. The areas that can be studied by MD simulation are diverse. In recent years, attempts have also been made to study metallic systems using MD simulations. For this kind of simulation, a potential function which has the characteristics of metallic bonding is required. This means that the potential should be able to account for the repulsive interaction between atomic cores as well as the cohesive force due to the local electron density. It maybe beneficial to use simple semi empirical function which account for the characteristics of metallic bonding for some applications. Recently, such semi empirical potentials have been proposed by various researchers [Daw1984], [finnis1984], [sutton1], [guevara1995]. The effect of local density is accounted for through the inclusion of a many body term in the potential function. The Sutton and Chen potential is an example of these potentials which has been quite popular among various researchers. It has been shown to describe the behavior of various metals with reasonable accuracy. The properties of small metal clusters have also been studied by using the SC potential and the results are found to be consistent with experimental findings [macka2]. These results indicate that the SC potential is very useful to gain insight into many important industrial processes where small metal clusters are an essential component of the process (e.g. catalytic reactions). The experimental characterization of the microscopic platinum morphology and its effect on activity is difficult. The situation is made worse by the fact that it is hard to carry out experiments with controlled and well defined micropores and with a uniform platinum loading. Platinum supported on carbon surfaces are our main system of interest. It is our aim to use the technique of molecular dynamics and Sutton Chen potentials to understand the structure of nanoparticles.

In order to understand the structure of supported catalyst, simulation of metal on substrate need to be done. However, simulation studies of the platinum-substrate systems are rare. The simulation studies which do focus on the metal-substrate system normally use a Lennard Jones (LJ) potential for platinum-platinum interactions. Recent studies involving platinum cluster adsorption on graphitic substrate have been reported [liem1], [liem2], [liem3], [balbuena2006]. The support is usually treated using a mixed potential developed by Steele [steele1973] and other variations of these potentials. Experimental evaluation of interaction between carbon supports and nanoparticles have been recently reported [ram1]. Optical properties of individual particles were measured from a colloidal dispersion in water and Lifshitz theory based method was used to evaluate the Hamaker coefficients for platinum, platinum alloys and carbon particles. Hamaker [hamaker1937] developed the distance dependence of the free energy change of macroscopic bodies by performing a pair-wise summation over all the atoms in the bodies. This model is approximate and is replaced by using the Lifshitz formulation [lifshitz1955]. The Hamaker coefficient is a material property that depends on the electron densities of the materials involved and the dielectric properties of the intervening media. In this analysis, the Van der Waals force of interaction is treated as a result of fluctuations in the electromagnetic field between two objects, modified by the intervening media. Knowledge of the Hamaker coefficients for interaction of materials gives a means to construct metal-substrate potential function for our simulations.

In the following sections, a brief description of potentials used for the simulations and conditions used during simulations are given. Results obtained from the simulations for unsupported and supported catalyst particles are discussed followed by studies performed for alloy nanoparticles. Trapping of the nanoparticles by the support is discussed based on $\alpha - \text{Lévy}$ diffusion process is described. The existence of Mackay transformation for small platinum clusters is verified.

Methodology

Metal atom cluster potentials

Platinum and other metal atom clusters are simulated in condensed state. Sutton-Chen potentials are used for setting up the interaction between platinum and other metal atoms in the cluster. The SC potential combines the van der Waals attractive interaction at long range with the many-body cohesive interaction at short range and has been shown to predict the properties of a range of fcc metals quite well [sutton1]. Because of its simple form, it is easy to use for different metals and it has also been generalized for random binary fcc alloys by Raffi-Tabar and Sutton [mixing3]. This allows us to simulate alloys and elemental metals easily, without the introduction of further potential parameters. The general formulation of the potential is given by,

$$U = \epsilon_{pp} \sum_{i=1}^N \left[\frac{1}{2} \sum_{j \neq i}^N \left(\frac{\sigma_{pp}}{r_{ij}} \right)^n - c \sqrt{\rho_i} \right]$$

and the term ρ_i is defined as,

$$\rho_i = \sum_{j \neq i}^N \left(\frac{\sigma_{pp}}{r_{ij}} \right)^m.$$

Where r_{ij} is the separation distance between atoms i and j , c is a dimensionless parameter, ϵ_{pp} is the energy parameter, σ_{pp} is the lattice constant and m and n are positive integers with $n > m$. The energy parameters are typically calculated from the equilibrium lattice parameters and the lattice energy for fcc lattice. The list of values of the parameters for various metals of interest is shown in table (Table MD1). Even though SC potential is a many body potential, the

interaction force on each atom can be evaluated as a sum of pair wise contributions:

$$F_i = \sum_j^N F_{ij}.$$

By differentiating equation (SuttonChenpot) with respect to r_i and rearranging the resulting expression, the interaction force F_{ij} , is given by,

$$F_{ij} = \epsilon_{pp} \left[n \left(\frac{\sigma_{pp}}{r_{ij}} \right)^n - \frac{cm}{2} (\rho_i^{-1/2} + \rho_j^{-1/2}) \left(\frac{\sigma_{pp}}{r_{ij}} \right)^m \right] \frac{r_{ij}}{r_{ij}^2}$$

Ideally metal atom interactions require averaging over all the atoms in the cluster instead of a pair potential. The interaction force in equation force contains an attraction term which is a function of the local distribution of atoms in the cluster. This suggests the potential accounts for the local neighborhood in the cluster. Interaction forces between atoms are based on identifying the atoms in the local neighborhood of every atom. For the simulations described in the following sections, interaction forces were calculated for all the atoms in the cluster. The number of atoms in the cluster being small ensures the simulations are not computationally expensive. Table MD1 lists the values of parameters for different metal atoms used in our simulations. SC parameters for alloys are estimated using the combination rules [mixing1], [mixing3], [mixing2]. The alloy clusters were simulated using the

$$\epsilon_{ij} = \sqrt{\epsilon_i \epsilon_j}, m_{ij} = \frac{m_i + m_j}{2}, n_{ij} = \frac{n_i + n_j}{2}, \sigma_{ij} = \frac{\sigma_i + \sigma_j}{2}$$

hybrid parameters.

Table 1: Parameters used in simulations

Metal Atom	$\varepsilon_{pp} \times 10^2$ (eV)	σ_{pp} (Å)	C	m	n
Platinum	1.9833	3.92	34.408	8	10
Gold	0.12793	4.08	34.408	8	10
Cobalt	1.5566	3.54	39.431	6	9
Copper	1.2382	3.61	39.432	6	9
Iron	5.2899	3.0	11.9067	6	9
Rhodium	0.49371	3.8	144.41	6	12

Simulations are performed under constant temperature conditions. There are various thermostats available for controlling the temperature of the MD system [nose1984], [nose1991], [Berendsen1984]. Berendsen thermostat [Berendsen1984], [berendsen1994] was used for controlling the temperature for our system. The thermostat works based on velocity scaling. Even though this thermostat is not designed for canonical ensembles, the deviation of velocities from a typical canonical ensemble is found to be small. Velocity is scaled such that the kinetic energy is matched up with the set temperature. Typical scale factor used in a Berendsen thermostat is given by,

$$\lambda = \sqrt{1 + \frac{\Delta t}{\tau_T} \left(\frac{T}{T_o} - 1 \right)}$$

Here, T_o is the set point temperature, Δt is the integration time step, and τ_T is a constant called the rise time of the thermostat. It describes the strength of the coupling of the system to a hypothetical heat bath. The larger τ_T , the weaker the coupling; in other words, the larger τ_T , the longer it takes to achieve a given T_o after an instantaneous change from some previous T_o . Value of τ_T was chosen such that the average variation in the temperature at a given set point was found to be within $\pm 2 - 3\%$. The velocities were found to be fit a Gaussian distribution

further suggesting lower deviations from canonical ensemble. Verlet algorithm for used for solving the equations of motion. Typical temperature used for most cases was 300K. Time steps of 1 femtosecond were used for the simulation. Typical length of the simulation was kept at 4 nanoseconds. Lengths of simulations were varied to ensure the proper equilibration of the system. The potential and kinetic energies were calculated at all times and were found to be equilibrated for the particular temperature during the length of the simulation. The initial structures are assumed to exist at 0K. The temperature is typically ramped up at the rate of $0.0003125\text{K} / \text{fs}$. Different rates of heating and cooling have also been tested. Simulations were performed using a Fortran 90 code executed using Intel Fortran compiler 10.025 on university's supercomputing cluster. Typical running time for a 147 atom cluster was found to be 22 hours for 5 ns of simulation time on the cluster.

The size of the simulation box was 50 times the lattice parameter from SC potential. The large size of the box ensures no boundary effects due to the domain were observed during the simulation. Two types of boundary conditions were used for the simulations. For the case of unsupported or free nanocluster, periodic boundary condition was applied for all 6 faces of the box. Bottom corner of the cube was placed at $\langle 0, 0, 0 \rangle$. For the case of supported catalyst, periodic boundaries were restricted to x and y axes. The xy plane along the $-z$ direction is considered to be the carbon support. So the xy planes along the z axis are therefore considered to be reflective in nature. The velocities and the displacements are reflected upon reaching these faces of the box. The hybrid boundary condition is validated by observing that the trapping of nanoparticle by the substrate during the simulations. The equilibrium structure observed for the supported nanoparticles are typically observed to settle closer to the xy along the $-z$ axis.

The choice of number of atoms used for the simulations is based on closed shell "magic numbers". Metal nanoparticles are typically found to exist in icosahedral or cuboctahedral shapes [HRTEM1]. Initial starting structures were chosen for two different cases; (i) Icosahedron (ii) Cuboctahedron. The closed shell

structures were the focus of this study. One of the main focuses of this work is to estimate the effect of carbon support on the structure of the nanoparticle. The closed shell structures give us a good approximate for the starting structure to enable us to calculate the strain/distortion of the structure due to the interaction with the support. In order to estimate the strain on the structure of nanoparticles due to the interaction with the support, displacement fields between equilibrated structures of supported and unsupported nanoparticles are compared. Strain field for the cluster depicts the direction of the strain vector for the particle. Typical strain field data gives us information regarding the extent/magnitude and the direction of strain vectors due to the support-nanoparticle interaction. The atoms are numbered and tracked throughout the simulations. Every atom's position, velocity and temperature of the system are recorded during each simulation.

Interaction potential between nanoparticle and support

Simulation of supported catalysts is of interest due to the wide application of supported catalysts. In order to simulate the interaction between the support and nanoparticle various types of potential functions have been used in the literature. One of most common supports/substrate of interest is graphite. Potential function developed by Steele [steele1973] has been typically used for this purpose. The Steele potential is suitable for surfaces with a different kind of crystallinity. It generates a potential surface with adsorption maxima and minima which is a result of the spatial distribution of the carbon atoms on the surface. However this potential is ideally suitable for a graphitic surface with no modifications. Lennard-Jones potentials have also been used as a model potential form for simulating adsorption of platinum nanoparticles on carbon support. The potential can be related to experimental information through identifying the energy minimum and minimum distance of separation. The ideality involved in the process of development of these potentials limit the applicability of these potentials to obtain a realistic supported nanoparticle structure.

Interaction forces between two bodies in close proximity arise from various contributions such as, double layer, structural, steric, depletion, hydration and hydrophobic forces. The one type of interaction which is ubiquitous is the Van der

Waals interaction. The Hamaker coefficient formalism represents a conventional and convenient way of assessing the magnitude of this interaction [hamaker1937]. The Hamaker coefficient is related to the optical properties of materials. Hence the knowledge of the material properties would lead to estimate a more realistic interaction parameter for the actual material of interest. Recently, Hamaker coefficients for platinum and platinum alloy nanoparticles and carbon supports have been estimated experimentally [ram1]. The Hamaker coefficient for interaction between the platinum nanoparticle and the carbon support can be simply derived from the individual Hamaker coefficients. The interaction energies from the Hamaker coefficient are estimated using the formulation of Hamaker for estimating the London forces. A $\frac{1}{r^6}$ term was used for estimating the attractive component and a Born approximation on $\frac{1}{r^{12}}$ was used to estimate the repulsive regime of the energy [feke1984].

$$U_{MmS} = \frac{-A_{MmS}}{6}[G1 + G2 + G3] + 4 \frac{4! * A_{MmS}}{10!} \left(\frac{\sigma}{R_N} \right)^6 \left(\frac{1}{R} \right) f(\lambda, R)$$

$$G1 = \frac{4R_N R_S}{(R_N + R_S + l)^2 - 4R_N R_S} \quad G2 = \frac{4R_N R_S}{(R_N + R_S + l)^2}$$

$$G3 = \ln \left(\frac{(R_N + R_S + l)^2 - 4R_N R_S}{(R_N + R_S + l)^2} \right)$$

$$f(\lambda, R) = \left[\frac{-R^2 - 7(\lambda - 1)R - 6(\lambda^2 - 7\lambda + 1)}{(R - 1 + \lambda)^7} + \frac{-R^2 + 7(\lambda - 1)R - 6(\lambda^2 - 7\lambda + 1)}{(R + 1 - \lambda)^7} + \frac{R^2 + 7(\lambda + 1)R + 6(\lambda^2 + 7\lambda + 1)}{(R + 1 + \lambda)^7} + \frac{R^2 - 7(\lambda - 1)R + 6(\lambda^2 + 7\lambda + 1)}{(R - 1 - \lambda)^7} \right]$$

Where A_{Nms} refers to the Hamaker coefficient of interaction between nanoparticle (N) and the support (S) in the presence of a medium (m).

Typical Lennard-Jones fit potentials used for modeling the interaction of support are derived from the information regarding the minimum energy and distance for the equilibrium interaction. Actual potential form of the function plays an equally significant role as the minimum energy for interaction. Hamaker and Born formalisms were used to estimate the full functional form for interaction potentials. The potential form is then compared to the Lennard Jones fit obtained from the minimum energy parameters. Figure (Figure MD1) shows the comparison between the two energy forms. Even though the minimum energy and the distance of separation are matched between the potentials the steepness of the L-J potential leads to an artificial high attractive force for the system. This force is found to be significantly higher compared to the force calculated from the full functional form. This suggests that the use of L-J fits to model the support with nanoparticle leads to an overestimation of the interaction and should hence not be used for these types of calculations. The influence of carbon support is treated as a mean field approximation with the use of the Hamaker formalism. The absence of significant structural characteristics of the amorphous carbons typically used for fuel cell

catalysts validates this assumption.

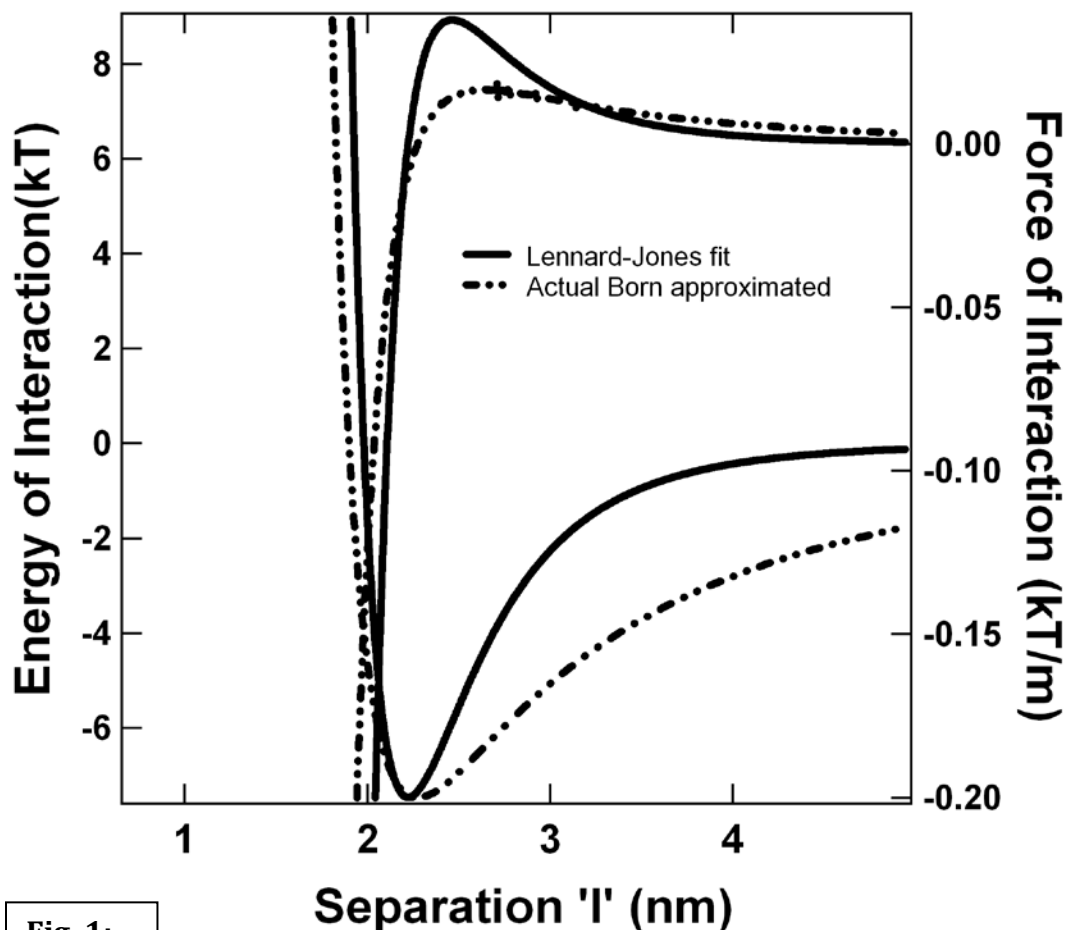


Fig. 1:

One of the main advantages of the Hamaker formalism is the wide applicability of the method to various materials. In order to study the effect of different substrates on the structure of catalyst observed, the only information necessary is that of the individual Hamaker coefficients for the materials of interest. Knowledge of Hamaker coefficients for different types of carbon is sufficient to understand the effect of varying substrates for nanoparticles.

Energy of interaction between the platinum nanocluster and carbon support as a function of size was estimated. Figure (Figure MD2) shows the forces and energies of interaction between nanoparticles and support as a function of particle sizes. The force of interaction is significantly dependant on the size of the nanoparticles. The magnitude of the maxima observed in the force function

determines the maximum attractive force experienced by the nanoparticle. Higher the magnitude of this force suggests a higher interaction energy suggesting a stronger binding energy between the nanoparticle and the support. From figure (Figure MD2), the smaller particle is found to have the smallest interaction force. In order for a nanoparticle to be effectively trapped by a support the particle must experience a significant interaction with the support. Effect of the decreasing particle size will be discussed in detail in the following sections. The 55-atom cluster was found to have a weak binding energy with the support consequently the nanoparticle is found to be untrappable by the support.

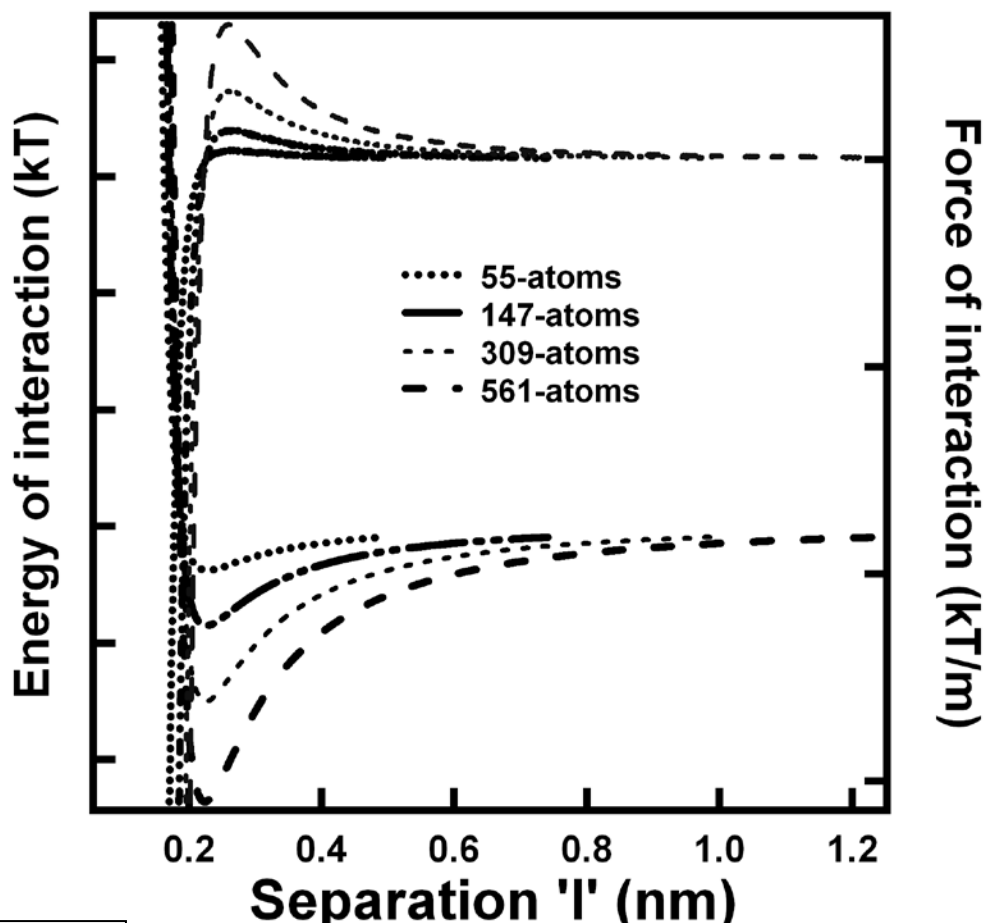


Fig. 2:

This work primarily focuses on platinum and platinum alloy nanoparticles. Effects of varying initial structure are considered. Temperature effect on the strain exhibited by the particle both in the presence and absence of the support are

considered to understand the effect of substrate. Simulations were carried out for a model alloy materials to understand the effectiveness of the methodology and to justify its applicability to novel systems. Effect of support on phase dispersion in alloys and the stabilization of materials have also been discussed.

Results and Discussion

Icosahedron and cuboctahedron structures were used as starting structures. The cuboctahedron and the icosahedron are two very interesting polyhedra; the first one is an Archimedean solid whereas the second one belongs to the class of the five Platonic solids. Besides these historical classifications and their rather different apparent geometrical shapes, cuboctahedra and icosahedra are very closely linked, since a cuboctahedron can be transformed into a icosahedron through mathematical transformations. One of the main differences between the icosahedral and cuboctahedral structures is the symmetry exhibited by the atoms. The 5-fold symmetry is typically exhibited by the atoms in the vertices of an icosahedron. The top of the icosahedron consists of a pyramid structure with 5 equilateral triangular faces. The cuboctahedron on the other hand consists of a triangular face surrounded by square facets. A cuboctahedron can simply be carved from a fcc lattice by removing the atoms along the $\langle 111 \rangle$ plane parallel to the vertices of the atoms. Icosahedral and cuboctahedral shapes have been found as a common shape for metal atom clusters [HRTEM1]. Atom clusters of cuboctahedron and icosahedron could be inscribed in a sphere and as the cluster gets larger in number the particles exhibit a spherical symmetry. The number of atoms per shell is the same for both icosahedron and cuboctahedron.

Icosahedron starting structures were simulated using the algorithm developed by Yanting Wang [mack4]. Table (Table MD2) shows the comparison of number of shells and number of atoms with the radius of the particles. Particles of different shells were used as starting structures. Cuboctahedron structures were generated using a matlab code which identifies the atoms on a cuboctahedral shell from the fcc lattice of atoms. The differences in the symmetry of the particles are established by estimating the bond order parameters for the individual atoms in the

clusters. Typical icosahedron and cuboctahedron structures are shown in Figure (Figure MD3). The clusters correspond to 1415 atoms. Gaussview^(R) was used to visualize the atom clusters.

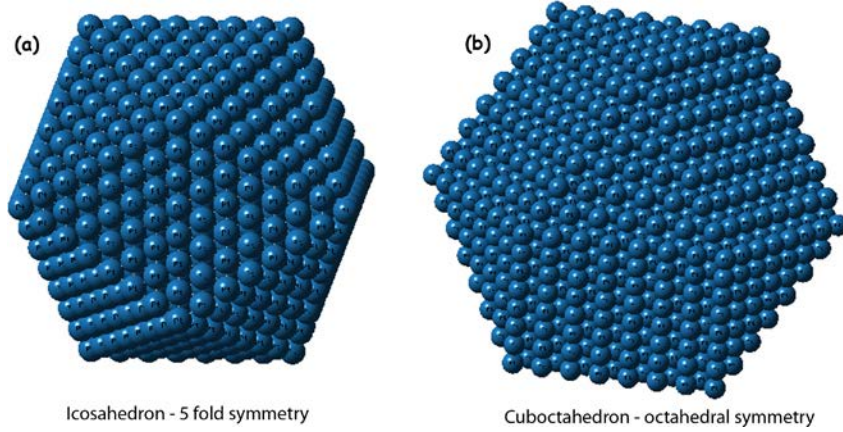


Fig. 3 a, b

Table 2. Cluster geometry

Shell number	N (icosahedron)	N(cuboctahedron)	Approximate diameter of cluster (nm)
1	13	13	0.510
2	55	55	1.071
3	147	147	1.579
4	309	309	2.08
5	561	561	2.631
6	923	923	3.142
7	1415	1415	3.702

Bond orientational orders [nelson1989], [BO2], [BO3] have been used to estimate the local structures of nanoparticles using the spherical harmonics for the individual atoms. There are several criteria used to identify local and extended orientational symmetries. Bond order parameter method [nelson1989], [BO2], [BO3] is an useful method which can be used to analyze the local crystalline structure as well understand the transformation between different crystallographies. To determine the orientational order, spherical harmonic basis functions $Y_{lm}(\theta(\vec{r}), \phi(\vec{r}))$ are associated with every bond joining an atom to its near

neighbors. Here, θ and ϕ refer to polar and azimuthal angles of vector \vec{r} in a given reference frame. The term bond refers to the unit vector \vec{r}_{ij} joining a reference atom i to any neighboring atom j within a cutoff radius r_{cut} . The cutoff radius is generally taken to be 0.75 times the lattice parameter for SC potential. For platinum atoms this value was found to be 3.09 Å. The function is calculated as an average over all atoms, surface and interior, and ensures all atoms in the first coordination shells are counted as near neighbors. To make the bonds independent of direction, only even l shaped harmonics are considered, which are invariant under inversion.

The local order around any atom i is an average over all its bonds with the neighboring N_{nb} atoms and given by,

$$q_{lm}(\vec{r}) = \frac{1}{N_{nb}(i)} \sum_{j=1}^{N_{nb}(i)} Y_{lm}(\theta(\vec{r}_{ij}), \phi(\vec{r}_{ij})),$$

Considering only the even harmonics allows us to not worry about direction for a particular bond. Two invariant measures are used for calculation of bond orientational orders. Quadratic and cubic measures are conventionally used to estimate the bond orders for structures. A second order invariant can be constructed to give a local order parameter independent of the choice of reference system,

$$q_l(i) = \left[\frac{4\pi}{2l+1} \sum_{m=-l}^l |q_{lm}|^2 \right]^{1/2}$$

The average of q_{lm} overall N atoms in a cluster gives the global bond order parameter,

$$Q_l = \left[\frac{4\pi}{2l+1} \sum_{m=-l}^l |\bar{Q}_{lm}|^2 \right]^{1/2}$$

Where

$$\bar{Q}_{lm} = \frac{\sum_{i=1}^N N_{nb}(i) q_{lm}(i)}{\sum_{i=1}^N N_{nb}(i)}$$

The value of the global bond order parameter Q_l in a solid cluster depends on the relative bond orientations and has a unique value for each crystal structure. Based on local solid symmetry, it was found that cubic and icosahedral clusters have nonzero values of $q_l(i)$ for $l = 4$ and at $l = 6$ for those with icosahedral symmetry. Values of local symmetry for the individual atoms are plotted for $l = 4$ and $l = 6$ values respectively.

A third order invariant which is less sensitive to the definition of the nearest neighbors can also be defined,

$$W_l \cong \sum_{\substack{m_1, m_2, m_3 \\ m_1 + m_2 + m_3 = 0}} \begin{bmatrix} l & l & l \\ m_1 & m_2 & m_3 \end{bmatrix} \times \bar{Q}_{lm_1} \bar{Q}_{lm_2} \bar{Q}_{lm_3}$$

The coefficients, $\begin{bmatrix} l & l & l \\ m_1 & m_2 & m_3 \end{bmatrix}$ in the third order invariant equation (Wthird) are Wigner $3j$ symbols. $l = 2, 4, 6, 8, 10$ and $m = -l, -(l-1) \dots 0 \dots, l-1, l$ are considered. Table shows the values of the global bond order parameters as a function of the crystal structure. The second order invariants are calculated for various atoms in the clusters and the local bond order symmetry is shown in Figure

MD4. The choice of l used was based on the non zero values exhibited by the atoms in different symmetry groups. Icosahedral group typically exhibits zero invariant measure for l values less than 6. Cuboctahedral clusters on the other hand are made of fcc lattice and exhibit non zero values for $l = 2, 4, 6$.

Table 3: Value of the invariants for various crystals.

Geometry	Q_4	Q_6	W_4	W_6
FCC	0.19094	0.57472	-0.1593	-0.013161
hcp	0.09722	0.48476	0.1340	-0.012442
bcc	0.03637	0.51089	0.1593	-0.013161
icosahedral	0	0.66332	0	-0.16594
sc	0.76736	0.35355	0.1593	-0.013161

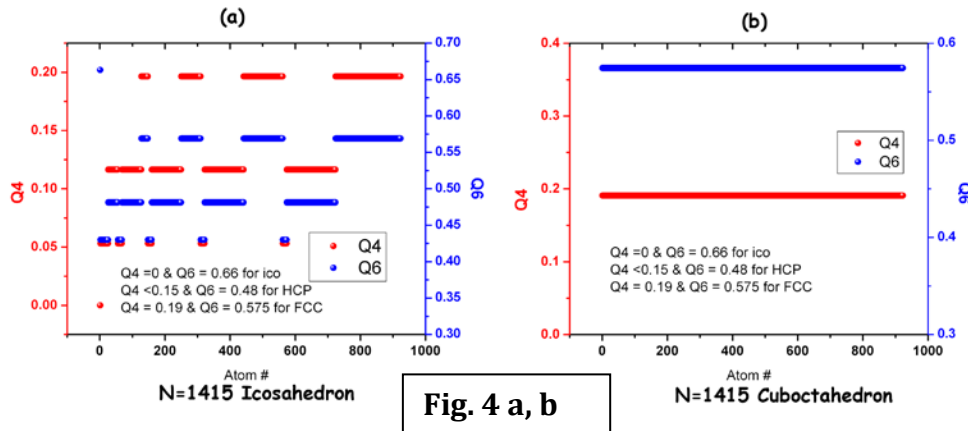


Figure MD4 shows the comparison of q_4 and q_6 for icosahedral and cuboctahedral structures. The cuboctahedral clusters typically show values of $q_4 = 0.19$ and $q_6 = 0.575$ corresponding to a fcc lattice. This stems from the fact that the cuboctahedral cluster was built from a simple fcc lattice. The icosahedral cluster on the other hand shows a mixture of fcc and hcp lattice structures. The central atom in the cluster has icosahedral symmetry. Atom #1 refers to the central atom and the values of q_6 and q_4 corresponds to that of a pure icosahedral cluster group. Only the values of second order invariant corresponding to equation (Qsecond) are presented in this work. The bond orders estimation helps us to

determine the final structure observed during simulations. Bond order parameters for unsupported and supported catalysts were calculated. Also Mackay transformation [mackay1969] corresponding to the structure transformation from an icosahedral symmetry to cuboctahedral symmetry are analyzed using the bond order calculations. The local bond order parameters were compared for different simulations. The bond order parameter distribution of the 0K cluster was used for comparison for the simulations. The deviation from the 0K structure determines the extent of distortion from the icosahedral structure for the simulated cluster.

1. Simulation Parameters

Simulations were performed at constant temperature for the clusters. Two main parameters were estimated during the simulation to ensure the equilibration of the system at the simulation conditions. The temperature of the system is measured based on the kinetic energy of the system and the potential energy of the system is calculated during every simulation step. The potential energy and temperature variations are compared. Figure MD5a shows the variation of temperature and potential energy as a function of simulation time. The values are compared from the time at which the system reaches the set temperature value. The variation in temperature was found to be within $1 - 2\%$ of the set temperature for all the simulations. The results corresponding to one such simulation is shown in the figure. The variation of potential energy was found to be in the same range as that of the temperature suggesting the energy equilibration in the system. Simulations were typically run for 5 ns to ensure the complete equilibration of the simulation

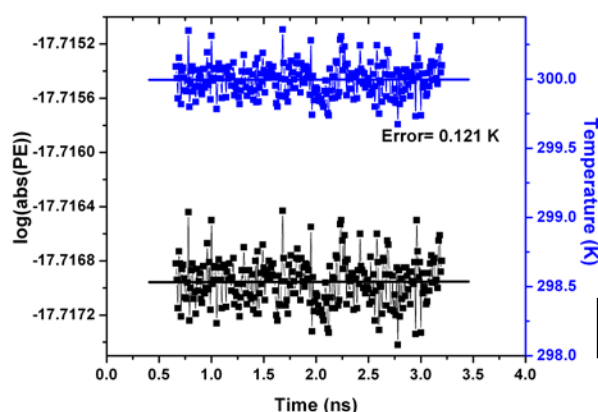


Fig. 5a Variations with Time

cluster.

The simulations correspond to the case of 309 atom cluster at 300K. One of the drawbacks of using Berendsen thermostat is that the possible deviation from a canonical ensemble. As a result one can only obtain average value for the properties of the system. One means to the test the deviation of system from canonical ensemble is to estimate the distribution of the velocities for the atoms in the cluster. Velocity distributions for the atoms at the end of simulation are shown in figure MD5b. Thermostats corresponding to canonical ensemble are known to produce velocities as a part of Gaussian distribution during the simulation. The velocity distribution obtained for our cluster using the Berendsen thermostat provides a distribution very close to Gaussian suggesting the system does not deviate too far from the canonical ensemble.

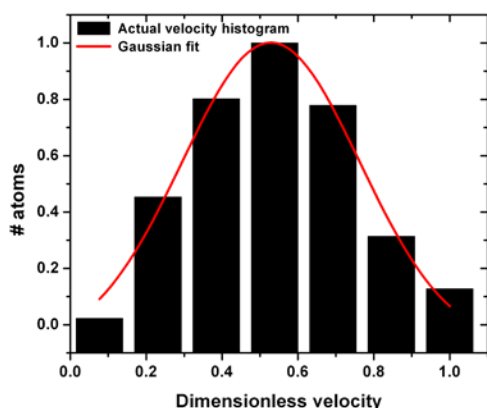


Fig 5b Velocity distribution

The advantage of using Berendsen thermostat is the ease of use in the integration algorithm. The thermostat is simple to implement and has been found to control the temperature of the system

effectively to within 2%. The individual thermodynamics properties however are subjected to errors due to the deviation of the system from canonical ensemble. This can be overcome to some extent by considering average quantities instead of the absolute quantities for the system.

2. Unsupported nanoparticle

Platinum nanoparticles were simulated with an icosahedral starting structure. Unsupported nanoparticle structures at the end of simulation are shown in figure (Figure MD7). The figures show structures corresponding to shells 4, 5, 6. The nanoparticles were equilibrated to 300K. The simulation times were varied from 5ns – 20ns. The structural variation with time was found to be minimal after 2ns. The platinum structure still exhibits the icosahedral 5-fold symmetry for the atoms on the vertices. Gaussview^(R) was used for graphical visualization of the cluster. The equilibrated cluster is found to exhibit symmetries similar to that of the 0K structure suggesting the stability of icosahedral structures. Transition metals such as Fe, Cu, Au and Ag have all been reported to have a stable icosahedral structure at low temperatures [lathioka1996]. The atoms however do exhibit slight deviations from their initial position suggesting the presence of a distribution of atom separations in individual atom clusters.

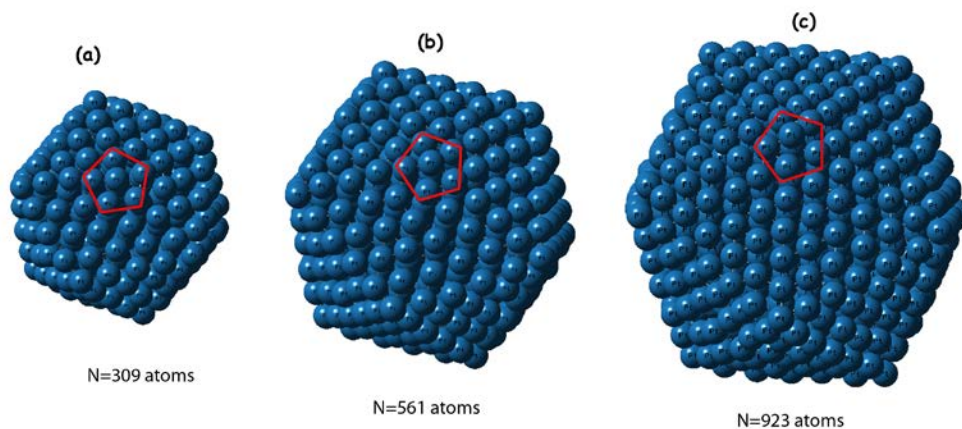


Fig. 6 a, b, c

Two main characteristics are evaluated for the structures obtained. Radial distribution function for the atoms is plotted in figure (Figure MD8). Radial

distribution functions for the clusters are obtained by estimating the distance of each atom from the center of mass of the cluster. For an unsupported particle the center of mass is found to be the center of the cluster. The center of mass for a given cluster is calculated and the cluster is moved to a new reference position with respect to the relocation of the center of mass. Typically origin is used as the reference position. The distribution functions are found to form individual distribution functions around different distances of separation. These distances of separations correspond to the different shell radii for the icosahedron. For the case of the 0K icosahedron the distribution function around these distances are found to be a delta function suggesting no displacement within the shells. The width of the distribution function around each distance shows the extent of distortion in each shell of the cluster. The typical distortion observed is small for the unsupported particles. The initial distance of separation of the particle was varied during simulations to ensure the true equilibrium structure was obtained. The width of the distribution functions is found to be a function of temperature of equilibration. As the temperature gets closer to 0K we observe a very narrow distribution at the different radii whereas a very broad function is observed at higher temperatures.

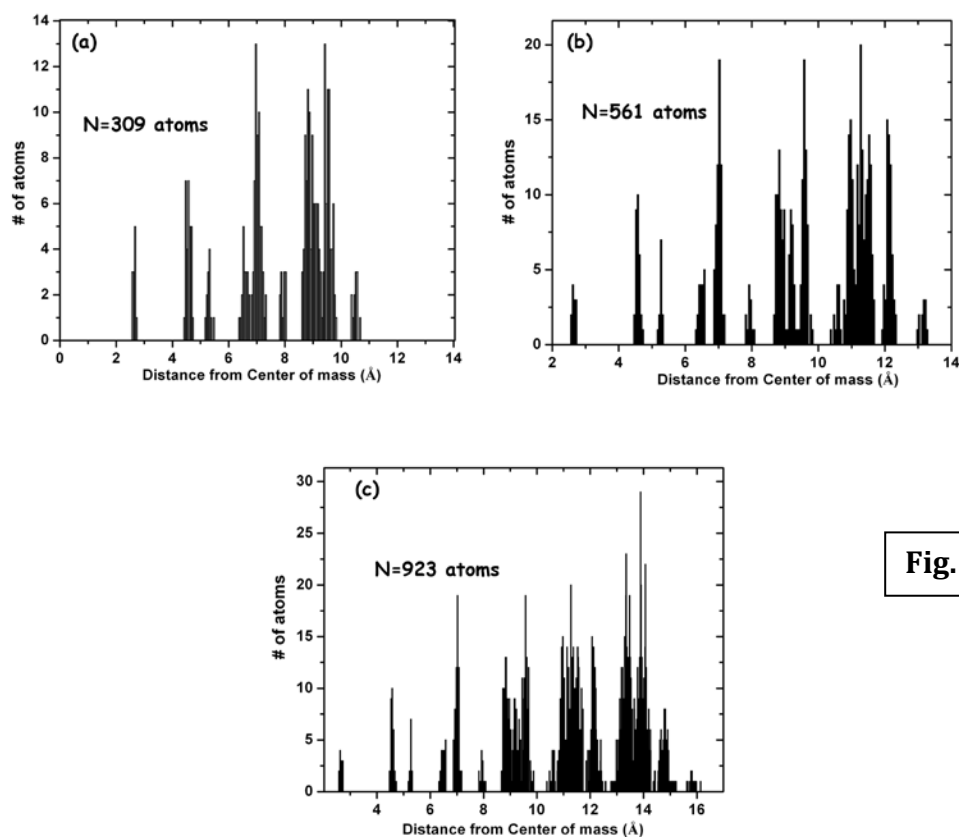


Fig. 7, 8, 9

Second order invariant bond orders are calculated for the unsupported particles. Figures (Figure MD12, 4, 5) shows the bond order plots for the core atoms of the unsupported particles for shells ⁵ and ⁶. The values of bond order parameters for the starting structure is also shown (straight line). The values of the bond order parameters are estimated for the shell below the outermost shell since the outer shell atoms do not have a complete neighborhood around them. The values of bond order parameter are found to lie in the same range as the 0K structure further proving the structure obtained for the unsupported nanoparticle from the simulations are closer to the starting the structure. Central atom (atom #1) exhibits the values of an icosahedral symmetry. The bond order parameter values for the atoms in the shell closest to the outer shell exhibit slightly higher variation than those in the inner core shells. This suggests that the atoms in the inner core/bulk are more stabilized than the atoms closer to the surface. The effect of temperature on the radial distribution function and the bond order parameter values suggests

the structures are sensitive to the temperature. Structures obtained from the unsupported nanoparticle are used to analyze the deviations obtained in the structures of supported nanoparticles. Simulation results for the supported nanoparticles and the implications on the structure of the catalyst nanoparticle are discussed in the following sections.

3. Supported nanoparticles

Supported nanoparticles are of interest in PEM fuel cells. Electrocatalytic reactions of oxygen and hydrogen are strongly dependent on the structure of catalyst surface. Unlike a regular lattice, the supported nanoparticles have been identified as a mixture of different facets of crystal lattice [koper2003]. Molecular quantum mechanics models have been developed for studying the catalytic properties of fuel cell catalyst materials. Ordered structures such as (111),(100),(110) are typically used for this purpose [zambelli1996],[curulla1999],[henry1998],[markovic2000]. Recently reports of structures with edges and kinks on the surface have been considered for these calculations. The actual nanoparticle structure of the catalyst particle has been very difficult to predict. Typical shapes of unsupported nanoparticles have been reported in the literature as icosahedrons and cuboctahedrons [HRTEM1]. However these structures are seldom observed in the real supported catalyst systems. Supported catalyst simulations involve using a hybrid boundary condition to study the adsorption of the platinum cluster on the surface of the support. Starting structures for the cluster was setup similar to the unsupported particle case. The temperature of the particle was maintained constant at 300K. The simulation times were varied from $5ns - 20ns$. Different particle sizes were used for the simulation purposes. 0K clusters are used as starting structures. Clusters are placed at an arbitrary distance from the xy plane corresponding to the support. At the end of simulations the supported catalyst structures are formed wherein the cluster is found to be at or near the equilibrium distance of separation between the nanoparticle and the support.

Particle size and the interaction energy are found to significantly affect the final structure of the supported catalyst particle. From figure (Figure MD2), the energy of interaction can be found to be a non linear function of the particle size. The energy of interaction is used as the binding energy between the nanoparticle and support. Support is found to influence all the atoms in the cluster as a function of the distance of separation between the atoms and the support. Atoms closer to the support interact stronger than the atoms farther away from the support. For really small particles, such as $n = 1 - 2$ shells the equilibrium structure of the particles resembles that of the unsupported particles. Also the relative position of the cluster was found to be independent of the support. This suggests that the particles with lower shell numbers are not sufficiently bound to the support leading to the desorption of the particles. Initial position of the cluster with respect to the support was varied in order to be able to validate the hypothesis of desorption of particles. Final positions of the particles were found to be far from the equilibrium separation distance for the Pt-C interaction further proving the inability of the support to trap the nanoparticle. One of the common concerns with PEMFC catalysts is the durability of the catalyst particles. Particle size distribution tends to shift towards larger particles during the operation of fuel cells [Borup2007], [kolde1995]. Recently observations of small platinum nanoparticles and bands of platinum in the membrane of the membrane electrode assembly have been reported [more2005]. The inability of trapping of the smaller nanoparticles by the substrate could help explain the loss of small nanoparticles from the substrate. Considerations of the effect of medium and electrostatic potentials are necessary in order to understand this phenomenon better. Ostwald ripening has been suggested as a possible mechanism for the growth of the particles. This process involves decrease in the size of smaller particles leading to the increase in the size of the larger particle leading to formation of small enough particles which may desorb from the surface of the carbon support leading to loss in utilization and increase in particle size distribution.

Figure MD10 shows the structures observed for supported nanoparticle clusters as a function of particle size/number of shells. Structures for shells 4,5,6

are presented. Images are assumed to be projections of the actual particle along the xy plane. The lower portion of the particle represents the portion of the cluster attached/adsorbed on the support. Unlike the case of unsupported nanoparticles the structures are found to be distorted from the 0K starting structure. Interaction between support and nanoparticle is also found to cause spreading of the catalyst particle closer to the substrate as seen by the flatness of the face of the nanoparticle. However the particle far from the surface is found to possess the five fold symmetry corresponding to the 0K icosahedral structure. This suggests that the interaction effect is interfacial between the nanoparticle and support and the bulk of the particle away from the support still preserves its characteristic structures. Localized modification of the structure of the nanoparticle also suggests the interaction forces are weaker in nature.

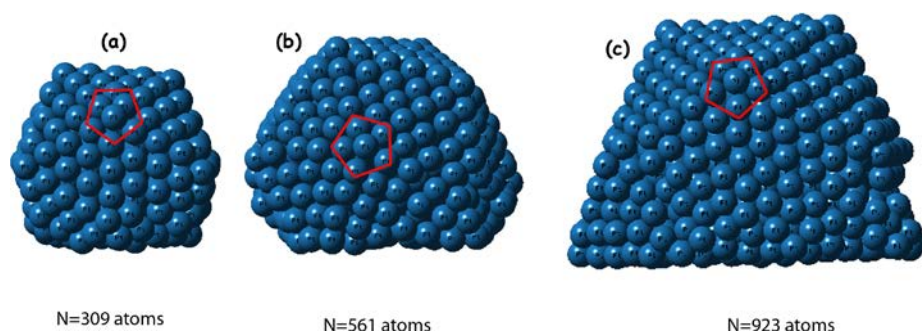


Fig. 10 Effect of Support

Radial distribution functions for the supported nanoparticles are shown in Figure MD11. Distances of atoms are estimated from the center of mass of the particle. The asymmetry in the structure of the cluster leads to the shift of center of mass of the cluster from the central atom. From figure MD11 the radial distribution function is seen to be more diffuse compared to the corresponding distribution functions obtained for the unsupported particle. This suggests the local neighborhoods and local shells of the particle are affected by the presence of the substrate. For smaller particles Figure MD11 (a) and (b) the distribution function shows deviation from the shell structure even at lower distance of separation from the center of mass. The extent of influence of the support on the nanoparticle cluster

could be understood from the deviations observed for the inner shells. Larger particles are found to exhibit smaller deviations for the inner/core shells than the smaller particles. As the particle size increases, the size of the region of influence between the support and nanoparticle decreases leading to smaller distortions in the inner shell. Local bond order parameters can also be used to understand the interfacial nature of the support-nanoparticle interactions.

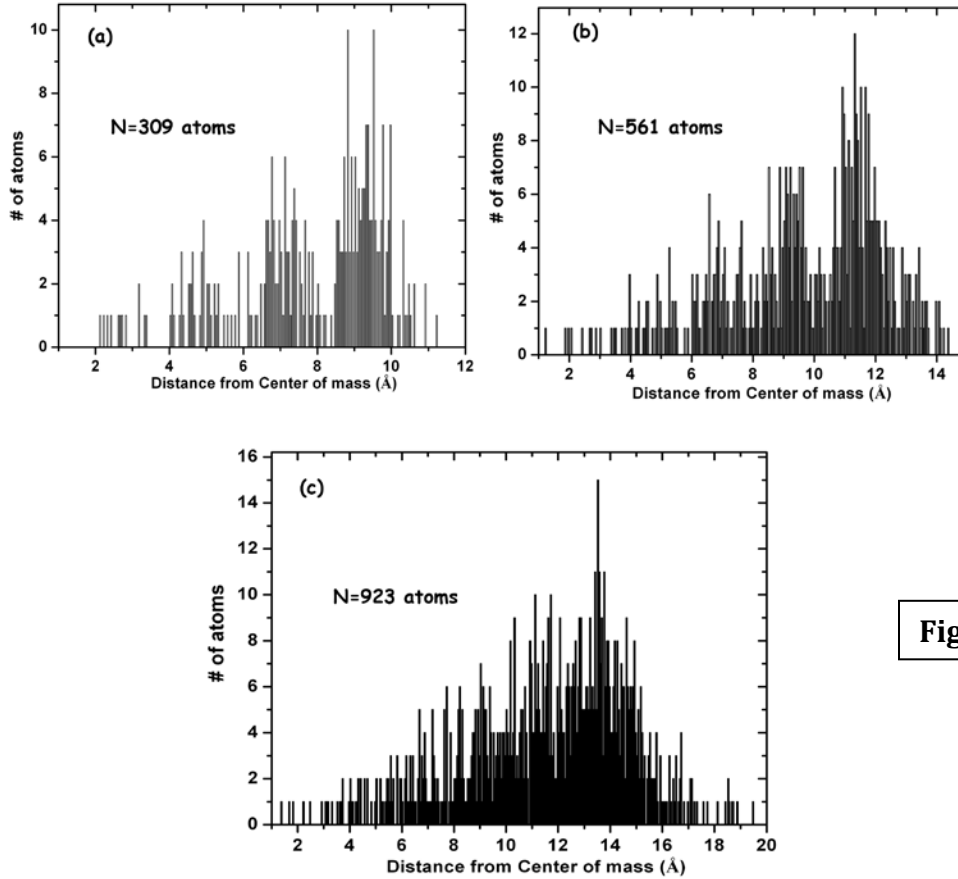


Fig. 11 a, b, c.

Second order invariant bond orders are calculated for the unsupported particles. Figure MD12 shows the bond order plots for the core atoms of the supported particles for shells ⁵ and ⁶. The values of q_6 and q_4 are found to vary significantly from that exhibited at 0K structure. A closer analysis of the values suggest that the local parameters still lie within the range of fcc and hcp symmetries suggesting the overall structure order for the inner cluster is still preserved. The central atom (atom #1) is found to exist in the icosahedral core proving that the

inner core of the particle is affected minimally by the presence of the support.

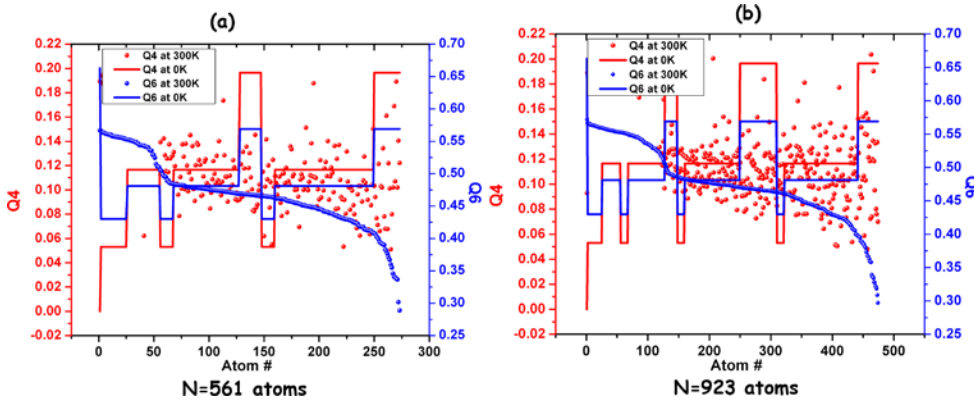


Fig. 12 a, b

Further analysis of the supported catalyst structure is necessary in order to understand the complete effect of the presence of the support. In order to quantify the effect of support on the structure/property of the supported catalyst the following three properties were considered: (a) Strain/atom for the particle, (b) geometric utilization and (c) the surface fraction of atoms. Effect of the support on these properties is discussed in the following sections.

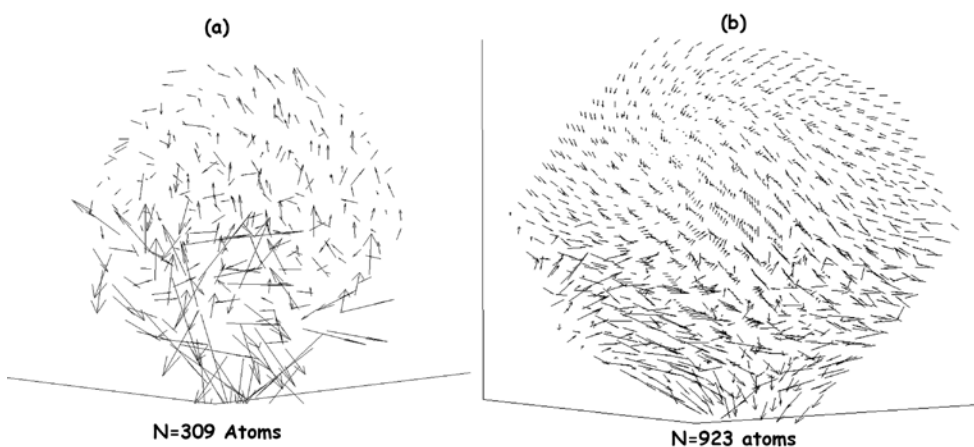
a. Strain field

Interaction between the support and the nanoparticle leads to displacement of atoms from the icosahedral shells. Strain field calculations reveal the extent of displacement of atoms due to this interaction. Strain field for supported calculated particles are calculated. The center of mass for the supported and unsupported catalyst particles are moved to $\langle 000 \rangle$. Atoms in the particle are displaced with respect to the center of mass such that both supported and unsupported particle have a common axes of reference. Strain per unit atom is then estimated as a difference between the position vectors for atom i between the supported and unsupported or free cluster.

$$\overrightarrow{Strain} = \overrightarrow{r_i^{Supported}} - \overrightarrow{r_i^{free}}$$

Where \vec{r} refers to the vector denoting the location of the atom. The vector field is then plotted using “quiver 3” function in Matlab®. Strain field plots for the three particle sizes chosen are shown in figure (Figure MD13). Strain field corresponding to two particles are shown.

Figure MD13:(a) corresponds to strain field observed for a particle of 4 shells (corresponding to 309 atoms) and 13(b) - 6 shells (923 atoms).



The magnitude of the vector is represented by the length of the vector. Higher displacements are represented by longer vectors. Two main observations are made. Larger displacements are observed at the support-nanoparticle interface. This is represented by the lower portion of the plot in the figures. Vectors are found to be a larger magnitude compared to the bulk of the particle suggesting a strong interfacial effect. Comparison of strain field between the small and larger particle indicates the displacement vectors decrease in magnitude moving away from the interface significantly for the case of the larger particle. This indicates a weaker displacement of the atoms in the bulk of the particle. The decrease in magnitude is more prominent for the larger particle compared to the smaller particle further suggesting the interaction is short range between the support and nanoparticle. A long range interaction would ensure the displacement vectors being uniform throughout the particle. One of the main conclusion that can be drawn from the strain field maps is the structure of the nanoparticle is a bit more strained at the interface of the support and nanoparticle and the strain relaxes moving through the bulk of the particle away from the support interface.

b. Surface to volume ratio

One of the main advantages of using supported nanocatalysts over bulk catalysts is the increased surface to volume ratios for the nanoparticles. Surface to volume ratio increases with decreasing particle sizes. A higher surface to volume ratio leads to better activity per unit weight of the catalyst material. The number of surface and core atoms for the nanoparticle clusters are calculated. The distinction between core and non-core or surface atoms is made based on the number of nearest neighbors for each atom. Core atoms are assumed to behave similar to an atom in the bulk of a metal therefore corresponds to atoms with twelve nearest neighbors. The sphere of nearest neighbors for each atom is assumed to have a cutoff radius based on the Sutton-Chen lattice parameter. This value was identified to be 3.05 \AA . This corresponds to a value of $\sim 75\%$ of the Sutton-Chen lattice parameter. Surface or non core atoms are counted as those atoms with $N_{\text{neighbors}} < 9$. The distribution of neighborhoods is shown in figure (Figure MD14). The distribution of neighborhoods for unsupported catalyst is also shown. Neighborhood includes the atom of interest. Therefore the core neighborhood consists of 13 atoms at the minimum.

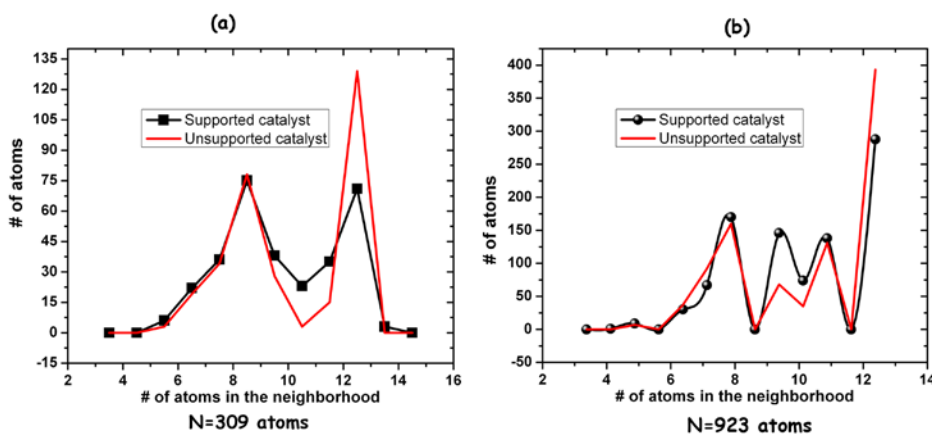
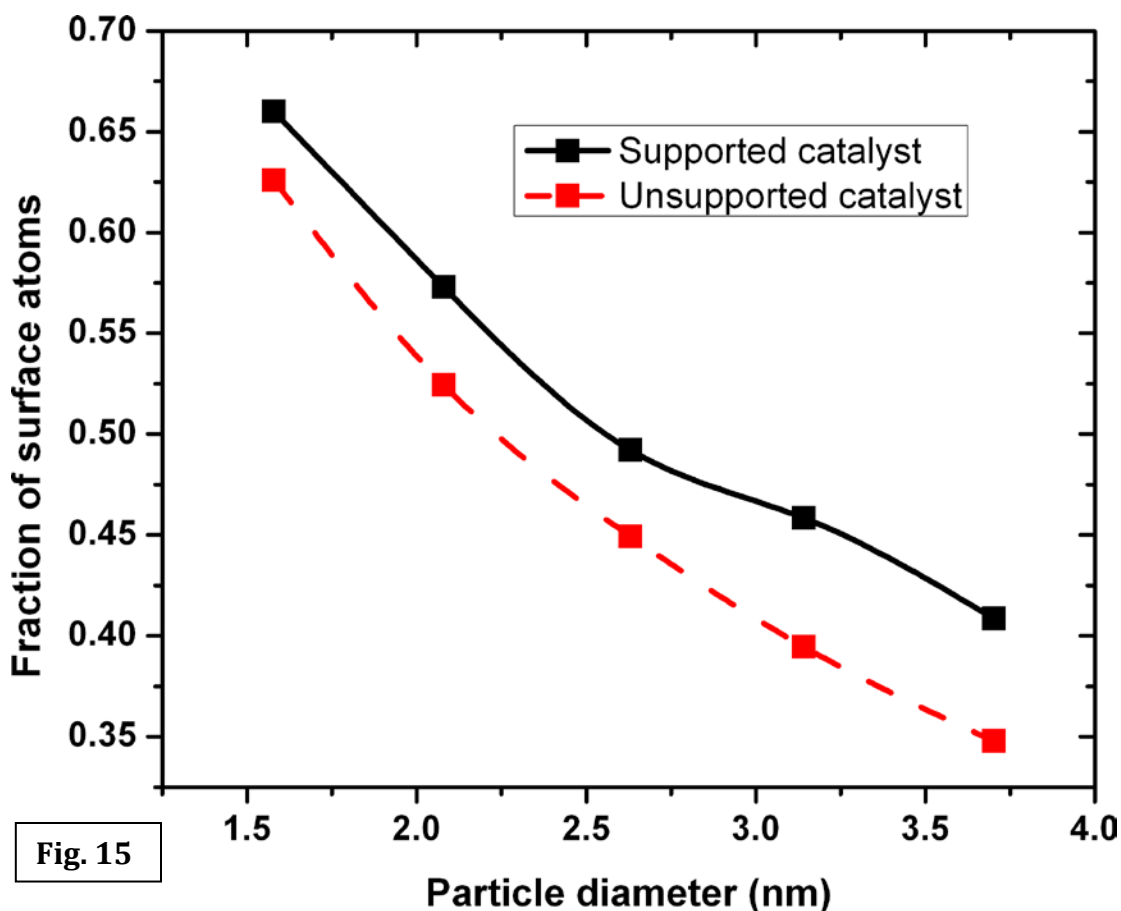


Fig. 14 a,b

Atom shells are slightly rearranged for unsupported nanoparticle. As a result we observe some different neighborhood patterns at the lower range for the atoms in these particles. For a 0K particle the only neighborhoods that are active are 6,9,10 and 12. For the unsupported particle due to the displacement of surface atoms we

observe some smaller neighborhoods such as 4,5 and 6. Supported particles exhibit a continuous distribution of neighborhoods. The number of neighborhoods with 12 atoms is lower than that for the unsupported nanoparticle suggesting the distortion of the particle structure whereby the bulk atoms are displaced. Also there is a significant increase in the number of non core neighborhoods for atoms in the supported catalyst particle. This leads to an increase in number of surface atoms for reaction.

Ratio of surface to core atoms for particles of different diameter is shown in figure MD15. The supported catalyst particle as expected has a higher fraction of surface atoms. The ratio of surface to core atoms decreases as a function of particle size due to the increase in bulk atoms. Higher fraction of surface atoms observed does not necessarily mean a better performance. This calculation does not take into account of the atoms in the cluster that lie in the interface between the support and the nanoparticle. These atoms are inactive during the reaction. Hence this fraction needs to be corrected for geometric area loss in the particle.

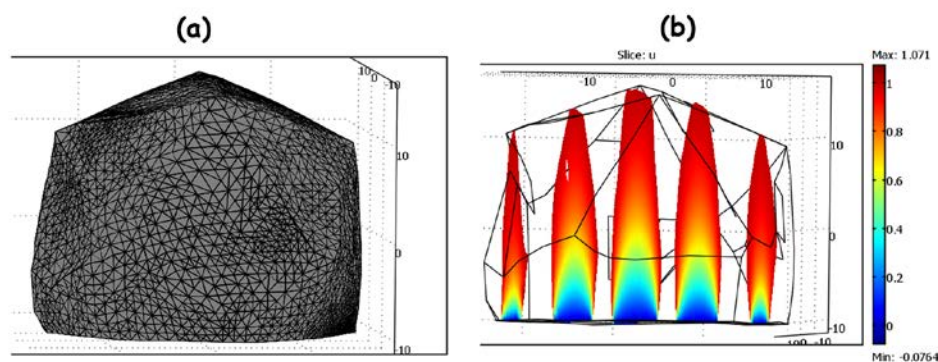


The intrinsic catalytic activity for the catalyst particles is assumed to be unity for these calculations. A strained structure may possibly lead to defects in the structure of the particle thereby increasing the activity of the catalyst. However a detailed quantum mechanical calculation is necessary in order to better understand this property. Geometric area of the catalyst available for the reaction is very important parameter that needs to be estimated to quantify the utilization of the catalyst particles. Loss in geometric utilization happens to the presence of catalytic atoms buried between the nanoparticle and the support at the interface. Geometric utilization of particles based on the simulated structures of supported catalysts is calculated in the following section.

c. Geometric utilization

Geometric area of the particles available for catalytic reactions is significant to understand the utilization of the catalysts. Geometric utilization can be defined as

the ratio of actual geometric area available for reaction compared to the total geometric area. Geometric utilizations were estimated for the supported catalyst particles using COMSOL finite element method. In order to estimate the geometric utilization, a mesh object was created from the locations of the outer shell atoms of the particles. The mesh object was then converted to a 3d object for estimating the area available. A model system was setup to estimate the surface area of the particle. The portion of the catalyst particle exposed to the support (bottom face of the catalyst particle) was considered inactive for reaction due to the lack of gas access. Model object was designed such that there is very little difference between the inner surface area and outer surface area. The walls of the object are considered thin enough to validate this approximation. A typical mesh and concentration profile for the solution are shown in figure MD16.



Mesh for N=931 atoms

Fig. 16 a, b

In order to model the reaction on the outer surface of the catalyst particle, an embedded geometry needs to be constructed. The particle would need to be placed inside a box which represents the bulk. Mesh integrity issues arose when trying to embed the 3d mesh object representing the catalyst particle into a domain representing the bulk. In order to overcome this issue the model system was inverted. For the inverted model system, an infinite source was assumed to be present at the center of the particle. By applying suitable Dirichlet boundary conditions wherein the active surface had a unity concentration and inactive surface had a zero concentration, the surface area of active region is estimated. Surface area was estimated based on integrating the concentrations on the reactive vs. inactive

surfaces for both unsupported and supported nanoparticles. Unsupported particles have no inactive regions. The model system used is described below.

$$\text{Subdomain : } \nabla^2 c = 0$$

$$\text{boundaryconditions : reactive : } c = 1, D = 1 \times 10^{-6} \text{ m}^2/\text{s}; \text{insulating : } c = 0$$

As can be observed in figure (Figure MD16) the concentrations closer to the support nanoparticle interface represent a diffusion layer of zero concentration. Therefore by summing the concentration values on the reactive surface we obtain a flux based surface area for the catalyst. If all the boundaries are assumed to be reactive we can obtain a theoretical maximum for the catalyst active surface area. Knowledge of the maximum and actual surface area helps us to estimate the geometric utilization of the catalyst particle.

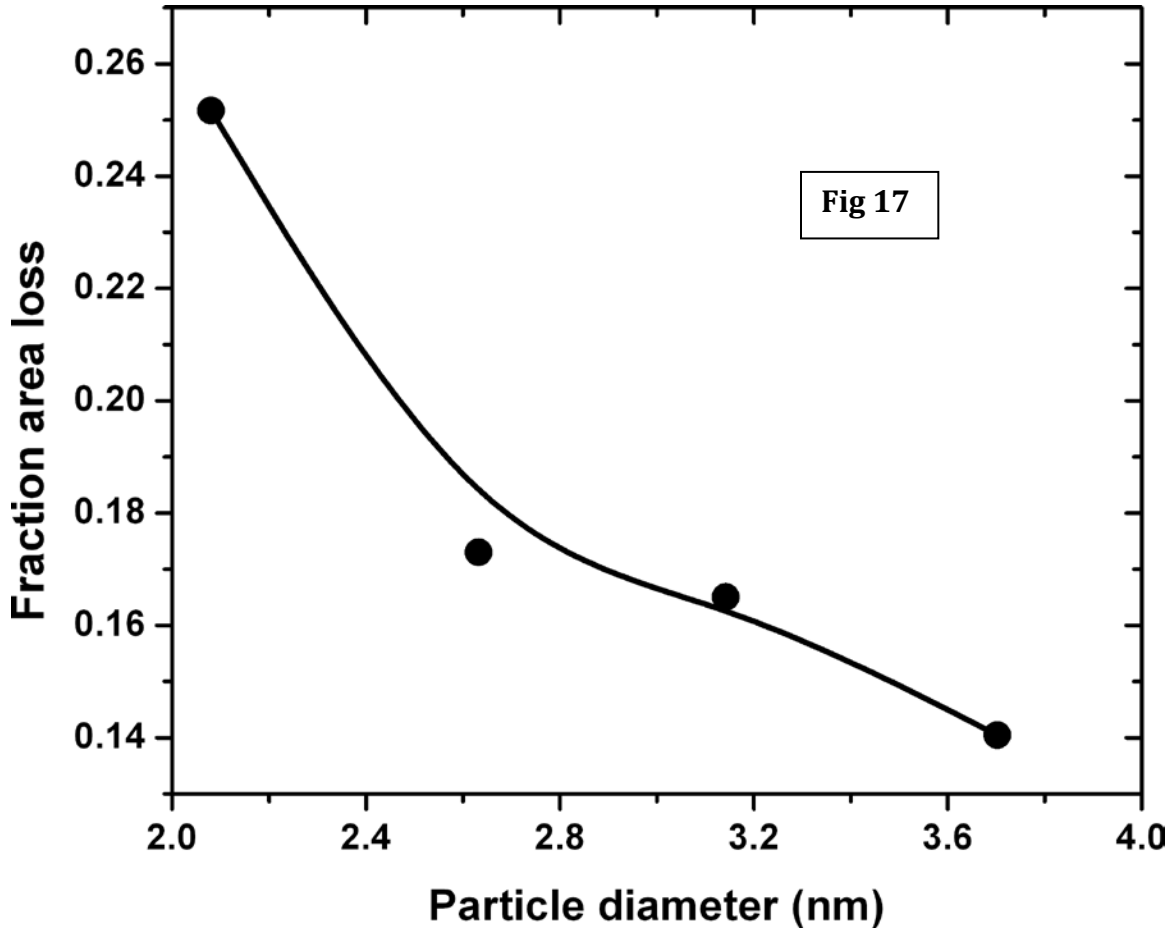


Figure MD17 shows the variation of utilization for particles of different sizes. The utilization shows a decrease with increase in particle size due to the decrease in the

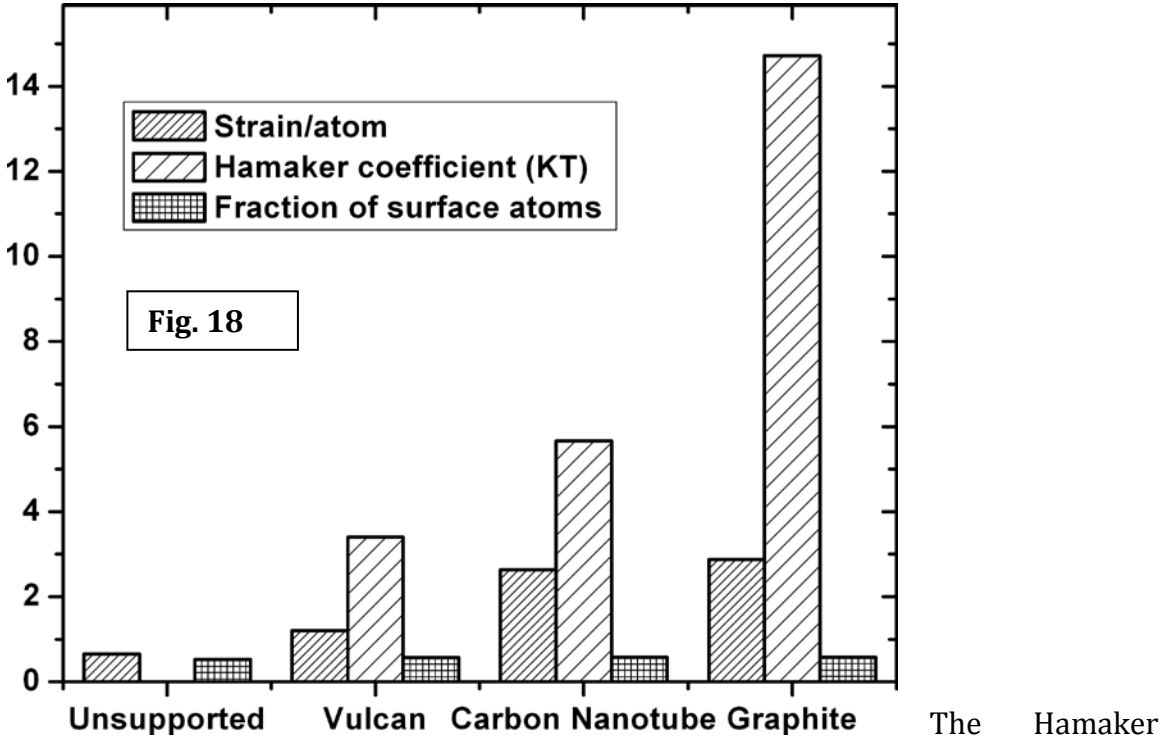
amount of surface area exposed to the support for the particles. Higher utilizations are necessary suggesting use of larger particles compared to very small particles. However a balance is needed when choosing the optimum particle size based on the geometric utilization and utilization per unit weight. A particle size which provides a high utilization per unit weight is ideal for fuel cell applications. Also the intrinsic catalytic activity of the particle as a function of particle size is necessary for choosing the optimum particle size for fuel cell applications.

A better calculation would be to use the particle to model the reaction kinetics for a typical fuel cell reaction. This would need the particle to be embedded in a box simulating the bulk conditions for the gas interface. However this problem gets complicated because of the mesh integrity issues as described above. Further investigation on methods to model the particle is currently underway.

4. Effect of support nature

Amorphous carbons such as carbon black and activated carbon (AC) have been the traditional supports used in heterogeneous catalysis. For activated carbons, the porous topology leads to large internal surface areas per unit weight [kinoshita1990]. These high surface area activated carbons potentially offer more sites for catalyst deposition than other varieties of carbon. Graphitic carbon varieties discovered in recent years such as carbon nanofibers (CNF) and carbon nanotubes (CNT) possess excellent electrical conductivity, a characteristic vital to electron transport within a fuel cell. Additionally, carbon nanofibers and nanotubes potentially offer significant advantages over traditional supports, namely an impurity free surface (devoid of catalyst poisons such as sulfur) and resistance to corrosion [serp2003]. These inherent advantages have encouraged several researchers to investigate platinum deposition on fibrous supports such as nanotubes and nanofibers [lordi2001], [Yu1998] and [abhi1]. Recent reports of carbon durability issues due to carbon corrosion have led researchers to focus on graphitized support due to their high resistance to carbon corrosion. One of important property to be considered before the use of new carbons as carbon supports is their effect on the nanoparticle structures. Nanoparticle structures as discussed in the above section are dependent on the interaction with the carbon

support. In order to estimate the effect of varying the carbon support, simulations were carried out for three different types of commercial carbons.



The Hamaker coefficients for Carbon nanotubes and graphite are available in literature [rajter2007]. Hamaker coefficients for interaction between platinum nanoparticles and the carbon support were estimated using a combination rule [jacob1991] given by,

$$A_{mn} = \sqrt{A_m A_n}$$

Support	Strain/atom	Hamaker Coefficient (kT)	Fraction of surface atoms
Unsupported	0.653	0	0.5243
Vulcan XC72	1.209	3.4	0.5728
Carbon Nanotube	2.631	5.665	0.5793
Graphite	2.876	14.724	0.5825

Strain per unit atom for supported catalyst particles were estimated using the following equation

$$\frac{Strain}{atom} = \frac{\left\{ \sum_{i=1}^N \left\| \left(\vec{r}_i^{Supp} - \vec{r}_i^{OK} \right) \right\|^2 \right\}^{1/2}}{N}$$

Figure MD18 shows the variation of strain per atom, Hamaker coefficient for interaction and fraction of surface atoms for the supported catalyst particles simulated using the three different types of carbon support. The data values are tabulated in table (Table MD3). The strain on the particle is found to be dependent on the magnitude of interaction of the particle. First glance at the strain data would suggest a highly spread structure for the carbon with highest Hamaker coefficient. However a closer look at the values of fraction of surface atoms suggests that the particle outer shell structures do not vary too much varying the nature of the support. A higher strained system does not necessarily lead to a higher surface atom fraction. This suggests that the variation is more internal and the internal structure of the platinum particle is different for the three different types of carbon. The variation of the core structure could lead to a variation in the reactivity of the catalysts further emphasizing the importance of understanding the interaction behavior between the carbon support and nanoparticle. This suggests that the internal structure of the catalyst particle on the supported is different for the different supports. This may lead to different catalytic activity on the particles on different supports. Quantum mechanical reactivity calculations are necessary in order to understand the increase or decrease of catalytic activity for the nanoparticle on changing the support.

5. Temperature effect

Molecular dynamics simulations of particles are strongly dependent on the temperature of the system. A higher temperature leads to higher energy atoms thereby leading to distorted structures for the catalyst clusters. For the case of supported catalyst particles, the binding energy between the nanoparticle and the

support may lead to lowering the vibration of the atoms on increasing the temperature. In order to understand the effect of temperature on the strain of the nanoparticles MD simulations were performed for platinum 4 shell cluster as a function of temperature. Temperatures of interest for the fuel cell catalysts are in the range of 330-400K. Particles were heated up from 0K to the temperature of interest and allowed to equilibrate at that temperature for 4ns.

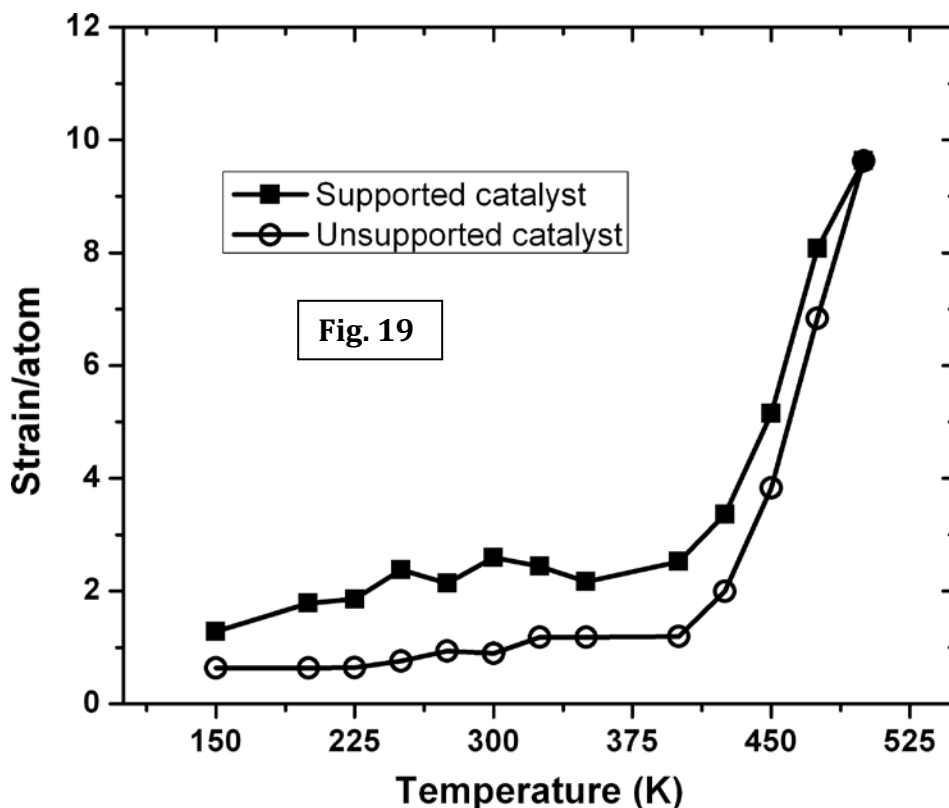


Figure 19 shows the variation of strain as a function of temperature. The supported catalyst particle has a higher strain at lower temperature arising from the interaction of the nanoparticle with the support. On increasing the temperature the kinetic energy of the atoms in the cluster increases which leads to further distortion in the structure of the nanoparticle. At higher temperatures above 425K the strain increases at a much higher rate than the lower temperatures. However the rate of increase of strain for the free nanoparticle was found to be much higher than the rate of increase of the supported nanoparticle. This can be explained based on the presence of binding energy between the support and the nanoparticle which prevents the free vibrational motion of the atoms leading to a restricted movement.

This experiment further gives us an insight into the effect of binding interaction between the support and nanoparticle and its effect in stabilizing the nanoparticle structures at higher temperatures. The calculations are extended to alloy nanoparticles by using the mixing rule. The temperature stability of nanoparticle structure is significant in the case of alloy nanoparticles in order to avoid phase segregation of material. Simulations of alloy nanoparticles are presented in the following section where the temperature effect on supported vs. unsupported alloy nanoparticle is discussed.

6. Alloy nanoparticles

Alloys of platinum and transition metals are commonly used in PEM fuel cells as alternative to platinum nanoparticles [stonehart1990], [stamenkovic22005]. Alloy nanoparticle provide various advantages such as lowering the amount of platinum needed, increased stability of the catalyst, increased resistance to poisons such as carbon monoxide and comparable activities. Both binary and ternary metal groups are being used as catalysts for PEM fuel cell applications. The nature of alloy nanoparticles influences the interaction energy between support and nanoparticle. Energies for alloy nanoparticles were estimated for commonly used alloy nanoparticles from measuring their optical spectra [ram1]. Alloy nanoparticles considered mainly for our simulations are Pt₃Co, Pt₃Cu, Pt₃Fe and Pt₃Au. The values of interaction energies were not available for PtFe, PtCu and PtAu materials. For this purpose approximation of the energy of interaction was made based on the energies of PtCo and PtRu. The average of PtCo and PtRu were used as the interaction energy for the alloy materials. Interaction energy of alloy nanoparticles was found to be slightly lower than that of platinum nanoparticles [ram1]. The initial structures for alloy nanoparticles were designed based on core-shell structures. The alloying element was considered to be in the core of the particle and platinum atoms on the shell of the particle. The number of atoms of alloying element and platinum were adjusted such that the composition was 1:3 for M:Pt where M=Co, Cu, Fe and Au. The composition was chosen based on the commercial material compositions. Icosahedron structures were assumed to be the

starting structures for these simulations. For the case of unsupported catalyst particles the core shell ordering was found to be preserved for the most extent during the simulation. The ordering and symmetry are observed to be preserved similar to the pure platinum unsupported nanoparticles. This could be because of the stabilization of the alloying elements in the core by the platinum shell atoms. The nature of alloying element plays a significant role in the stabilization of the core shell structure. For high surface energy metal atoms such as copper and iron the core shell structure gets disturbed during the simulation of unsupported nanoparticles.

Supported alloy nanoparticles exhibit different behavior based on the alloying elements. Figures (Fig. MD20a, b, c, d) show the structures of PtCu, PtFe and PtCo, PtAu respectively. The overall structure of the nanoparticle resembles that observed for the supported platinum nanoparticles except for the case of PtFe alloy particles. Higher numbers of core alloying elements are observed on the outer surface of the particle than that for the case of unsupported nanoparticles. This could be explained as a dual effect due to the substrate. The interaction of whole particle leads to distortion of the overall structure of the particle. Strain on the structure leads to modification of interaction between the core elements and shell elements leading to the migration of the atoms to the surface. Also the spreading of the particle leads to the exposure of core atoms to the surface thereby increasing the number of alloying elements found on the surface. For PtFe catalyst particle, the structure of the catalyst is found to be more spread than for any other material. This may suggest Pt₃Fe structures are not favorable for a core shell arrangement. Also the interaction energies used for these calculations are approximate further suggesting a possibility of overestimation of the interaction energies leading to a unique structure. Further investigation is necessary in order to quantify the effect of alloying elements on the overall structure of the nanoparticles.

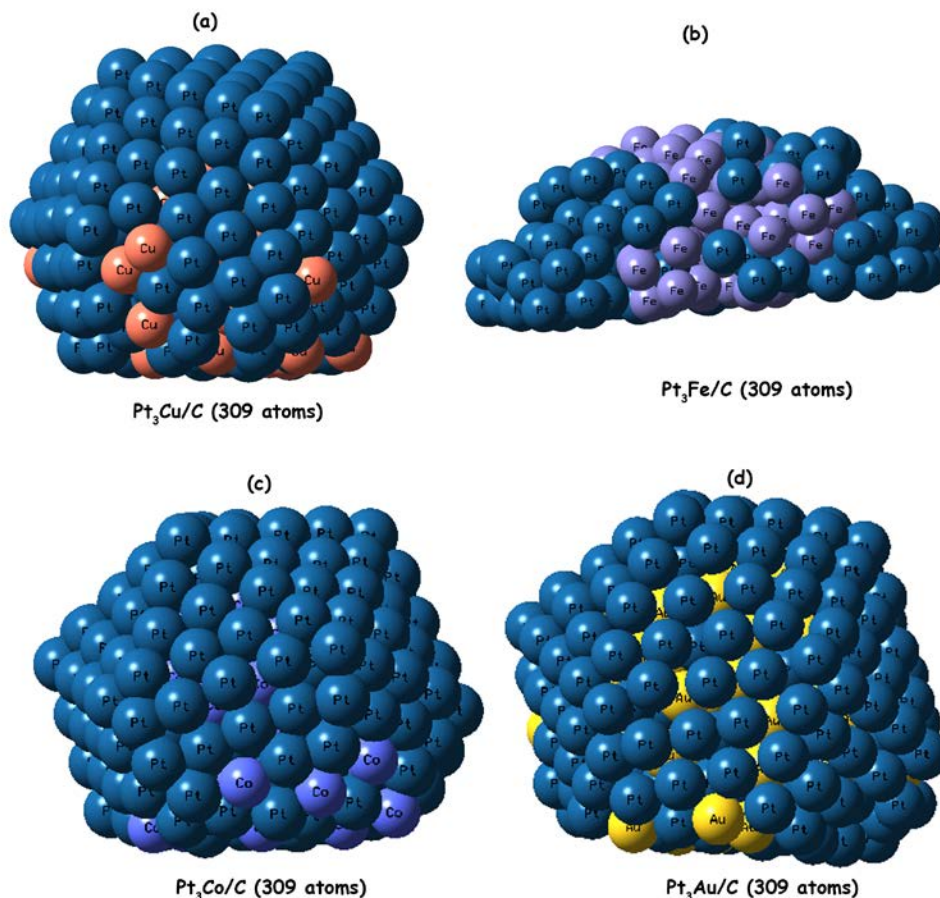


Fig. 20 a, b, c, d

The presence of alloying element on surface leads to two significant effects on the nature of the catalyst. The number of non-core platinum atoms decreases with alloying of the nanoparticles. Also the inter platinum distance on the surface is affected by the presence of alloying element. This may lead to roughening of catalyst particles. Recent results [Strasser1],[strasser2] of PtCu alloy nanoparticles indicate an increased activity per unit weight of the catalyst on electrochemical dealloying of the copper from the alloy nanoparticle. This could be a result of increased roughness on the surface of the nanoparticle. In order to understand the roughness effect better distance of separation between platinum atoms on the outer surface is calculated. Figure MD21 shows the distribution function for Pt-Pt distance on the outer surface for alloyed nanoparticle (in this case Pt_3Cu after removal of copper atoms) and that for the unalloyed nanoparticles (supported platinum nanoparticles).

The Pt-Pt distance distribution function for the alloyed nanoparticle indicates a shift in distribution of Pt-Pt bond distances towards shorter lengths for the dealloyed nanoparticle. This could be a possible explanation for the higher activity observed for PtCu nanoparticles with copper atoms stripped from the particle. Figure MD22 shows the variation of number of surface platinum atoms and strain per atom for the alloy nanoparticles. Alloying elements are arranged as a function of oxidative ability of the alloying elements. As expected increase in surface energy of alloying elements leads to increase of the number of alloying atoms on the surface of the nanoparticle. This explains the loss of platinum surface atoms moving from Au to Cu for the alloying elements. The strain per unit atom from equation (strainperatom1) for the particle shows that strain decreases with increase in surface activity of the alloying elements. The case of Pt₃Fe shows a much higher strain due to the complete destruction of the symmetry.

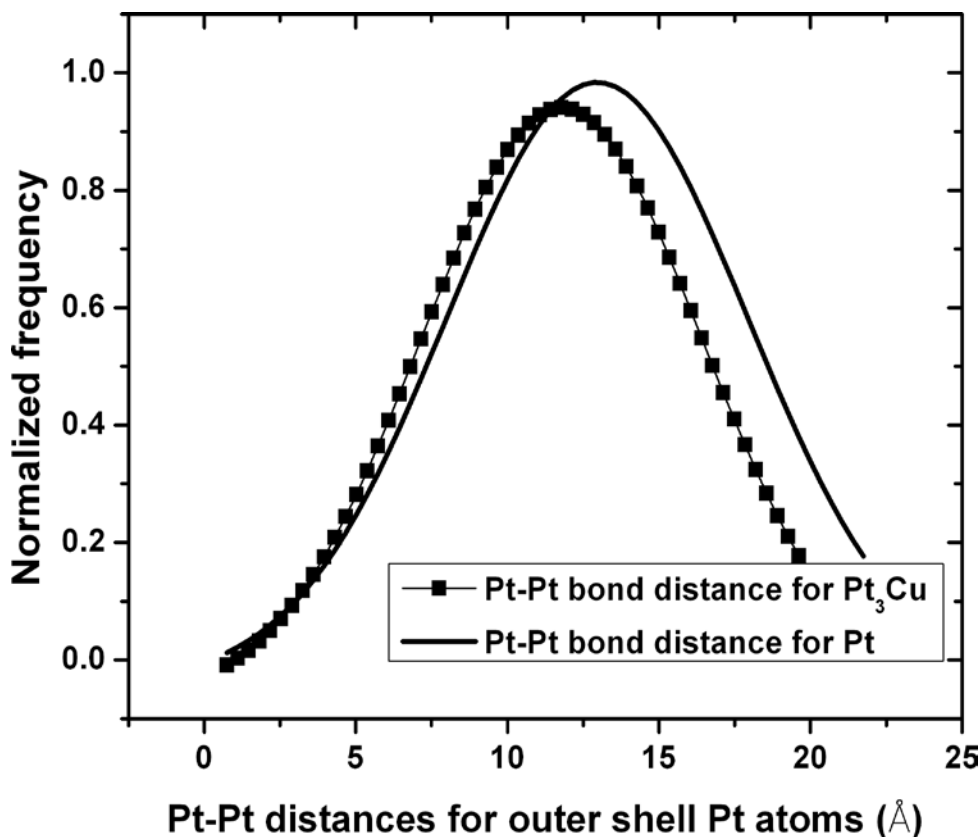


Fig. 21

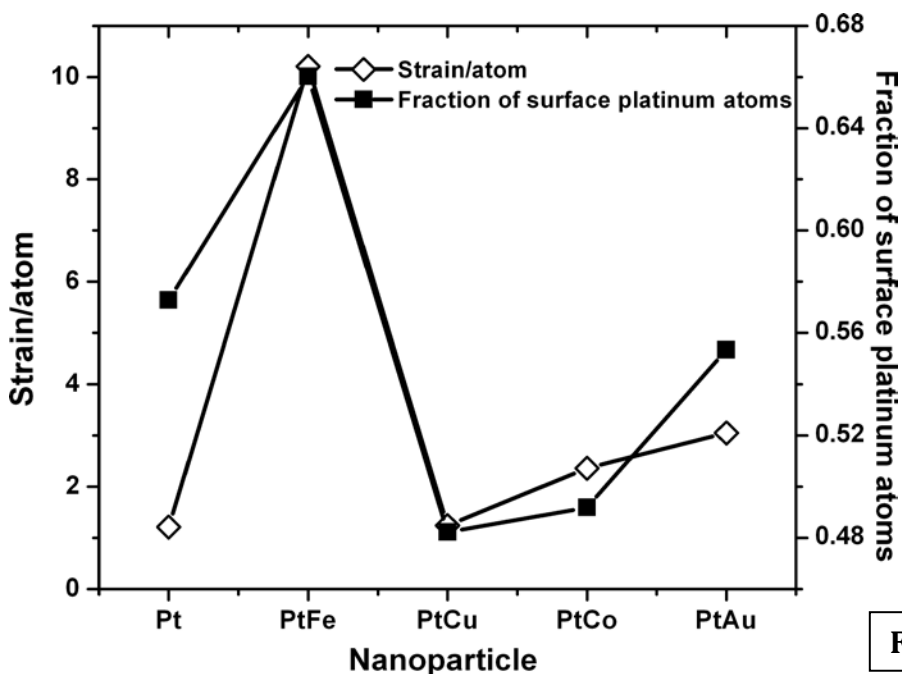
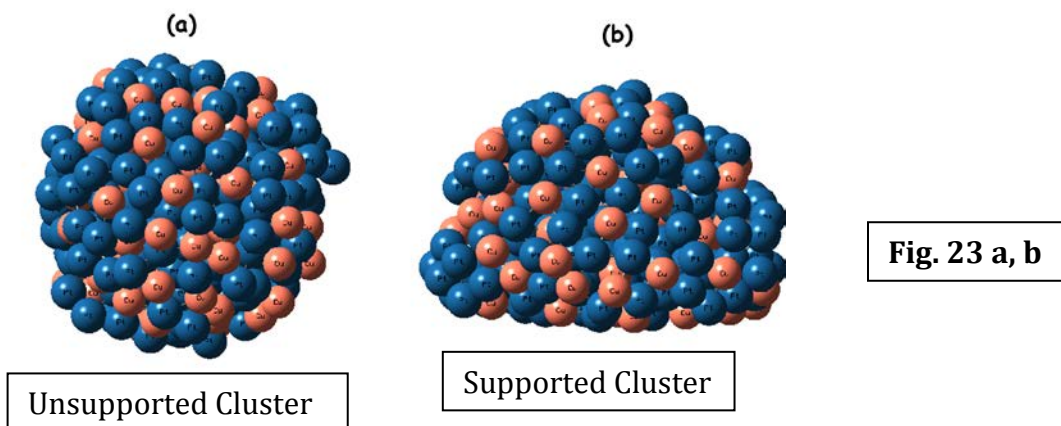


Fig. 22

Melting of unsupported nanoparticles was studied to understand if the alloy element core structure is disturbed at high temperatures. Figure MD23 a, b shows the comparison between Pt₃Cu alloy nanoparticles at 1000K. Comparing the structures initially suggests the number of core Cu atoms on the surface of the nanoparticle increases with increasing temperature. Strain per atom was estimated for the two structures with the 0K core-shell structure as the starting structure. The strain for the unsupported nanoparticle was found to be 10.05 whereas for the supported alloy nanoparticle the value was lower at 9.63. This suggests that the support leads to extra binding effect on the structure. Nature of core metal atom plays an important role in determining the extent to which the two metal atoms are dispersed in the final structure. Difference in mobilities and energy of interaction between the alloying elements would lead to difference in structures obtained. The main conclusion from this computer experiment is that the support exhibits a

stabilizing effect on the structure of nanoparticles at higher temperatures.



Ternary alloys are interesting for fuel cell applications. Recent reports of higher stability and reaction kinetics for ternary alloys have made them viable for PEM fuel cells [Strasser1], [strasser2]. One of the many advantages of computer simulations of structure is the ability to identify and design new metal alloy system. Phase segregation is a common problem in alloy nanoparticles. Phase dispersion of alloying elements is also a necessary property to be addressed. Two systems of ternary alloys were considered for our simulations. $\text{Pt}_{4.1}\text{Co}_{2.2}\text{Cu}$ and $\text{Pt}_{4.1}\text{Au}_{2.2}\text{Rh}$ were chosen for our studies.

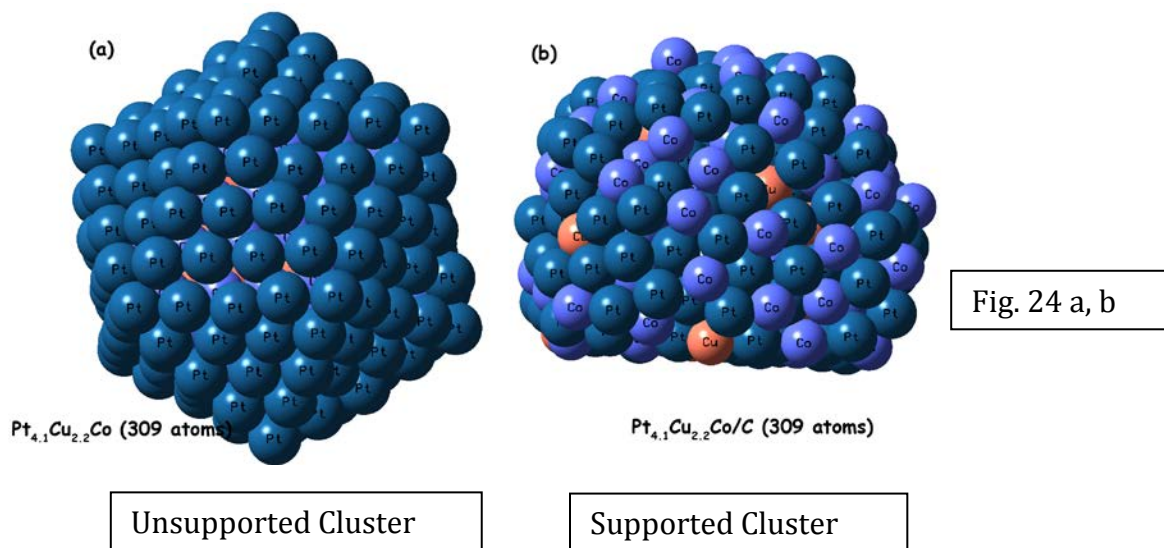
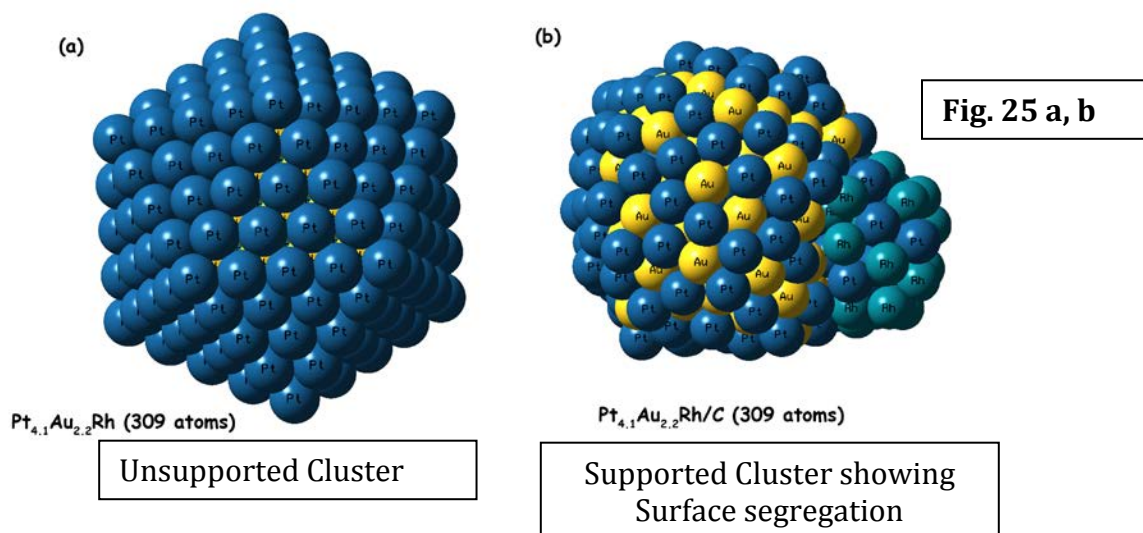


Figure MD24 a, b shows the comparison between unsupported and supported ternary alloy particle of PtCoCu. The interaction energy value of PtCo is used for the

simulations. The OK structure is developed as follows. Copper atoms are placed at the innermost core of the particle followed by a Co shell which is then surrounded by a platinum shell. The number of atoms in the core is adjusted in order to preserve the ratio of interest. The unsupported particles show very few alloying elements on the outer surface and some Cu and Co atoms switching shells between the two atom groups. However on inclusion of the effect of support a well dispersed system with Co and Cu atoms on the outer shell are observed. This could lead to formation of well mixed alloy nanoparticle. Mixing of alloying elements may lead to decrease in catalytic activity due to increased distance of separation between the platinum atoms. However mixing may also alter the local electron densities suggesting a modification of intrinsic catalytic activity of platinum atoms. A more detailed quantum mechanical calculation is necessary to understand this effect better. This result suggests the possibility of phase mixing of alloying elements due to the interaction with the support. This suggests a means to design phase mixed alloy system for fuel cell catalysis. Modification of composition or the carbon support could modify the interaction force thereby leading to better phase dispersion or prevention of phase dispersion. This opens up opportunities for further designs of new catalyst materials for fuel cell applications.



Another advantage of MD simulations is the ability to identify viable alloying materials and material compositions. PtAuRh alloy was used for this purpose Fig. MD 25 a, b. Rhodium metal due to its crystal structure is known to be a non mixable

metal atom with platinum and gold. Simulation of PtAuRh was carried out with similar starting structure as for that of PtCoCu system. The rhodium metal was placed in the innermost shell of the particle. However during simulation the Rh metal atoms are found to migrate to the outer shell of the particle forming a phase of predominantly rhodium metal atoms. This suggests that the alloy material comprising of PtAuRh is not suitable for a catalytic system. Thus MD simulations with accurate support-nanoparticle interaction energies could be used for computational testing of new materials for fuel cell catalysts. Refinement needs to be done to account for the actual energetics of the particle. Nonetheless the use of average interaction energies based on PtCo alloys should give us a qualitative tool for identifying the effect of the support. Quantum mechanical calculations will help in understanding the effect of these structures on the activity of the new catalyst materials. The simulations suggest that the support contributes strongly to the catalytic activity of the material other than being a support for dispersing the nanoparticles.

7. Trapping

During the simulation of supported nanocatalyst, the nanoparticle cluster is placed at an arbitrary distance away from the support. The interaction between the support and the nanoparticle acts as a driving force moving the particle cluster towards the support. Atom positions are tracked during the simulation. Figure MD26 shows the variation of position of an atom on the inner shell of the nanoparticle cluster with time. The motion along the z direction shows the effect of the substrate and the motion along the xy direction is a function of the temperature and interaction between platinum atoms. In an unsupported nanoparticle the particle motion with time can be compared to Brownian dynamics.

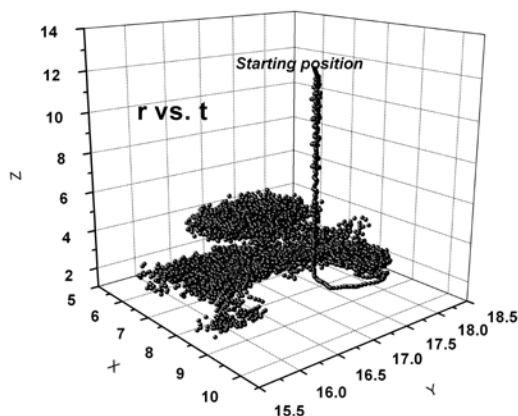


Fig. 26 Pt NanoParticle diffusing to the substrate surface.

Figure MD27 shows the comparison of motion along the xy plane and yz plane. The xy plane motion of the atom shows a random Brownian diffusion whereas the motion along the yz plane suggests a biased diffusion. The trapping of the particle on the substrate can be visualized from observing figure (Figure MD26, 27) which shows the location of atoms along the z direction for the atom. The movement of the atom shows there are two different kinds of mechanisms involved in the diffusion process. The first stage involves a rapid movement of the atom along the $-z$ direction suggesting a biased/directional diffusion of the cluster towards the support. The second process corresponds to an unbiased diffusion of the atoms along xyz directions constrained to the minimum energy distance between the particle and support. This process is still biased wherein the diffusion is restricted by the average distance of separation between the atoms and support however the atom does exhibit a Brownian type of diffusion along the xy plane. In order to better understand the diffusion mechanisms calculations were performed to identify the order of diffusion in these systems. For an unsupported nanocatalyst there is no biasing suggesting the atoms are following Brownian like diffusion.

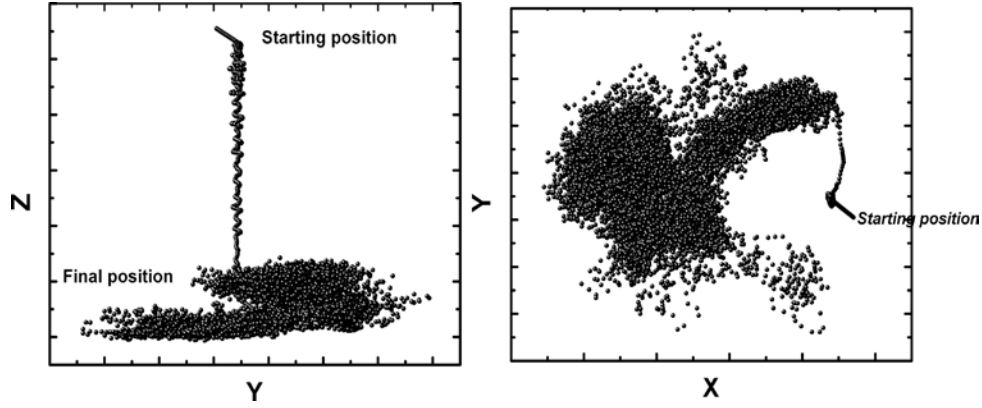


Fig. 27 Diffusion process of Pt on a smooth carbon like substrate

In order to understand the nature of diffusion of atoms for unsupported nanocluster, we provide a brief, ab ovo, review of *Lévy's* model for a self-similar non local hopping surface transport model that in other context was called anomalous diffusion. Long jumps in surface diffusion have been observed in a number of experimental situations [alphalevy2], [mann2001], [senft1995], [mruzik1981]. α - *Lévy* process can be described simply as a diffusion process with a fractional Laplacian operator. The formal definition of such an operator is

$$\Delta_{\alpha} \stackrel{def}{=} -(-\Delta)^{\alpha/2}$$

Where Δ is the usual second order differential operator, which is recovered when $\alpha = 2$. The effect of the operator is developed in Fourier space through

$$\hat{F}(\Delta_{\alpha} f)(\omega) = (|\omega|^2)^{\alpha/2} (\hat{F}(f))(\omega)$$

Where it is clear that $0 < \alpha \leq 2$. Brownian diffusion could be described as a special case of *Lévy* process where the order of the Laplacian is 2. A brief mathematical derivation of the *Lévy* diffusion process is shown below.

Consider a one dimensional Poisson process representing the diffusion of the platinum atoms. $X(t)$ represents the stochastic function which describes the position of the atom at any given t . At any time $t > 0$ the standard Poisson distribution for a jump process of unity step is expressed as,

$P\{X(t), t = k\} = \exp(-t) t^k / k!, k = 0, 1, 2, 3, \dots$ The Fourier transform of this function $\phi(u)$ (characteristic function) is given by,

$$\phi(u) = E e^{i u X(t)} = \exp(-t) \sum_{k=0}^{\infty} (e^{i u})^k \cdot \frac{t^k}{k!} = \exp[t(e^{i u} - 1)]$$

If the process can be considered as a composition of n independent simple Poisson processes, each with jump sizes a_1, a_2, \dots, a_n , respectively, The resulting stochastic function $X(t)$ has a Fourier transform of the form,

$$\phi(u) = E e^{i u X(t)} = \prod_{j=1}^n \exp(-t) \sum_{k=0}^{\infty} (e^{i u})^{a_j k} \cdot \frac{t^k}{k!} = \exp \left[t \sum_{j=1}^n (e^{i u a_j} - 1) \right]$$

If jumps sizes are continuously distributed, say with intensity $L(da)$, then the natural infinitesimal limiting procedure for the corresponding Lévy process, leads to the following representation of its Fourier transform:

$$\phi(u) = E e^{i u X(t)} = \exp \left[t \int_{-\infty}^{\infty} (e^{i u a} - 1) L(da) \right]$$

assuming that the time increments are stationary and independent in disjoint time intervals. Define ψ so that, $\phi(u) = \exp(-t\psi(u))$ with Image. The intensity measure $L(da)$ is called the Lévy measure of the process $X(t)$ [bertoin1996]. When the Lévy measure has power scaling, i.e., $L(da) = da/|a|^{\alpha+1}$, a simple calculation leads to the α -stable Fourier transform:

$$\phi(u) = e^{-c|u|^\alpha} \text{ and } \psi(u) = c|u|^\alpha, c > 0$$

and the corresponding α -stable Lévy process.

Table MD4: The variation of Alpha with neighbors.

Atom number	Number of M neighbors	Alpha values
56	9	1.625
147	6	1.85
309	2	1.95

Table MD5: Variation of Alpha for atom 56 with alloying atoms

Alloying element M	Alpha values
$M = Cu$	1.625
$M = Co$	1.925
$M = Au$	1.825

The displacement of atoms from its position with respect to the center of mass of the particle is recorded. $X(t)$ is then obtained by estimating the statistical distribution of the jump sizes in the displacement function. The bin size used in calculating the distribution corresponds to the step size for the Poisson process of interest. A cluster corresponding to 4 shells are considered for these calculations. The following atom positions are considered. Atoms corresponding to the innermost shell (#3), atoms in the second shell (#63,81), atoms in the outer vertices (#152,153,179,198) and outer facets of the particle (#158,278) are considered. These atoms are chosen in order to distinguish the effects of the atom position on their diffusion coefficients. The algorithm used for the calculation of the values of α is described in Appendix 1. The calculation involves transforming the data into inverse Fourier space where the data was fit to the characteristic function in the inverse Fourier space using non linear least squares. The values of σ and α for each of the characteristic functions are then estimated by identifying the minimum error in the fitting function. The Fourier space calculations aid in avoiding dealing with the partial Laplacian operator in the real space. Figure MD28 shows the alpha

values estimated for the stochastic variables for the various atom locations for a set of supported and unsupported nanoparticles.

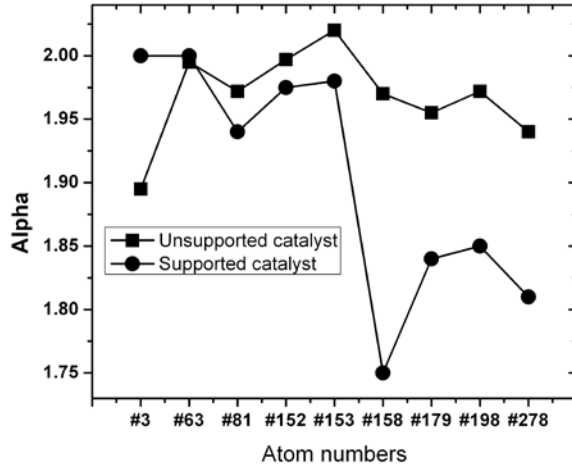


Fig. 28

The alpha values for unsupported particles are found to lie within 1.96 ± 0.04 . The atoms on the outer shell exhibit only slightly lower order of diffusion. This suggests that the diffusion of atoms in this case exhibits a Brownian type diffusion process. This is expected since the periodic boundary conditions ensure the interaction energies are symmetric through the whole particle and the only driving force for the diffusion process is based on temperature which typically exhibits a Brownian dynamics. Nature of the stochastic function $X(t)$ determines the order of diffusion process.

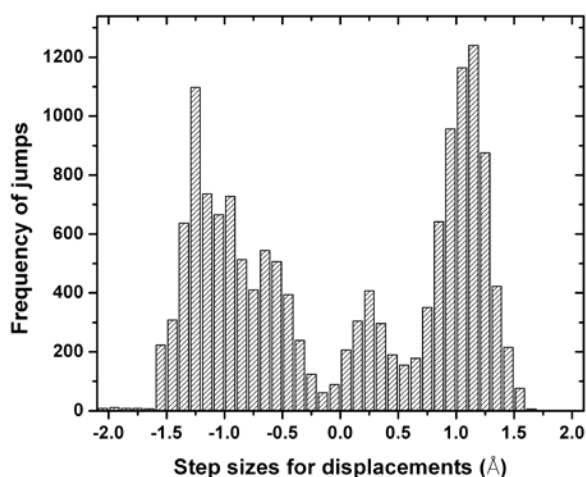


Fig. 29

From Figure MD29 we can observe that the displacement function for the case of the supported particle exhibits a multimodal distribution of step sizes. This can be explained as a consequence of the multiple mechanism of diffusion of the atoms described earlier. The values of α are calculated for the second part of the stochastic function. The second part of the distribution corresponds to the diffusion of atoms after the particle reaches the equilibrium distance of separation between the support and the nano-particle corresponding to minimum energy of interaction. α values are found to be in the range of 1.91 ± 0.08 . This suggests that the diffusion process at the equilibrium separation is similar to that of a Brownian dynamics. The atom closest to the support (#158, fig 28) exhibits a much lower order than the inner core atoms suggesting the effect of substrate prevents the free motion of the atom. A more rigorous model needs to be developed to describe the diffusion of the atoms to the support to account for the multimodal distribution function.

For alloy nanoparticles the order of diffusion could be used to understand the nature of interaction between the alloying elements. Tables (Table MD4 and Table MD5) show the values of α for a platinum atom in the particle as a function of atom position and number of alloying element neighbors for a supported alloy nanoparticle. Three atoms were chosen based on the number of alloying element

neighbors. The position of the atoms was varied between the shells of the particle. The atoms were chosen from each of the shells of the particle. Comparison of α values between the platinum atoms with varying alloying element neighborhood shows a decrease in order of diffusion with increasing alloy element. The lowering of the diffusion order is possibly due to the restriction of the atom movement due to the interaction potential between platinum and the alloying element. The nature of alloying element also has a significant effect on the diffusion order of the platinum atoms. Further investigation is necessary in order to quantify the order of diffusion in terms of the alloying element.

8. Mackay Transformation

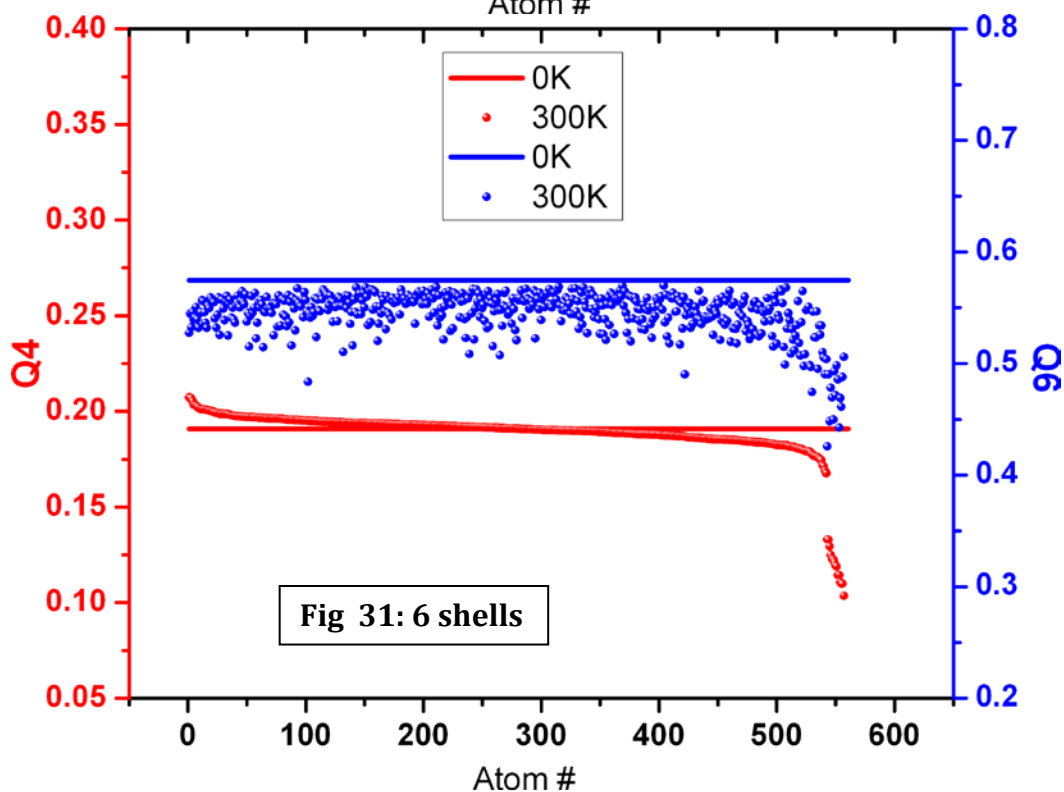
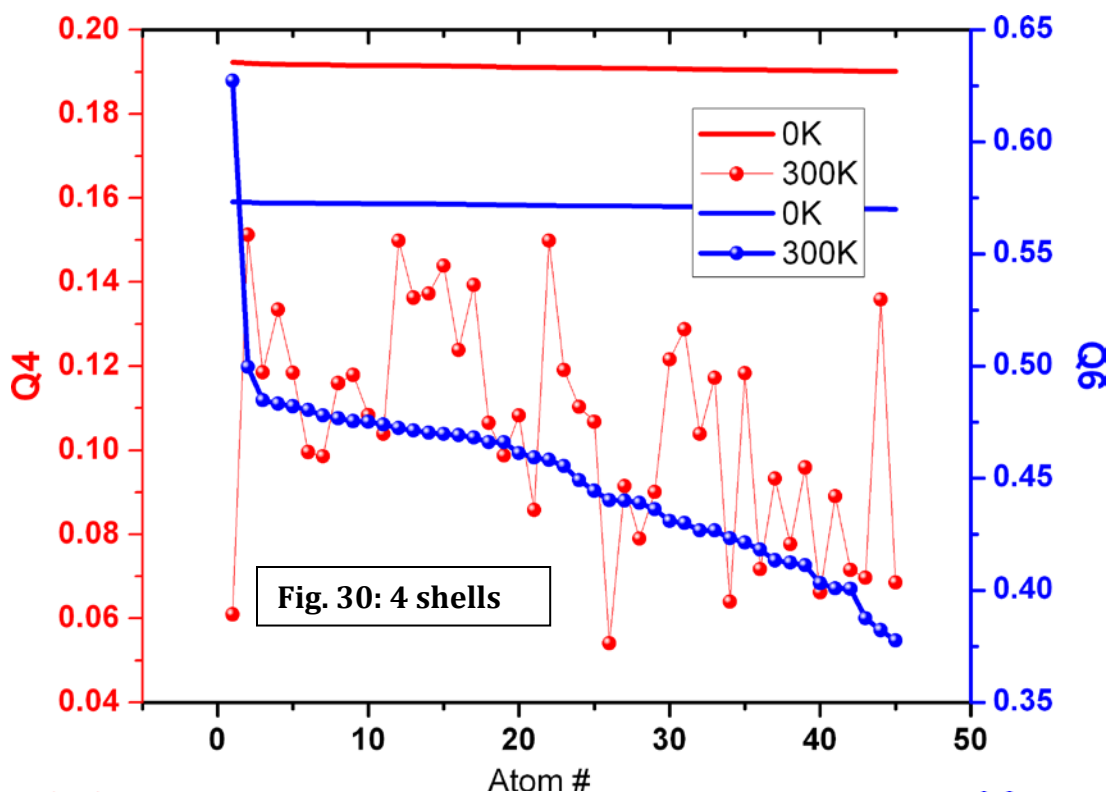
In spite of the large number of theoretical and experimental studies, the atomic structure of small clusters is still the object of many investigations. When the size of the cluster decreases, most atoms become surface atoms with low coordination and are subject to forces which lead to an equilibrium atomic configuration possibly different from that of a fragment of the bulk phase. Furthermore the relative stability of two clusters depends on several fundamental quantities: the number of surface atoms, the orientation of facets and their relative energies, the stress inside the cluster etc. The determination of the atomic configuration of small clusters is however of a fundamental importance in addressing chemical and physical properties, such as catalysis or crystal growth, of any system. Typically electron diffraction and Extended X-ray Absorption Fine Structure (EXAFS) are used to identify the nanoparticle structures. In these experiments, clusters with five fold symmetry axes have been observed, whereas such axes are forbidden in perfect crystals. For instance, icosahedral aggregates have been found in a large number of experiments on rare gas clusters [farges1981] and also on metals like Cu, Ag, Au, Ni, Pd, Pt and Co [lathioka1996]. Moreover, the cluster sizes $N = 55, 147, 309, 561$ atoms of Ni and Co have revealed to be particularly stable [lerme1994] and have a closed icosahedral structure (i.e., made of closed atom shells). From the theoretical point of view and since the rare gases and all the metals quoted above have an fcc solid phase (save for Co which has

however an fcc phase at high temperature), it is interesting to study the relative stability of the closed icosahedral clusters and fcc clusters which have the same sequence of number of atoms, i.e., closed cuboctahedral structures. Several studies of this type can be found in the literature. Pair potentials (Lennard-Jones or Morse) have been extensively used for rare gases [10{12]. For instance Doye and Wales [Doye1997] showed recently with a very simple Morse potential that a wide variety of scenario can be obtained depending only on the range of the potential. However, in metals and in particular for noble and transition metals, the interactions between atoms are not pair wise and energy calculations need either more elaborate potentials, containing at least a many body contribution, or ab initio methods. Recently many body potential functions such as the Sutton-Chen potential [sutton1], second moment potential [empiricalpot1994], glue model [carp1988], embedded atom model (EAM) [Daw1984], effective medium theory (EMT) [valke1992] have been used to study the structure of transition metal clusters. The results indicate a higher stability of the icosahedral structure at very small sizes.

Furthermore, Mackay [mackay1969],[mackay2] has quoted that it is possible to transform the cuboctahedron into an icosahedron by a simple continuous distortion. The cuboctahedron and the icosahedron are two very interesting polyhedra; the first one is an Archimedean solid whereas the second one belongs to the class of the five Platonic solids. Besides these historical classifications and their rather different apparent geometrical shapes, cuboctahedra and icosahedra are very closely linked, since a cuboctahedron formed of rigid rods can be transformed simply into an icosahedron. The cuboctahedral clusters are built on the basis of an fcc lattice, and from this transformation an icosahedral cluster with the same number of atoms is obtained. These two closed structures are particularly stable at intermediate sizes. Reports for existence of Mackay transformation of smaller cluster of metals such as Cu, Ni, Pd are available in the literature [mack3], [Bernholc1992]. No recent reports suggesting the existence of Mackay transformation for Platinum have been found. In this section we will focus on looking at cuboctahedral structure of platinum and observe if there is a

transformation observable for the platinum clusters. 3^{rd} shell clusters corresponding to 147 atoms of platinum are considered for this purpose. Cuboctahedral clusters are generated using a fcc lattice and the structures are set to equilibrate at constant temperature for $5ns$. The bond orders of the structure were compared both before and after the simulation. For a pure cuboctahedron the second order invariants exhibit a q_6 and q_4 values of 0.575 and 0.19 respectively. The central atom (atom #1) shows the icosahedral symmetry with values of ~ 0.05 and 0.62 for q_4 and q_6 respectively. Figure MD30 shows the comparison of the second order invariant measures between the initial structure, 0K, and the final structure, at 300K, obtained from the simulation. As observed the bond order parameters show a significant deviation from the starting fcc structure. A little closer look at the bond order parameter suggests that it is similar to the icosahedral cluster's bond order values. This suggests that the particle structure order shifts from a cuboctahedral starting structure to an icosahedral structure.

Larger shell number structures were studied as well. Figure MD31 shows the bond order parameter comparison for a $n = 6$ shells. The bond order function is found **to preserve** the cuboctahedral structure. This suggests that the icosahedral symmetry is the most favorable structure for smaller platinum nanoparticles. This is similar to that observed for fcc metals such as Ni, Cu and Pd [mack3], [Bernholc1992]. The overall value bond order parameter value for the larger cluster shows the values of $Q_4 = 0.2024$ and $Q_6 = 0.5823$. The values are closer to that exhibited by the starting cuboctahedral structure further showing the preservation of the cuboctahedral symmetry. This shows the existence of Mackay transformation for smaller platinum clusters which disappears for the larger clusters. Thus we can conclude that the cuboctahedron structure is also a stable structure for larger platinum clusters with an activation energy required for transformation between icosahedron and cuboctahedron structures.



Activation energy for the transformation was not observed from the energy profile with temperature. This suggests that the Mackay transformation observed in the case of platinum clusters is a second order variation in energy. One possible

explanation for not observing the energy transformation could be the type of thermostat used for the simulations. The Berendsen thermostat is not purely canonical in nature since the temperature scaling is done in terms of a velocity scaling method. This may lead to a leak in the energy of the system either to the bath or dissipated as a numerical error. Use of a more sophisticated canonical thermostat such as the *Nosé – Hoover* thermostat will give us a better control over the ensemble energetics. Smaller platinum particles find icosahedral structure to be predominantly favorable structure. Commercial fuel cell catalysts have particles of diameter $2\text{nm} - 5\text{nm}$. Simulations of larger particles are computationally intensive and hence have not been reported in this work. Icosahedral and cuboctahedral structures are both found to be stable structures for larger particles. However for smaller particle system the cuboctahedral structure is found to be unstable undergoing a transformation to icosahedral structure.

9. HRTEM Image Simulations

High Resolution Transmission Electron Microscopy (HRTEM) is an analytical technique commonly used to analyze/identify nanostructure of catalyst particles. Details of the internal structure of the particles can be gained by HRTEM from the direct visualization of the lattice planes from images. The morphology of very small particles (down to 1nm) as well as the lattice deformations near the interface, due to the lattice mismatch, can be accurately measured [smith1985], [Datya1992], [poppa1993]. Conventional image formation in the transmission electron microscope is achieved by magnifying either the forward-scattered beam, to form a bright field (BF) image, or one of the Bragg-scattered beams, to form a dark field (DF) image. High resolution electron microscopy in the imaging mode derives information about specimen by phase contrast methods. These methods are based on the theory of microscopic image formation in which an electron beam of coherent radiation falls on a periodic object, such as a crystal structure, and passes through an imaging lens, producing a diffraction pattern in the back focal plane of the objective lens. It actually represents a mapping of the Fourier transform of the specimen. Maximum information about the specimen, i.e., at highest resolution, can

be obtained by an inverse Fourier transform wherein all the Fourier coefficients are retained. This can be achieved by including higher-order reflections in the imaging aperture, which means that high-resolution detail is provided in the image by allowing the interaction of these higher-order reflections arising from planes of smaller spacing in the crystal and appearing at higher angles to the microscope optical axis. Phase contrast is derived from the variations in phase induced in the incident electron wave by both the specimen and the imaging system; because the TEM objective lens is imperfect and phase shifts are introduced from spherical aberration. The relative phase of interacting beams is an important factor in determining the resultant amplitude. By proper control of phase shifts the exit wave amplitude can be changed, yielding wide variations in contrast from the specimen. In order to get interpretable contrast, phase shifts must have a known relationship to the structure of the specimen. The thickness of the sample has a very significant effect on the nature of the image observed. In case of a non thin sample which leads to multiple scattering and attenuation, the phase shifting between the incident wave and image exhibit non linear relationship. In this case exit wave reconstruction is necessary to understand the intrinsic details of the image [keef1], [keef2].

Exit wave reconstruction to understand the details of structure of nanoparticle require a good approximate for starting structures to be used in HRTEM image simulations. Radmilovic et al. [radmilovic1994], [radmilovic2001] have used HRTEM image simulation to explore the changes in images of metallic nanoparticles under various imaging conditions, i.e., to relate the real particle size to its apparent size as derived from the HRTEM image. They demonstrate that even under optimum focusing conditions the spot intensity distribution does not correspond to the positions of the atoms in the particle due to the strong influence of Fresnel fringes near the edge of the particle. The results of this work suggest that measurements of size and relaxation of outer planes in small particles must be accompanied by image formation simulation knowing all imaging parameters and taking into account the strong Fresnel effect.

Image simulations for the structures of supported nanoparticles obtained from MD simulations were performed using EMS. The atom location information is

provided as a series of slice files corresponding to atom positions in each plane. Simulations were performed along two different directions for the supported particle. Figure MD32 shows the simulated HRTEM image obtained from simulations for a particle of 6 shells (corresponds to 923 atoms). As can be observed the images show fringes along the boundary of the particle due to the defocusing effect from the microscope parameters. The simulations were performed along $\langle 001 \rangle$ axis. The bright spots corresponding to the atom columns show significant deviations from an fcc lattice structure. These preliminary structures could be used for performing analyses such as strain field analysis and exit wave reconstruction. The model structure could be used to better understand HRTEM images obtained for supported catalysts. Further research in this direction is necessary in order to quantify the effect of support/substrate.

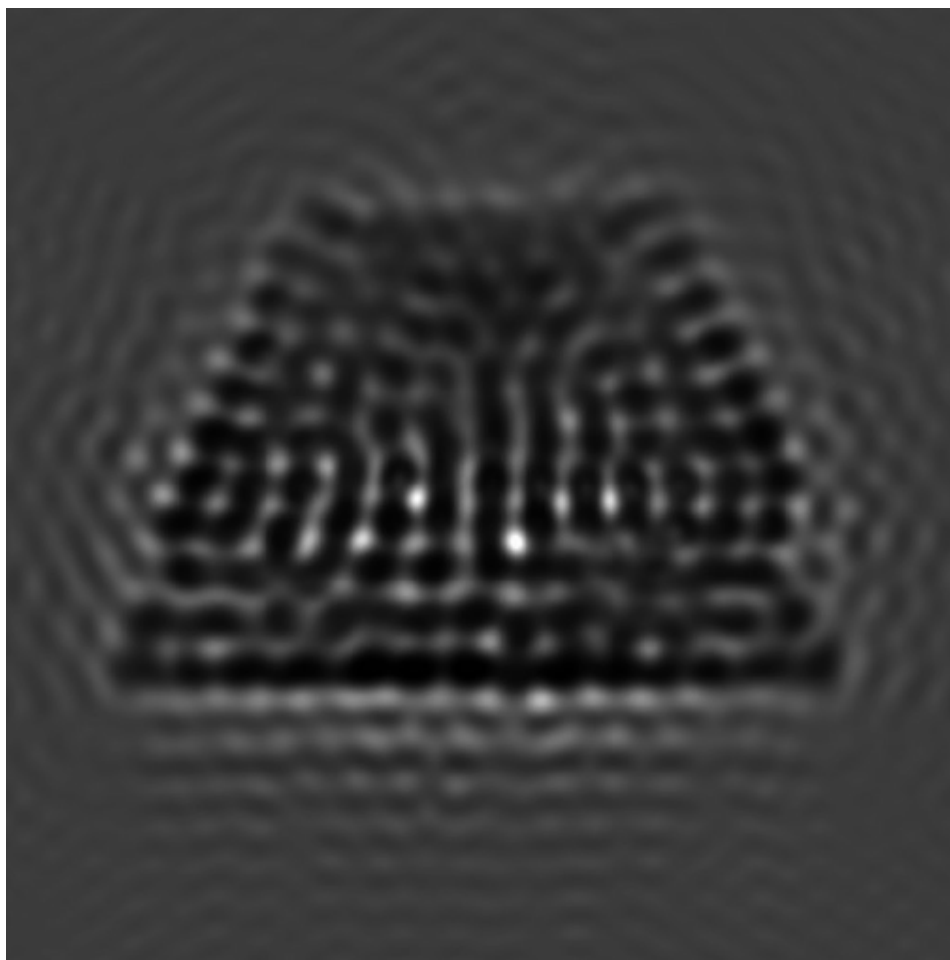


Fig. 32: Simulated HRTEM Image

HRTEM image simulations of simulated structures

Conclusions

Structure simulations for unsupported and supported nanoparticles have been described. The structure of the nanoparticle is affected significantly due to the presence of support and the interaction is confined to the interface between the metal and substrate. Larger particles exhibit lower strain in the bulk of the particle and the interaction effect of the support is restricted to the interface of the particles. Geometric utilization of nanoparticles was estimated using simple Comsol calculations. The geometric utilization decreases significantly with decreasing particle size. The effect of new supports on the structure of the nanoparticles has been described. Increased strain on the particles is observed to increase with increasing interaction energy between the support and nanoparticle. The strain is found to be localized to the bulk of the particle suggesting the catalytic activity of the nanoparticle is affected by changing the nature of the support. Alloy particle of core-shell structure were used for simulating structures of alloy nanocatalysts. The core-shell order is disturbed in the presence of support and the improved activity for nanoparticles could be explained in terms of the variation of the Pt-Pt bond distance on the surface of the catalyst particles. Phase segregation effects in the alloy nanoparticles are prevented by the presence of support interaction suggesting the behavior of support as a stabilizer of the particles. This method could be used as a tool for determining the structure of new materials for fuel cell catalysts. The generality of the simulations ensure the applicability of this method to study different catalytic materials. Effect of temperature on the structure of the particle suggests change in strain of the particle with temperature. Higher temperatures lead to higher strains suggesting the atom positions are displaced as a function of temperature. Activity variation of catalyst materials as a function of temperature could be explained by performing quantum mechanical simulations on these structures to identify the catalytic activity. Trapping of the particles by the support is described in terms of *Lévy* diffusion process. The diffusion order of the atoms in the case of unsupported and supported particles reveals the existence of a

secondary diffusion mechanism for the cluster to the support. HRTEM image simulations of the structures were performed for the simulated nanoparticles. Reaction mechanism studies of catalyst particles are done using EXAFS and XANES experiments. These methods require realistic starting structures for the catalyst particles. MD simulation results provide a good starting structure for the analyses from these experiments. These simulation methods help contribute significantly to the progress in understanding the structure of supported nanocatalysts and in the design of new materials for applications in PEMFCs.

Reference: A more detailed treatment of the topics of this section, Experimental Target 11: Simulations of support-particle interactions, is found in the 2008 Ph. D. dissertation by Ramachandran Sabbaraman submitted to Case Western Reserve University. The Manuscript can be downloaded from the OhioLINK EDT Center. The internet address is **http://edt.ohiolink.edu/view?acc_num=case1205852564**

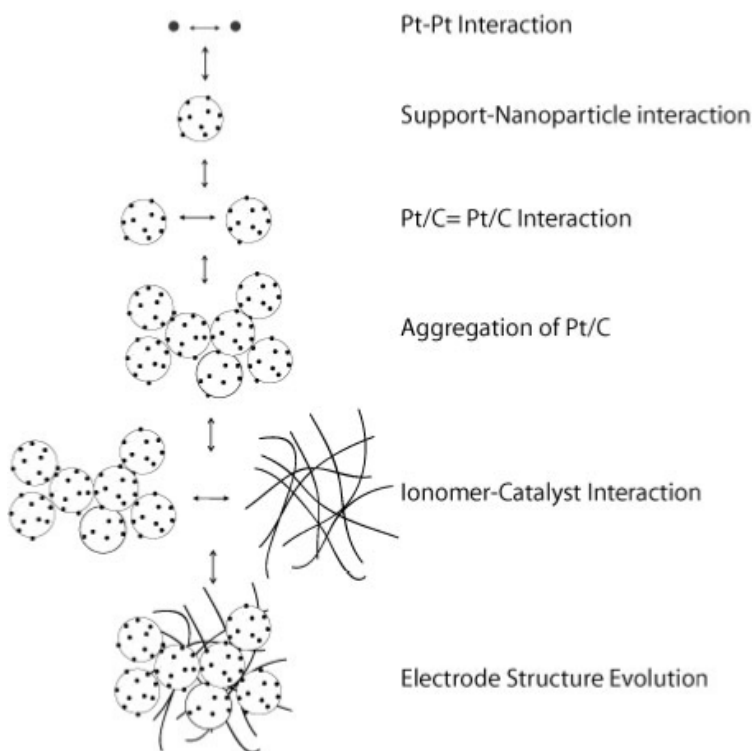
Experimental Target 12: Composite Electrodes

Synopsis:

A complete model detailing the formation of composite electrode structures was developed. This model was built from the colloidal interactions of components.

Detailed Report:

In order to take information from theory and fundamentals of reaction



pathways and understand applications in fuel cells, we are constructing a multiscale model of a thin film catalyst layer. This model, schematically illustrated at left, considers a nested series of structures formed by well-defined interactions. For example, Pt nanoparticles interact with carbon support to form the catalyst particles typically used. These interact with each other and with the

proton conducting binder.

As the first step in this hierarchical model of a composite fuel cell electrode, a simple model probing the catalyst utilization for supported catalysts used in fuel cells was developed. Some basic conclusions derived specifically from geometric constraints were developed. Active area losses are estimated for cases of (1) a single carbon particle loaded with Pt colloidal particles and (2) carbon-supported Pt (C/Pt) particles contained in matrices. The particle matrices are used to simulate the PEMFC electrodes. The effects of catalyst loading, particle size and support surface area are explored and results for the catalytic area loss are presented for

each of these cases. Values for loss corresponding to maximum loading achievable for random and ordered packing are presented. The values obtained for catalytic area losses from the geometric model suggest the existence of optimum structures for fuel cell electrodes.

Experimental Target 13 Electroanalysis

Synopsis:

New in situ electrochemical methods were deployed and validated. Pulsed voltammetry was shown to be directly applicable to fuel cells, allowing direct interrogation of electrode kinetics in the actual environment of the fuel cell.

Detailed Report:

Patrick Pietrasz and Thomas Zawodzinski

Recent concern over the sluggishness of the oxygen reduction reaction (ORR) on the fuel cell cathode has led to a renewed interest in the cathode catalytic process and the suitability of platinum and platinum alloy catalysts for use in hydrogen / air fuel cells. Owing to the fast reaction kinetics on the typical fuel cell anode (on an order of magnitude faster than the cathode kinetics), there is little concern for catalyst improvement at the anode. A better understanding of the cathode kinetics could lead to catalysts that make better use of available platinum, to address the platinum loading and current high cost of fuel cell catalysts. The use of high power density fuel cells for vehicular or mobile applications in particular shows promise for near term implementation in specialized applications.

The development of pulse voltammetry as an analysis technique has its beginnings in mercury drop and micro disk electrodes. Both are solid electrodes that include a surface refresh step in the electrochemical process. Pulse voltammetry controls the surface state of the electrode and the rate of surface refresh. In general, the technique is applicable to solid electrodes due to the surface refresh capabilities of pulse voltammetry. Mercury drop electrodes have a built-in surface refresh step in that the electrode surface is completely replaced as soon as the mercury drop detaches from the capillary electrode. The benefit of a constantly refreshed surface is a high sensitivity due to the clean surface before each experiment, and the ability to detect reaction intermediates. Extending the technique to fuel cells would allow for the detection and measurement of surface oxides and intermediates in situ in the fuel cell. Typically, experiments concerning the fuel cell catalyst layer and electrode

reactions are studied in aqueous media with a rotating disk electrode (RDE) setup. The question always remains whether the aqueous system is an accurate representation of the functional fuel cell electrode due to concentration gradients and the lack of a triple-phase boundary in the aqueous system. The use of pulse voltammetry eliminates speculation on the difference between experimental and actual electrode conditions.

Osteryoung [1] applied pulse voltammetry to microdisk electrodes for the detection of reactive intermediates. This serves as the basis for the application of pulse voltammetry to the fuel cell. Osteryoung introduced normal pulse and reverse pulse voltammetry and the description of said techniques. Pulse voltammetry is an array of sampled current techniques, the most common of which are normal pulse, reverse pulse, differential normal pulse, and square wave voltammetry. Normal and reverse pulse voltammetry are suited as general analysis techniques similar in scope to cyclic voltammetry, while differential normal pulse and square wave voltammetry are background subtractive techniques, which would be particularly useful for the detection of short lived surface species or low levels of adsorbates. Square wave voltammetry has favorable characteristics for multiple step surface reactions and the discrimination between surface reactions. Reverse pulse voltammetry is particularly useful for determining the stability of a reaction product over a potential range. As applied to microdisk electrodes, pulse voltammetry consisted of a gradually increasing set of potential steps. Normal pulse voltammetry was chosen due to the nonplanar surface renewal behavior at shorter time scales at the microdisk electrode surface than with a pumped or stirred system. A fuel cell electrode is considered to be a triple-phase boundary, in that reactant gases interact with the solid electrode surface. The electrode surface contacts or is considered to be covered with a wetted ionomer.

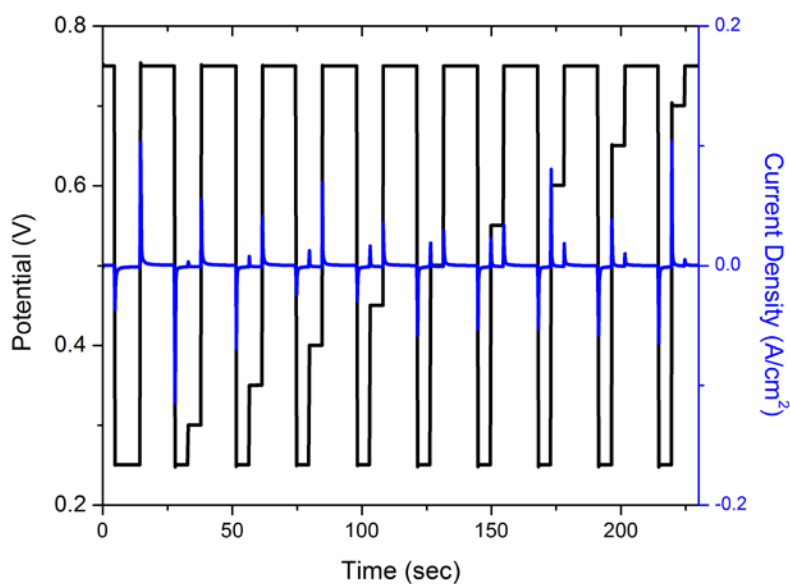


Fig. 1: Typical pulse voltammetry experiment in a fuel cell operated at 80°C, 50sccm H₂ / 50sccm N₂ (anode / cathode). 10 second pulse times.

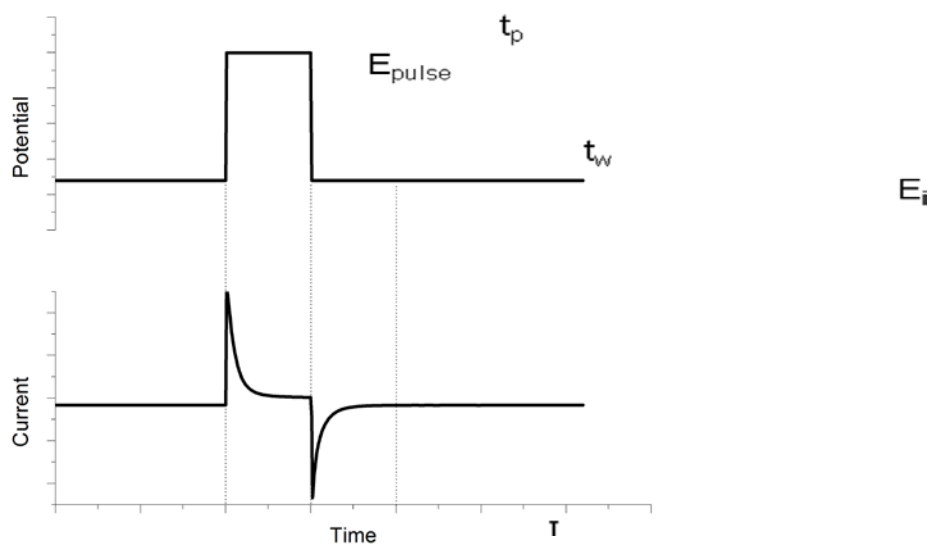


Fig. 2: Normal pulse waveform and response. The current is measured at τ .

Pulse steps and durations are chosen to electrochemically clean the electrode surface, preparing it for the subsequent step to some reaction potential. The

electrode is conditioned in normal pulse voltammetry to delay the initial faradaic reaction before the current is sampled. The technique was originally invented by Barker and Gardner as an adaptation of a polarographic technique [2]. The Cottrell equation defines the current decay characteristic for the system, and the difference between the measured current decay and theoretically calculated decay current can be attributed to the current of reaction. The electrode cleaning step occurs sufficiently quickly that the electrode remains clean for the short duration of the pulse experiment. In normal pulse voltammetry, a square wave voltage pulse of time duration t_p is applied to the cell. Subsequent voltage pulses are applied with an increasing potential from E_i to E_{pulse} in fixed potential steps. The current response of the cell is measured at the end of the wait time, t_w . Typical current response to a normal pulse experiment is shown in figure 1.

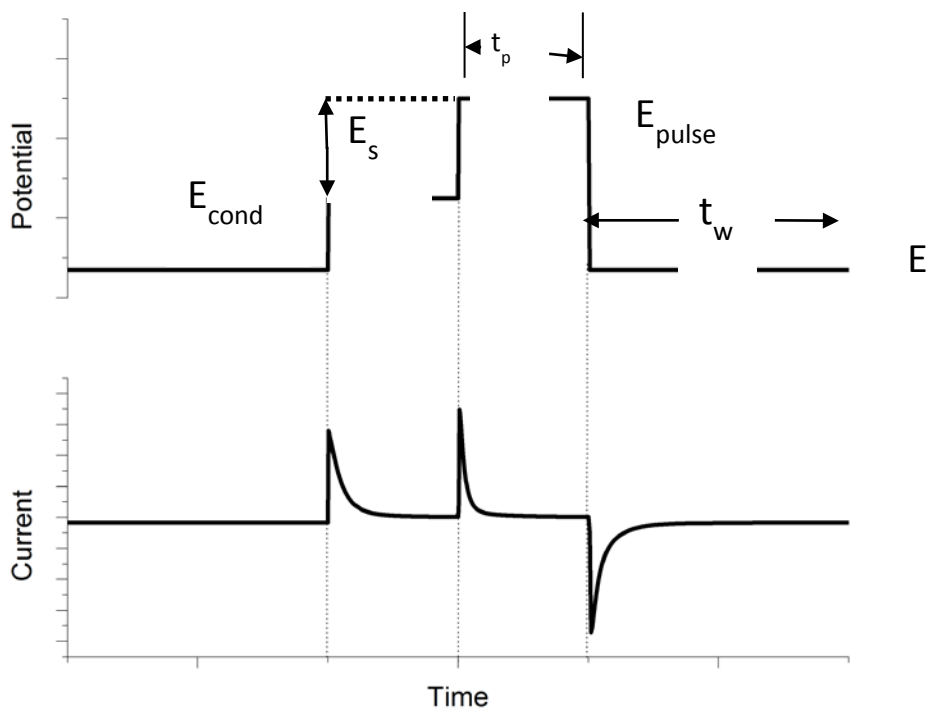


Fig. 3: Reverse pulse waveform and current response.

In reverse pulse voltammetry, the electrode starts at the limiting current for some reacting species before being stepped to a lower reaction or non-reaction condition. This enables the detection of intermediates and adsorbates on the surface of the electrode due to the fast reaction and measurement time. Deviation from the limiting current allows for discrimination of the reaction current and leads to the high sensitivity of this technique. Under carefully controlled conditions, pulse voltammetry mimics cyclic voltammetry, i.e. the shape of a pulse voltammogram can be recreated with pulse voltammetry, with higher sensitivity due to the surface refresh effect. Pulse voltammetry is also a qualitative technique. Spectroscopic techniques would have to be applied to the system to determine exactly what sort of chemical species are present at the electrode surface. The pulse pattern and current response is shown in figure 3.

Pulse Time

A key problem of the application of pulse voltammetry to a fuel cell system is the discrimination between the charging and faradaic current in the fuel cell. Both currents are present on different time scales in the cell. Charging current is a result of the control of the time parameter allows one to discriminate between the charging and faradaic current. Charging current dominates over short time scales (under 0.1 seconds), since initially the cell behaves as a capacitor due to the high surface area of the fuel cell electrode. The basic initial experiments appeared similar to chronocoulometry. Varying the current sampling time results in the measure of a different current.

Figure 4 below shows a current density (i) versus $1/t^{1/2}$ plot obtained from the chronoamperometric curve from the reverse pulse experiment. The non-linearity of the curve relates to the two previously mentioned measurement of a charging and faradaic current.

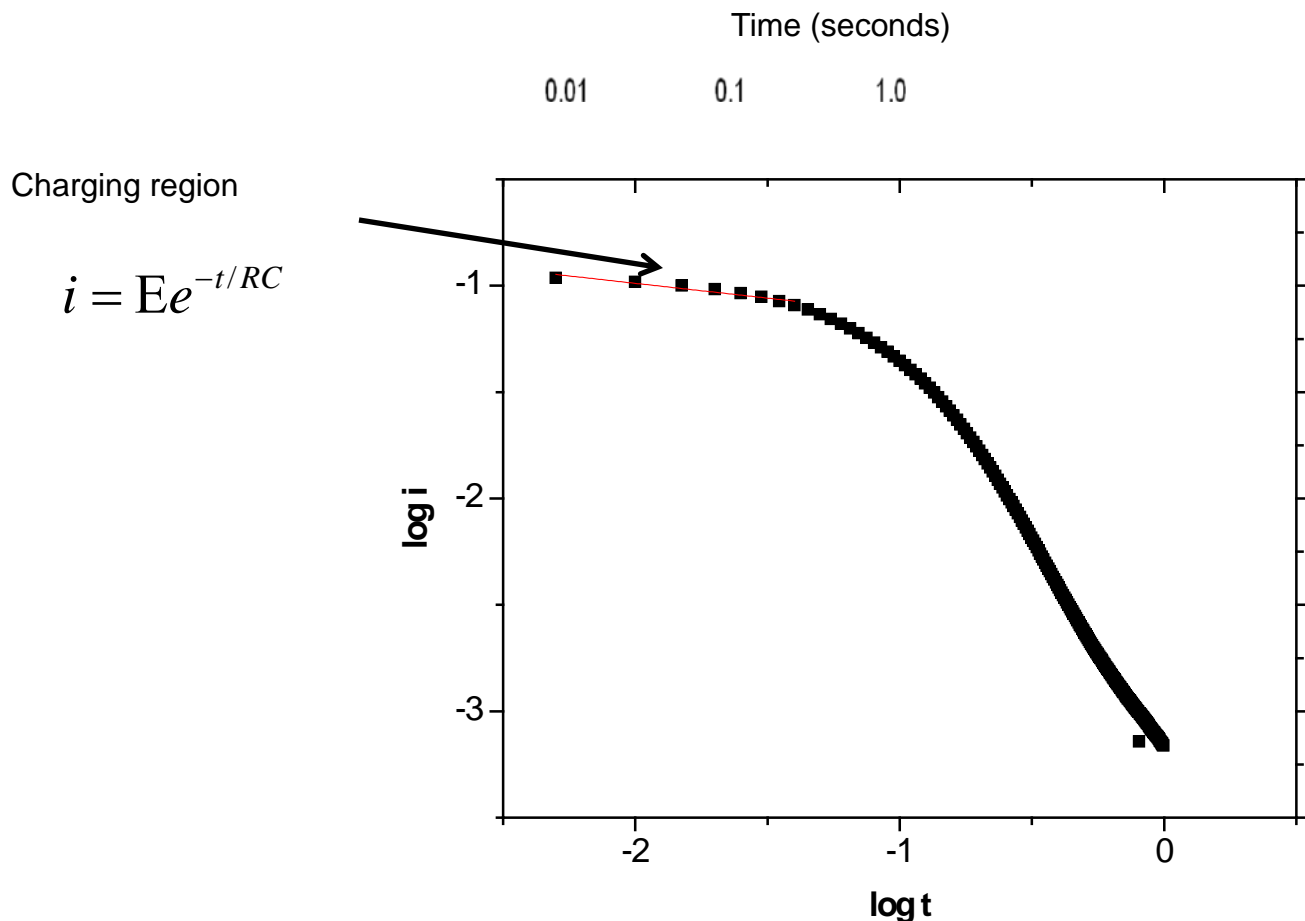


Fig. 4: Fuel cell current short time scale response from a single applied pulse.

Measurement of the current occurs at some time, τ , where $0 < t < \tau$. The potential step occurs at time t . A further step down to the base potential also contains useful information. The wait time must be sufficiently long to allow for the reaction current belonging to the previous step to decay before the next pulse is applied to the cell. Techniques similar to differential normal pulse or square wave voltammetry can potentially discriminate against this background current and allow for shorter time between pulses.

The Normal Pulse Voltammogram

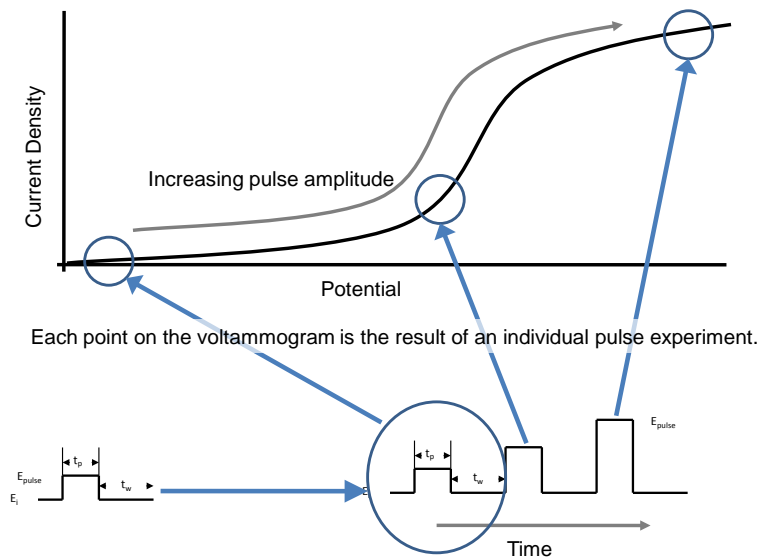


Fig. 5: Normal pulse voltammogram waveform. The voltammogram is composed of a discrete sequence of potential steps of gradually increasing amplitude.

For the most common system in the normal pulse mode, the electrode starts at some base potential near the open circuit potential for a hydrogen anode and nitrogen cathode. The cell potential under these conditions is typically 50-80mV versus the standard hydrogen electrode (SHE, the conditions of which are present at the anode). Experimental cells were typically run with the reference electrode shorted to the anode, due to the fast reaction kinetics at the anode and the inherent SHE. A sequence of increasing potential steps is then applied to the cell in the normal pulse mode. The instantaneous potential pulse forces reaction at the electrode surface and the decay current after the pulse is applied is measured on some time interval.

ORR: For the investigation of the oxygen reduction reaction

Platinum hydroxide and platinum oxide form on platinum in the presence of water and/or oxygen and under high potentials versus RHE in a fuel cell environment. Both oxides inhibit the diffusion of gas to the surface of the catalyst, and limit the

number of reaction surface sites available, and thus the subsequent rate of reaction. The problem is especially pronounced on the cathode in a hydrogen / air fuel cell due to the sluggishness of the oxygen reduction reaction (ORR) kinetics. The fuel cell particularly experiences high potentials which favor platinum oxide formation during startup and shutdown. Experimental evidence in the literature suggests a initial formation of PtOH at potentials over 0.84 V vs. RHE [3], as well as the following reactions of platinum to form different oxides in the following sequence [4-6]:

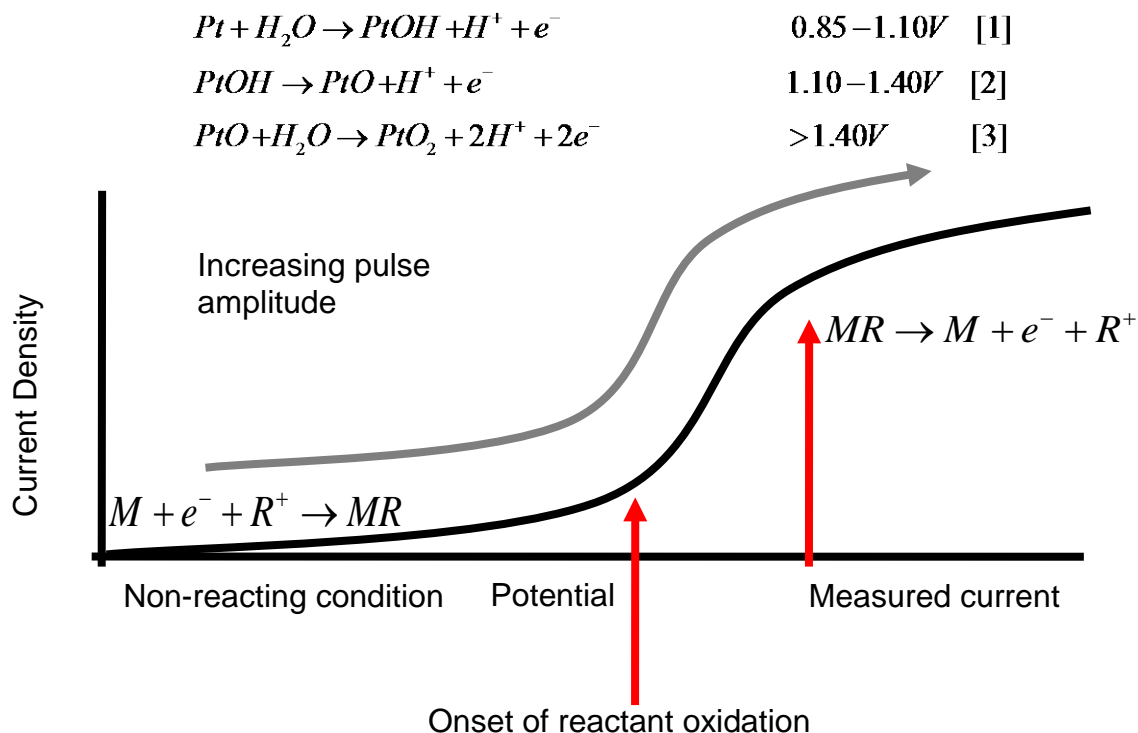


Fig. 6: Steps and reactions of pulse voltammetry on waveform

A better understanding of when the platinum oxide begins to form, and what conditions favor oxide formation or removal in a fuel cell environment would be beneficial in determining optimal conditions for fuel cell operation. Additionally, the development of a technique for in situ measurement of the onset potential for platinum oxide formation provides a means of characterizing catalyst performance in the fuel cell. The effect of varying catalyst compositions and morphologies can

also be studied. The transition potential from PtOH to PtO₂ is also an interesting regime that can be studied by pulse voltammetry to better understand when and at what potential the transition occurs, as well as the kinetics of platinum oxide removal. Growth rate of platinum oxides is dependent on the catalyst composition, thus different catalysts will change the onset potential for PtOH formation from that of pure Pt. The different regions of voltage limited platinum oxide growth overlap with the oxidation of carbon.

Experimental

Fuel cell membrane electrode assemblies (MEA) were prepared in house. The catalyst layer was composed of ETEK 20 wt% Pt/C at a loading of 0.4mg/cm² at both the anode and cathode. Prepared catalyst inks were hot pressed onto Nafion® 117 ionomer. All fuel cell experiments were carried out at 70% and 100% relative humidity and 60°C or 80°C on a Precision Flow Technologies test stand. A Solartron SI 1280B and an Eco Chemie Autolab PGSTAT 302 potentiostat was used for all measurements and programmed pulse potentials.

Cells were conditioned for 24-48 hours before testing. Most testing was carried out in hydrogen anode and nitrogen cathode conditions to limit the amount of oxygen present in the system. Testing under the normal fuel cell operating mode of hydrogen and oxygen results in high instantaneous pulse currents beyond the limits of the test equipment.

Results & Discussion

Initial experiments were conducted to determine the optimal pulse time, width, and delay between subsequent pulses. The fuel cell electrode has a large electrochemical surface area. The capacitive elements of the resulting post-pulse current can be taken into account with the Cottrell equation, resulting in a measurable reaction current. A time of 1-5 seconds for the pulse width was found to be optimal for most

experiments, as longer times were found to decay to the background current level. At open circuit potential (approximately 70-100mV, depending on the membrane) with a hydrogen anode / nitrogen cathode, there is a residual current present in the system; the hydrogen crossover current. At potentials higher than the open circuit potential, a hydrogen pumping mechanism is present in the cell. Pulse times shorter than 5 seconds resulted in erratic cell behavior and current reversal in the cell if the cells were not sufficiently conditioned beforehand. Maximum peak currents observed exceeded 2.5 amps, and the step potential was limited by the potentiostat at approximately 800mV, as potential steps greater than this limit exceeded the current rating of the instrument, even when operating the cell with hydrogen and nitrogen. Hydrogen / air operation was not possible under the current experimental setup without exceeding existing cell current limits.

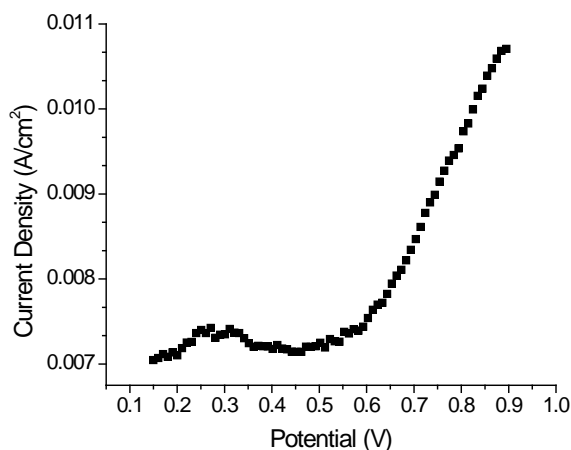


Fig. 7: Good NPV result. $E_i = 500\text{mV}$, 10mV/step , 80°C , $100\%\text{RH}$

A reverse pulse experiment is shown in figure 3 in comparison to the steady state current values obtained by holding the electrode at. Steady-state current values were obtained by maintaining the electrode at a single potential for long periods of time in relation to the pulse experiment (5 minute potential holds). There is an observed oxidation current; however the cell does not reach a limiting current.

An initial oxidation onset potential of approximately 550mV for the formation of PtOH was measured in the reverse pulse experiment which is substantially lower than the experimentally determined value of 0.85 volts present in the literature [7]. The measurement of such a low oxidation potential for platinum was due to the fast measurement and reaction times directly at the fuel cell electrode, and the use of a reverse pulse technique to clean the electrode before each experiment. Platinum oxide formation is the most likely reaction occurring at the investigated potentials, and under the conditions present in the fuel cell. However, pulse voltammetry can measure reaction currents, but provides no information about the reacting chemical species.

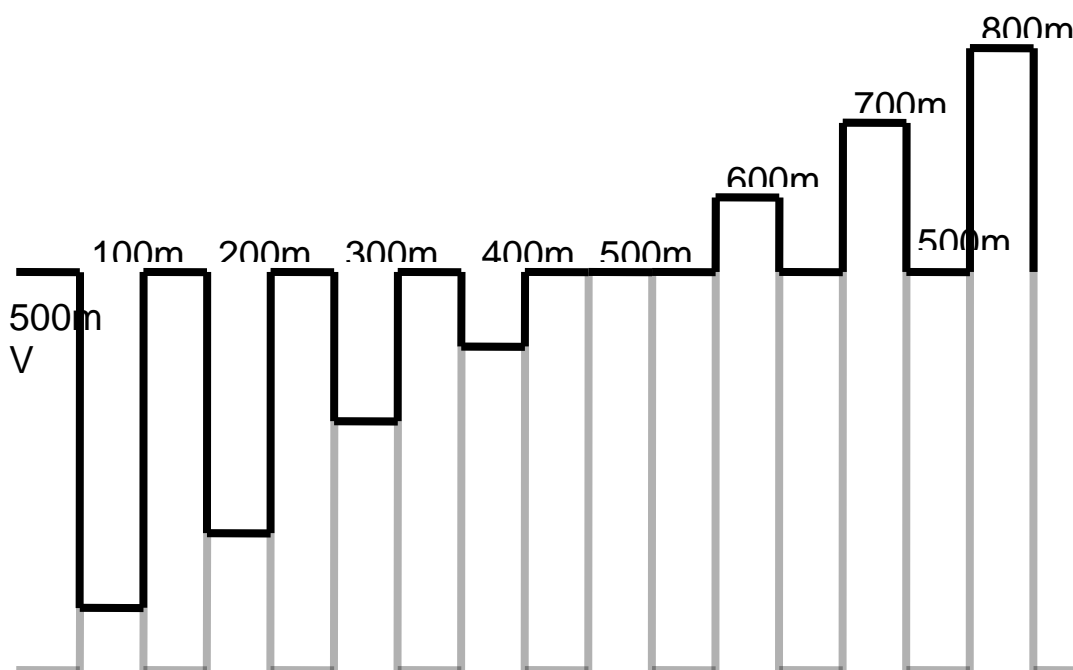


Fig. 8: Example pulse sequence and initial pulse sequence for the voltammograms in figure X. The gray sequence begins from an initial potential of 250mV. The black sequence begins from 500mV and increases in 100mV increments.

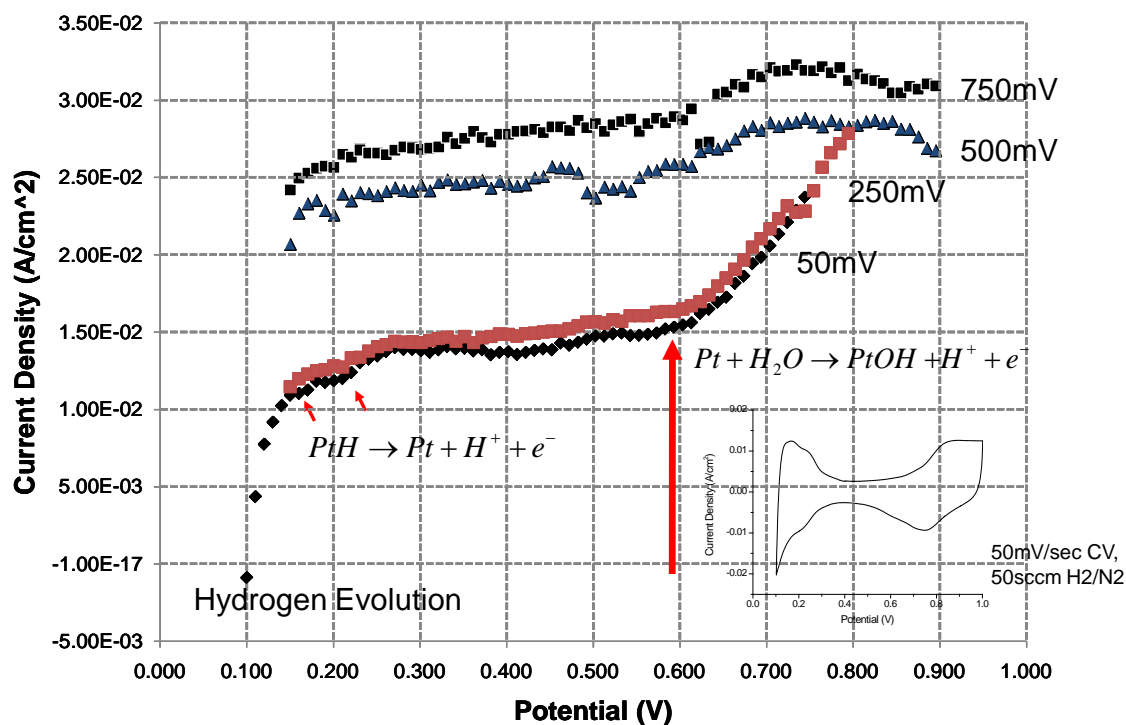


Fig. 9: Sequence of applied potential steps from different initial potentials and current response. A typical CV of the cathode under the same conditions is present in the bottom right corner.

Figure 9 above details a sequence of pulse voltammograms obtained from a fuel cell from varying initial potentials of 50, 250, 500, and 750mV. Though initially the shape of the voltammograms appears consistent with initial and expected results, the interpretation of the voltammogram leads to slightly different information. The purpose of the particular experiment was to determine the effect of the initial potential on the shape of the voltammogram, which relates to the expected reactions occurring on the surface of the platinum in the fuel cell. At 50mV, no initial reaction is expected (other than hydrogen crossover) since the surface of the platinum is initially covered with adsorbed hydrogen species (PtH) under this low potential condition. During the course of a single normal pulse, the cathode starts at

open circuit hydrogen / nitrogen potential (70mV). At the start of the experiment, the electrode potential is lowered to 50mV (this potential is chosen), where no reaction is expected – this is the baseline or initial potential for the experiment. A potential pulse is then applied to the cell by the potentiostat. This higher potential immediately facilitates a reaction to occur at the electrode surface, if the potential step is to a reaction potential, and leads to a high measured initial current.

The voltammograms at 50 and 250mV have similar shape to the idealized voltammogram presented earlier. The progression from the hydrogen evolution region to the pseudo steady-state hydrogen crossover dominated region is clear, as is the step to the PtOH stripping region above 600mV. Once the initial potential is raised to 500 and 750mV, the initial measured current shows an approximately 2.5 times enhancement over the 50 and 250mV cases. The only parameter that changes between each voltammogram is the initial potential from which the pulse sequence starts. This enhancement in the measured current is most likely due to a surface roughening effect due to the rapid cycling at the cathode surface, and the amplitude of the potential steps past 250mV. A set of experiments with smaller, more discrete potential steps is planned.

New analysis methods were also developed by Wieckowski during analysis of methanol pathway. These were detailed above, in a previous section..

4. Comparison of Proposed Elements and Accomplishments of the Program

Succinctly stated, our theory and experimental goals were as follows:

Theory Objectives

- Accurate Quantum Mechanical Methods for Kinetics and thermodynamics
- ‘In silico’ Synthesis of Particle Structure
- Quantum Mechanical Electrocatalysis
- Ab initio Descriptions of Electron/Proton Transfer
- Predictive Catalysis: Multiscale Catalysis Model
- Data Mining Approaches to Predict New Materials

Experimental Objectives

- Theory Support
- Studies of Key Electrocatalytic Processes
- New Catalysts
- New Experimental Characterization of Structure

All of these objectives were achieved in the course of this project. We have reported a long series of innovations and, indeed, have extended this original list. Several of the investigators in the team have been cited as among the most productive ARO contractees.

5. Impact

The impact of the program can be assessed in several ways. The output of the program in terms of publications, patents, books and so on is described, as is the output in terms of number of people. Also important are programs that have grown out of the MURI activities and collaborations. These are summarized below.

Peer-Reviewed Publications (*published*)

1. D. Cao, G.-Q. Lu and A. Wieckowski; S. A. Wasileski and M. Neurock, *J. Phys. Chem. B.*, **109**, 11622-11633 (2005). "Mechanisms of Methanol Decomposition on Platinum: A Combined Experimental and Ab Initio Approach". Press release: (<http://pubs.acs.org/subscribe/journals/cen/83/i26/html/8326sci2.html>)
2. J. S. Spendelow and A. Wieckowski, *Phys. Chem. Chem. Phys.*, **6**, 5094-5118 (2004). "Noble Metal Decoration of Single Crystal Platinum Surfaces to Create Well-Defined Bimetallic Electrocatalysts".
3. J. Spendelow, G. Q. Lu, P. J. A. Kenis and A. Wieckowski, *J. Electroanal. Chem.*, **568**, 215-224 (2004). "Electrooxidation of Adsorbed CO on Pt(111)/Ru in Alkaline Media: Comparison with Results from Acidic Media".
4. F. Maillard, G. -Q. Lu, A. Wieckowski and U. Stimming, *J. Phys. Chem. B feature article*, **109**, 16230-16243 (2005). "Ru-Decorated Pt Surfaces as Model Fuel Cell Electrocatalysts for CO Electrooxidation".
5. D. Cao and A. Wieckowski, J. Inukai and N. Alonso-Vante, *J. Electrochem. Soc.*, **153**, A869-A874 (2006). "Oxygen Reduction Reaction on Ruthenium and Rhodium Nanoparticles Modified with Selenium and Sulfur".
6. J. S. Spendelow, J. D. Goodpaster, P. J. A. Kenis and A. Wieckowski, *J. Phys. Chem. B*, **110**, 9545-9555, 2006. "The Mechanism of CO Oxidation on Pt(111) in Alkaline Media".
7. J. S. Spendelow, P.K. Babu, A. Wieckowski, *Curr. Opinion Solid St. and Mat. Science*, **9**, 37-48 (2006). "Electrocatalytic Oxidation of Carbon Monoxide and Methanol on Platinum Surfaces Decorated with Ruthenium".
8. H. Schweiger, E. Vayner, and A. B. Anderson, Why is there such a Small Overpotential for O₂ Electroreduction by Copper Laccase?, *Electrochem. Sol. St. Lett.*, **8**, A585-A587 (2005).
9. R. A. Sidik, A. B. Anderson, N. P. Subramanian, S. P. Kumaraguru, and B. N. Popov, O₂ Reduction on Graphite and Nitrogen-Doped Graphite: Experiment and Theory, *J. Phys. Chem. B*, **110**, 1787-1793 (2006).

10. R. A. Sidik and A. B. Anderson, Co_9S_8 as a Catalyst for Electroreduction of O_2 : Quantum Chemistry Predictions, *J. Phys. Chem. B*, 110, 936-941 (2006).
11. Taylor, C. D., and M. Neurock, "Theoretical Insights into the Structure and Reactivity of the Aqueous/Metal Interface", *Current Opinion in Solid State Mater. Sci.*, 9, 45-65, 2005.
12. Taylor, C.D., S. A. Wasileski, J. Fanjoy, J.S. Filhol, M. Neurock, First Principles Reaction Modeling of the Electrochemical Interface: Consideration and Calculation of a Tunable Surface Potential from Atomic and Electronic Structure", *Phys. Rev. B*, 73, 165402, 2006.
13. Filhol, J. S., and M. Neurock, "First-Principles Elucidation of the Electrochemical Activation of Water over Pd", *Angew. Chemie International (Frontispiece)*, 45, 3, 402 – 406 and *Angewandte Chemie German Ed.*, 118, 3, 416 - 420.
14. Neurock, M., S. Wasileski, and D. Mei, "From First Principles to Catalytic Performance: Tracking Molecular Transformations", *Chem. Eng. Sci.*, 59, 22-23, 4703-4714, 2004.
15. V. S. Murthi, S. Mukerjee and D. Ramaker, Correlation of Water Activation, Surface Properties and Oxygen Reduction Reactivity of Supported Pt-M/C Bimetallic Electrocatalysts using X-ray Absorption Spectroscopy', M. Teliska, *J. Electrochem. Soc.*, **152(11)**, A2159, (2005).
16. V. S. Murthi, S. Mukerjee and D. Ramaker, Correlation of Water Activation, Surface Properties and Oxygen Reduction Reactivity of Supported Pt-M/C Bimetallic Electrocatalysts using X-ray Absorption Spectroscopy', M. Teliska, *J. Electrochem. Soc.*, **152(11)**, A2159, (2005)
17. Neurock, M., S. Wasileski, and D. Mei, "From First Principles to Catalytic Performance: Tracking Molecular Transformations", *Chem. Eng. Sci.*, 59, 22-23, 4703-4714, 2004.
18. Filhol, J. S., and M. Neurock, "First-Principles Elucidation of the Electrochemical Activation of Water over Pd", *Angew. Chemie International (Frontispiece)*, 45, 3, 402 – 406 and *Angewandte Chemie German Ed.*, 118, 3, 416 -420.
19. Taylor, C.D., S. A. Wasileski, J. Fanjoy, J.S. Filhol, M. Neurock, First Principles Reaction Modeling of the Electrochemical Interface: Consideration and Calculation of a Tunable Surface Potential from Atomic and Electronic Structure", *Phys. Rev. B*, 73, 165402, 2006.
20. D. Cao, G.-Q. Lu and A. Wieckowski; S. A. Wasileski and M. Neurock, *J. Phys. Chem. B.*, **109**, 11622-11633 (2005). "Mechanisms of Methanol Decomposition on Platinum: A Combined Experimental and Ab Initio Approach". Press release:

(<http://pubs.acs.org/subscribe/journals/cen/83/i26/html/8326sci2.html>)

21. J. S. Spendelow and A. Wieckowski, *Phys. Chem. Chem. Phys.*, **6**, 5094-5118 (2004). "Noble Metal Decoration of Single Crystal Platinum Surfaces to Create Well-Defined Bimetallic Electrocatalysts".
22. J. Spendelow, G. Q. Lu, P. J. A. Kenis and A. Wieckowski, *J. Electroanal. Chem.*, **568**, 215-224 (2004). "Electrooxidation of Adsorbed CO on Pt(111)/Ru in Alkaline Media: Comparison with Results from Acidic Media".
23. F. Maillard, G. -Q. Lu, A. Wieckowski and U. Stimming, *J. Phys. Chem. B feature article*, **109**, 16230-16243 (2005). "Ru-Decorated Pt Surfaces as Model Fuel Cell Electrocatalysts for CO Electrooxidation".
24. D. Cao and A. Wieckowski, J. Inukai and N. Alonso-Vante, *J. Electrochem. Soc.*, **153**, A869-A874 (2006). "Oxygen Reduction Reaction on Ruthenium and Rhodium Nanoparticles Modified with Selenium and Sulfur".
25. J. S. Spendelow, J. D. Goodpaster, P. J. A. Kenis and A. Wieckowski, *J. Phys. Chem. B*, **110**, 9545-9555, 2006. "The Mechanism of CO Oxidation on Pt(111) in Alkaline Media".
26. J. S. Spendelow, P.K. Babu, A. Wieckowski, *Curr. Opinion Solid St. and Mat. Science*, **9**, 37-48 (2006). "Electrocatalytic Oxidation of Carbon Monoxide and Methanol on Platinum Surfaces Decorated with Ruthenium".
27. H. Schweiger, E. Vayner, and A. B. Anderson, Why is there such a Small Overpotential for O₂ Electroreduction by Copper Laccase?, *Electrochem. Sol. St. Lett.*, **8**, A585-A587 (2005).
28. R. A. Sidik, A. B. Anderson, N. P. Subramanian, S. P. Kumaraguru, and B. N. Popov, O₂ Reduction on Graphite and Nitrogen-Doped Graphite: Experiment and Theory, *J. Phys. Chem. B*, **110**, 1787-1793 (2006).
29. R. A. Sidik and A. B. Anderson, Co₉S₈ as a Catalyst for Electroreduction of O₂: Quantum Chemistry Predictions, *J. Phys. Chem. B*, **110**, 936-941 (2006).
30. Taylor, C. D., and M. Neurock, "Theoretical Insights into the Structure and Reactivity of the Aqueous/Metal Interface", *Current Opinion in Solid State Mater. Sci.*, **9**, 45-65, 2005.
31. Taylor, C.D., S. A. Wasileski, J. Fanjoy, J.S. Filhol, M. Neurock, First Principles Reaction Modeling of the Electrochemical Interface: Consideration and Calculation of a Tunable Surface Potential from Atomic and Electronic Structure", *Phys. Rev. B*, **73**, 165402, 2006.

Book Chapters

Wasileski, S.A., C.D. Taylor, and M. Neurock, "Modeling Electrocatalytic Reaction Systems from First Principles", in Device and Materials Modeling for the PEM fuel Cell, Ed. S. Paddison, Springer, 2005.

Books

Molecular Heterogeneous Catalysis: A Mechanistic and Computational Approach,
Authors: Rutger A. van Santen and Matthew Neurock, VCH-Wiley, Inc. 2006.

6. Summary

The MURI set out with a series of objectives to construct a ‘theory toolkit’ coupled to advanced experimentation for validation and support. We have achieved all of our initial objectives in this regard and have expanded the scope of the MURI to use theory and experimentation to drive the prediction and preparation of new and highly active catalysts for key processes in fuel cells.

Succinctly stated, our theory and experimental goals were as follows:

Theory Objectives

- Accurate Quantum Mechanical Methods for Kinetics and thermodynamics
- ‘In silico’ Synthesis of Particle Structure
- Quantum Mechanical Electrocatalysis
- Ab initio Descriptions of Electron/Proton Transfer
- Predictive Catalysis: Multiscale Catalysis Model
- Data Mining Approaches to Predict New Materials

Experimental Objectives

- Theory Support
- Studies of Key Electrocatalytic Processes
- New Catalysts
- New Experimental Characterization of Structure

All of these objectives were achieved in the course of this project. We have reported a long series of innovations and, indeed, have extended this original list. Several of the investigators in the team have been cited as among the most productive ARO contractees.

7. References

8. Appendices

1. Graduate Students and Post-Docs of the Project

Student	Institution	Advisor	Degree/Position
1. R. Subbaraman	Case	Zawodzinski/Mann	Ph.D.
2. M. Pelsozy	Case	Zawodzinski	Ph.D.
3. P. Pietrasz	Case	Zawodzinski/Sankaran	Ph.D.
4. J. Ziegelbauer	N.Eastern	Mukerjee	Ph.D.
5. Q. He	N.Eastern	Mukerjee	Ph.D.
6. Byungchan Han	MIT	Ceder	Ph.D.
7. Jacob Spendelow	UIUC	Wieckowski	Ph.D.
8. Rachel Behrens	UIUC	Wieckowski	Ph.D.
9. Ismaila Dabo	MIT	Marzari	Ph.D.
10. Tianhou Zhang	Case	Anderson	Ph. D.
11. Feng Tian	Case	Anderson	Ph. D.
12. M. Janick	UVa	Neurock	Post Doc
13. Kui Du	Case	Ernst	Post Doc
14. Ishihito Narita	Case	Ernst	Post Doc
15. Mina Hoorvar	Case	Mann	Post Doc
16. Rey Sidik	Case	Zawodzinski	Post Doc
17. Jamal Uddin	Rice	Scuseria	Post Doc
18. Wei Ping Zhou	UIUC	Wieckowski	Post Doc.